2011

Polymer based microfabrication and its applications in optical MEMS and bioMEMS

Guocheng Shao
Louisiana State University and Agricultural and Mechanical College

POLYMER BASED MICROFABRICATION AND ITS APPLICATIONS IN OPTICAL MEMS AND BIOMEMS

A Dissertation

Submitted to the Graduate Faculty of the
Louisiana State University and
Agricultural and Mechanical College
in partial fulfillment of the
requirements for the degree of
Doctor of Philosophy

In

The Interdepartmental Program in Engineering Science

By
Guocheng Shao
B.S., Zhejiang University, 2004
M.S., Shanghai Jiao Tong University, 2006
May, 2011

ACKNOWLEDGEMENTS

The author would like to take this opportunity to sincerely thank his major advisor, Dr. Wanjun Wang, for his continuous guidance, encouragement and support during the course of the author's Ph.D. study. Without Dr. Wang's devoted time and effort, the author's research work and this dissertation would not completed progressively.

The author is also obliged to his committee members: Dr. Tryfon T. Charalampopoulos, Dr. Steven A. Soper, Dr. Jin-Woo Choi and the Dean's Representative, Dr. Robert I. Hynes, for their professional advices and guidance on my research.

During his Ph.D. study, the author had the honor to work in Dr. Yuehe Lin's research group at Pacific Northwest National Laboratory (PNNL). During his stay in PNNL, the author received in-depth and generous guidance from Dr. Yuehe Lin, Dr. Jun Wang and Dr. Laxmikant Saraf.

Also, special thanks go to the author's fellow students in the research group, and colleagues in Dr. Lin's research group. It is you guys that made the author's Ph.D. study an experience with all kinds of fun.

Finally, the author's grateful appreciation goes to his parents whose hardworking spirit and dedication to family have always been a great example for the author.

TABLE OF CONTENTS

LIST OF FIGURES

ABSTRACT

Due to its ease of fabrication, low cost and great variety of functionalities, polymer has become an important material in microfabrication. MEMS devices with polymer as the structure material have found applications in various fields, especially in BioMEMS and optical MEMS.

In this dissertation, three polymer based microfabricated devices/components have been developed and tested. Various polymer based fabrication techniques, such as high aspect ratio SU-8 photolithography, three dimensional polydimethylsiloxane (PDMS) soft lithography, multi-layer soft lithography and PDMS double casting technique have been developed/studied and employed in the device fabrication process.

The main contribution of this dissertation includes: (1) Developed two novel methods for the fabrication of out-of-plane microlens. The PDMS and UV curable polymer (NOA73) replication technique made possible the fast replication of out-of-plane microlens and broaden the lens material selection. The in-situ pneumatical microlens fabrication technique, on the other hand, provides feasible method to integrate out-of-plane microlens into microfluidic chips requiring minimal design footprint and fabrication complexity. (2) Design, fabrication and test of a microchip flow cytometer with 3-D hydrofocusing chamber and integrated out-of-plane microlens as on-chip optical detection component. The developed micro flow cytometer offers 3-D hydrofocusing like conventional cytometer cuvette, and has on-chip microlens for optical signal collection to improve the detection efficiency. With the latest design improvement, the hydrofocusing chamber can focus the sample stream down to less than 10 μm in diameter in both vertical and horizontal directions. (3) Development of a PDMS microchip based platform for multiplex immunoassay applications. Integrated micro valves were employed for manipulation of fluidic reagents in the microchannel network. PDMS surface was used as the solid phase

substrate for immuno-reactions. Preliminary results showed that, even with low cost polyclonal goat anti-mouse IgG as the reporter antibody, the detection limit of goat mouse IgG can reach as low as 5 ng/mL (about 33 pM).

With the continuous advance in microfabrcation technique and polymer science, polymer based microfabrication and polymer MEMS devices will keep to evolve. In the future, more work needs to be done in this field with great potential and endless innovations.

CHAPTER 1. INTRODUCTION

1.1 Introduction of MEMS Technology

Micro Electro Mechanical Systems (MEMS) is a technology that was primarily developed based on integrated circuit (IC) technology at first. Because of its batch production capability, low energy consumption, and compatibility with traditional IC process, MEMS technology has found various applications in the fields of mechanical engineering, optics, chemistry and biologics.

The development of MEMS technology can be dated back to 1950s. The discovery of piezoelectric effect in silicon and germanium announced the birth of micro--sized silicon strain gauge, which is also generally considered the birth of modern MEMS technology [1]. Not far after this, Dr. Richard Feyman, in his famous talk "There's plenty of room at the bottom", described the tremendous potentials in the micro technology field [2]. Since then, MEMS technology has drawn enormous research interests, and therefore experienced great growth both in academia and industry. Some remarkable MEMS products have been developed in the past decades: in 1970, the first MEMS silicon accelerometer was demonstrated by Kulite Inc.; in 1990, the first electrostatic-comb drive lateral actuator was described by Tang *et. al.*[3]; in 1994, the first digital mirror display (DMD) based digital light process (DLP) was demonstrated by Texas Instruments Inc; and in late 90s, bio-MEMS and optical MEMS started to gain significant importance and visibility in the MEMS community and are continuing their prosperity ever since.

1.2 Polymer Based Microfabrication

Since it originated from IC fabrication and greatly benefited from the well-studied silicon

material science, microfabrication, in its early days, was performed almost solely on silicon substrate. Although silicon based microfabrication has gained tremendous interests and development, its application is significantly limited by the material properties of silicon, such as optical non-transparency, mechanical frangibility, poor electric insulation, and relatively high fabrication cost. In recent years, with the advances in organic chemistry and microfabrication equipment, polymer microfabrication technology has become very popular. In comparison to silicon substrate, polymers offer several advantages: most polymers used in microfabrication are transparent; large pool of different polymers with specific properties are available; and also the cost can also be significantly lower [4].

1.2.1 Using Cured Photoresist as Structural Material

Even in silicon based microfabrication process, photoresist is used to for a pattern transfer purpose only and needs to be removed from the substrate later. It is therefore primarily used as an intermediate material. In the last decade, as progresses have been made in MEMS field to fabricate non-silicon microstructures and devices as demanded by many applications, lithography of ultra-thick photoresists has attracted many researchers. Among the thick resists that have been used, two of the most popular ones are SU-8 and Poly (methyl methacrylate) (PMMA).

SU-8 is a negative tone, epoxy type, near-UV photoresist. It can be fabricated as thick as 2mm with aspect ratio up to 25 by a standard UV-lithography process [5]. Crosslinked SU-8 polymer has Young's modulus of 4.4 GPa and poission ratio of 0.22. The cured SU-8 polymer is transparent in a relatively broad wavelength range. These properties make SU-8 polymer suitable for various applications. Yang and Wang demonstrated an SU-8 polymer out-of-plane microlens array made with a direct UV lithography technique [6], where the resulting microlens has its

optical axis parallel to the substrate. Dai and Wang reported a method to selectively metalize cured SU-8 surface [7], which can greatly broaden the application scope of SU-8 polymer. An SU-8 comb drive actuator based on this selective metallization technology is also reported [7].

PMMA is a positive tone photoresist often used in X-ray lithography and e-beam lithography processes. During an X-ray lithography process, soft X-rays shines on PMMA sheet through a special mask, the exposed PMMA material can be removed in developer and the unexposed area remains. Since X-rays have a large depth of field and a very low diffraction limit, microstructure with ultra-high aspect ratio and fine lateral resolution is achievable. PMMA, due to its high transparency, is an important polymer in optical applications. Researchers have used X-ray lithography and reflow process to obtain micro lens with high numerical aperture [8] [9]. X-ray refractive lenses made of PMMA were also reported [10] [11]. It is also worthy mention that PMMA X-ray lithography is an essential step in the LIGA (German acronym for X-ray lithography, electroplating, and molding process) process. Although X-ray lithography has some unique advantages over UV-lithography, its application is highly limited by the cost and availability of X-ray light source.

1.2.2 Direct Micromachining on Polymer Substrate

With the advancement of material science and machining technology, direct machining can now reach micrometer scale resolution. Micromachining technologies that are commonly used in polymer fabrication are briefly discussed below:

- **Micro Milling:**

Micro milling system uses a rigid drill bit with micro-size tip to constantly scratch on the substrate surface to make fine patterns, and the substrate is often mounted on a precision stage. With a computer numerical controlled (CNC) system, one can import a design from a CAD file

and have the micro milling system fabricate the microchip automatically. With the limit of drill bit and stage movement, practically lateral resolution is well beyond 10 μm [12] [13]. Although it's considered low resolution comparing to lithography, micro milling can be a flexible and quick tool for micro device prototype fabrication, especially for microfluidic devices. Mei and coworkers developed a microfluidic reactor using micro milling for luciferase detection [14].

- **Focused Particle Beam Ablation:**

Another micromachining technique is the focused particle beam ablation method. This high-energy beam can be a laser beam, a focused ion beam (FIB), or other high-energy particle beam. In the laser ablation process, a laser source with short pulse width is desirable. Ultra-short pulse (pico to femto second) laser can have very high peak intensity, and since the pulse width is so short, thermal effect at the adjacent area is negligible, which is essential for the resulting feature surface quality [15] [16]. The principle for FIB micromachining process is similar to laser ablation, high energy ion beam is focused on and bombards the substrate surface to remove the target material by sputtering action [17] [18]. Currently, the FIB micromachining system is often integrated in FIB microscope with the ion gun shared by both the imaging and the machining units. The machining process is a relatively time consuming process and can only be done in a small area. FIB machining directly on polymer is therefore rarely used because of the high cost.

- **Replica Molding and Hot Embossing:**

Replica molding and hot embossing are both techniques to transfer the microstructures on the master to a polymer substrate. Since only the master needs to be fabricated using a microfabrication process, replicas can be made in a very cost-effective fashion. Poly(dimethylsiloxane) (PDMS) is the most popular polymer material for the micro replica

molding process [19] [20]. For the PDMS molding process, the molding master is often fabricated with SU-8; PDMS prepolymer is in liquid state and can be poured onto the master pattern and ensure conformal covering; after a short thermal curing, the solidified PDMS elastomer can be easily peeled from the master. This process in not only suitable for micro patterns but can also be applied to nano patterning [21].

Hot embossing is a technique of imprinting microstructures on a substrate (usually polymer) using a master mold. In a typical hot embossing process, the polymer substrate and the master mold are heated up to a temperature above the glass transition temperature (T_g) of the polymer; force is then applied to press the polymer against the master mold; after certain contact time, the system is cooled below T_g and polymer substrate is released with a negative microstructure replica [22]. Comparing to other polymer microfabrication techniques, hot embossing can have a large selection of substrate materials, equipment can be relatively cheap and productivity is very high. Thus, it is widely used in BioMEMS and optical MEMS applications.

1.3 Brief Introduction for BioMEMS and Optical MEMS

1.3.1 BioMEMS

The BioMEMS, or Biomedical Microelectromechanical systems, are a specific class of micro devices or systems used for biological/medical applications. They are typically built on a microchip platform fabricated by MEMS technology. Polymer-based microfabrication technologies provided possible methods to fabricate microchip with bio-compatible polymers. The ultimate goal for BioMEMS is to include sample preparation, fluid handling, chemical reaction, separation and final detection in a single microchip, thus the concept known as micro

total analysis system (μTAS) or lab on a chip (LOP).

Sample preparation is the first step in a μTAS process and is specific to different applications. Wang and coworkers performed sample preconcentration on a microfluidic chip using an electro kinetic trapping mechanism enabled by nanofluidic filters. Collection and trapping can be maintained for several hours and concentration factors as high as 10^6-10^8 can be achieved [23]. An interesting mechanical cell lysis system was reported by Di Carlo *et al.*. They utilized the well-known scalloping effect in the deep ion reaction etching (DRIE) process to fabricate "nanoknives" on the side wall of their cell filter and cells were broken by nanoknives while passing through filter structures [24].

After sample preparation, the sample and chemical reagent need to be delivered to the reaction site on the microchip. Electrophoresis is one of the most popular techniques to directionally deliver the reagent. Joseph Wang *et al.* employed electrophoresis to inject antigen and antibody onto a microchip for immune assay application. It is found that under the same electric field strength, free antibody and antibody-antigen complexes have different migration times and can be separated [25]. Yi and coworkers developed a method to generate uniform micro-sized droplets containing latex particles in a micro fluidic chip [26]. These droplets have the potential to be utilized as not only the sample delivery vehicle but also the reaction site. Unger et al. reported a technique to integrate elastomer pneumatic valve into a micro fluidic network [27]. By controlling the pneumatic valve, fluid in the micro channel network can be manipulated. And interestingly, multiple valves opening and closing in a specific sequence can form a fluid pump and deliver the reagent into the target site.

One of the main advantages to scaling down a conventional chemical bench into a microchip is the higher reaction rate due to the fact that less diffusion time is required in a micro-

sized channel. Since the flow in most micro fluidic channels has very low Reynolds number and is therefore mostly laminar, the mixing / reaction process is diffusion limited. Effectively mixing several reagents in a micro channel is therefore a challenging task in BioMEMS. Yang et al. developed a micro mixer using tilted UV lithography [28]. Pre-mixing reagents are injected into the mixing chamber at opposite directions through two arrays of micro nozzles. Flow jets impinge face to face to introduce turbulence and help the mixing process.

Separation in a micro fluidic device can be accomplished by various means, such as particle sorting, electrophoresis, chromatography and others. Yamada and Seki [29] found that, with small size branch channels on the main channel, only the carrier fluid but not the micro size particles in the fluid can be dispensed from the main channel (even if the branch size is bigger than the particle diameter). When the branch size became bigger, small particles started to come out from the branch and eventually bigger particles were dispensed through the big branches. With this mechanism, they can successfully separate particles at different size. Electrophoresis is also popular, and Wang et al. demonstrated a microchip based immunoassay using electrophoresis for antibody and antibody-antigen complex separation [25]. Chromatography also has its application in lab-on-chip devices. Three tryptophan containing peptides were separated using electrochromatography performed in a sol-gel column and detected by UV absorbance [30].

The final and arguably the most important step in a μTAS is the on-chip detection system. Electrochemical detection, fluorescence detection, non-fluorescence optical detection and mass spectrometry are some of the detection methods often adopted in μTAS chip. Wang et al. utilized an off-chip three electrode system to conduct amperometric measurements for a micro-chip immunoassay [25]. Garcia and coworkers integrated two gold wires into a PDMS

based micro fluidic chip for amperometric measurement to detect underivatized carbohydrates, amino acids, and sulfur-containing antibiotics [31]. On-chip fluorescence detection is another feasible solution, however, the integration of optical elements into the micro fluidic chip is still difficult. Roulette et al. made attempt to integrate a microlens and inference filter into a fluidic chip [32]. We have also successfully integrated out-of-plane micro lens into micro fluidic channel walls, more detail about this work will be discussed in chapter 3.

1.3.2 Micro Opto-Electromechanical Systems (MOEMS)

MEMS fabrication techniques are often used to make micro-sized sensors and actuators, also called transducers. In optics, sensors are used to detect light signals while actuators are responsible for modulating and delivering light signals. Comparing to other MEMS applications, the technology of micro-opto-electromechanical systems (MOEMS) already has a stable and growing market [33]. Due to the fact that design and fabrication of MEMS devices are performed in micro-scale, which is very close to light wavelengths (380nm-750nm for visible spectrum), MOEMS has an intrinsic advantage in optical applications. A brief introduction of MOEMS in different sub-fields is presented in the following sections.

- **MOEMS in Optical Communication:**

The advancement of MEMS technology has greatly pushed forward the development of optical fiber communication, at the same time, the demand generated from fiber communication has brought MEMS technology new opportunities and challengers [34]. MEMS based key optical communication components, such as data modulator [35], variable optical attenuator [36] [37], optical switch [38-40], add/drop multiplexer [41] [42], spectral intensity filter [43] and cross connectors [44] have all been demonstrated. Some of them have already been commercialized. These developments will eventually lead to the miniaturization and integration

of current optical communication components.

- **MOEMS in Display:**

Display is another field where great application has been found for MEMS optical devices. Two main technologies here are Digital Mirror Device (DMD) from Texas Instrument and Grating Light Valve (GLV) from Silicon Light Machine. DMD was first invented by Dr. Hornbeck in 1984. A dense array of aluminum micro mirrors is fabricated on a completed CMOS memory chip. Each mirror is individually addressable with the 5V CMOS voltage and can be tilted to either 10^{o} (on) or -10^{o} (off) position. In "on" position, the light reflected by the individual mirror passes through the imaging system and generates a bright pixel on the screen; while in "off" the reflected light cannot pass through the exit pupil, thus a dark pixel is generated. Since the actuation time for the mirror is on the micro second level, binary pulsewidth modulation of the incident light can be achieved to generate gray scale pixels. Color is accomplished with the assistance of color filters [45]. GLV is another MEMS based display technology. Each pixel includes an array of high reflective silicon nitride ribbons coated with aluminum. In the rest state, light is directly reflected from the ribbons and blocked at the reflect angle to generate a dark pixel. In the on state, alternative ribbons are pulled down by ¼ of the light wavelength. Because of diffraction, output light in this state is diffracted into a certain angle and can be focused onto the screen to generate a bright spot [46].

- **MOEMS in Biomedical Applications:**

Optical MEMS also has major applications in the bio-medical field. One of these is the optical detection components in micro fluidic devices which are covered in the previous section. Other than that, some other interesting applications are worth mentioning here. Scanning micro mirrors have been adopted into miniaturized endoscope for non-invasive optical biopsy [47]

[48]. Xie and coworkers have reported a MEMS endoscope with integrated scanning micro mirrors. Low-coherent light is split into two beams, one goes through the reference arm and the other one is reflected by the micro mirror and scans on the target. Reflected or scattered light from the target is later combined with the light from the reference arm to generate an inference pattern similar to that in a Michelson interferometer. Information about the target tissue can be obtained by monitoring the change of the interference pattern [47]. Changho's approach is similar to He's, however, a longer wavelength light was used to generate driving current for the micro mirror and thus optical modulation of the mirror movement was achieved.

1.4 Scope of the Research

The research work presented in this dissertation has focused on the microfabrication of polymer based microstructures and devices. SU-8 negative tone photoresist, PDMS silicone elastomer and UV curable polymer (NOA series, Norland Products Inc., Cranbury, NJ) are the polymers used for most fabrication process. Three polymer-based MEMS applications, including a micro optics component and two micro fluidic chips for BioMEMS applications, are investigated.

In chapter 2, two novel methods to fabricate out-of-plane microlens arrays are described. In the first method, an out-of-plane micro lens array master mold was fabricated using the SU-8 tilted UV exposure technique. PDMS was molded against the SU-8 master to generate a PDMS negative mold and out-of-plane microlens arrays made of other curable polymers were achievable with another molding process with the PDMS mold that was reusable. The whole replication process was very time-effective and can be finished in less than 5 hours including PDMS mold fabrication or 30 minutes with a PDMS mold already available. In addition, this technique allowed more polymer materials to be used for out-of-plane microlens fabrication,

which was very important due to the limited optical properties of the cured SU-8 polymer. The second method relies on the deformation of PDMS membrane under pneumatic pressure. Thin PDMS membrane vertically embedded in microchannel (at the location of the final lens) is fabricated using ordinary soft lithography technique. Pneumatic pressure is then applied on the membrane to cause deformation. With high refractive index polymer (e.g. UV polymer) filling in the lens body, an out-of-plane microlens can be fabricated in an in-situ fashion.

In chapter 3, the research work to develop a micro flow cytometer with an integrated three-dimensional hydro-focusing unit and an out-of-plane microlens array is presented. As an important component in the on-chip optical detection system, an out-of-plane microlens array was embedded in a fluid channel wall and prealigned with the output optical fiber fixed in the V-shape groove. Optical Simulation results confirmed that an integrated microlens can substantially improve the detection efficiency by effectively coupling fluorescent light from the sample cells into the output optical fiber. A preliminary cell counting test was also performed to prove the feasibility of the proposed micro flow cytometer design. A simple theoretical model based on mass conservation is developed to predict the final width of the focused sample stream. Based on the theoretical analysis, an optimized hydrofocusing chamber made in PDMS is also designed and fabricated. The new chamber has vertical hydrofocusing elements at both the bottom and the top to make the vertical hydrofocusing more symmetric and better confine the sample stream at the center of the outlet channel. Experimental results confirmed that the new hydrofocusing chamber is capable of generating a focused sample stream with width as low as 10 μm.

In chapter 4, a PDMS based multiplex immunoassay is proposed for high throughput multiple target detection. The PDMS microchip includes two layers, the microfluidic layer and the micro valve control layer. The micro pneumatic valves can be open and closed individually

by controlling the corresponding air chamber. Fluid flow in the micro fluidic layer can then be manipulated by the valves, also contamination is greatly reduced with closed valves separating different reaction sites. Initial experiments have been conducted to prove the feasibility of doing ELISA (Enzyme-linked immunosorbent assay) with PDMS as the substrate. A microchip has been successfully fabricated with the PDMS soft lithography process and proper valve control was achieved. More work will be done to conduct on-chip immunoassay process and study the achievable detection limit. Possible integration of on-chip detection components is also in consideration.

CHAPTER 2. FABRICATION OF OUT-OF-PLANE POLYMER MICROLENSES

2.1 Introduction

With the development of microfabrication technology, especially polymer based microfabrication, Micro-Opto-Electro-Mechanical Systems (MEOMS) technologies have experienced a dramatic advancement in the past decade.

Microlenses, as a key component in micro optics systems, have found applications in optical communication [49], integral imaging systems [50, 51], backlight illumination enhancement in OLED display systems [52], and lab-on-a-chip systems [53], etc.. The most popular technique for refractive microlens fabrication is the well-known reflowing process [54, 55]. Briefly, an array of micro-sized photoreist cylinders is formed after lithography and treated at an elevated temperature. If the temperature is higher than the polymer's glass transition temperature, photoresist cylinders are melted and reflow to form curved microlenses due to surface tension. Although the reflow process has been a well-studied microlens fabrication technique, it is limited to fabrication of an in-plane microlens, i.e. the resulting microlens has its optical axis perpendicular to the substrate.

In applications like free space optical interconnection and on-chip optical detection, it is often desirable to have an integrated out-of-plane microlens that has its optical asix parallel to the substrate. Previously, hinged microlenses have been used to form out-of-plane microlenses [56]. These lenses were typically fabricated using in-plane technologies and suspended with a mechanical hinge. They were then driven up to the required vertical position either electrostatically or electromagnetically. The main drawbacks of the hinged microlens are the poor stability of the resulting structures and the tedious assembly process. While early out-of-

plane microlenses were mostly fabricated using silicon bulk fabrication technology, polymer microfabrication has become the dominating technique in out-of-plane lens fabrication in recent years. Liang and co-workers [57] confined a liquid slug in a microchannel, by applying slight pressure at one end of the slug, they obtained parabolic surface profiles of at both ends of the liquid slug due to surface tension at the liquid-air interface. A similar approach was adopted by Lien *et al.* [58], instead of using liquid slug, they injected PDMS prepolymer into PDMS microchannel and defined the radius curvature of the surface profile by chemically treating the channel wall.

2.2 Fast Replication of Out-of-plane Microlenses with PDMS and Curable Polymer

Our group has previously reported a tilted UV lithography method to directly fabricate out-of-plane microlens with negative tone photoresist SU-8 [6] [59]. An out-of-plane microlens array with nearly-spherical micrlens pixels was successfully fabricated with this method. However, there are two disadvantages with the previous technology. First, the use of an ultra-thick (>500μm) SU-8 photoresist layer and multiple tilted UV exposures made this process a time consuming one. It took more than two days to finish the whole process and expensive photo-lithography process equipments was necessary. Secondly, microlenses can only be made of SU-8 polymer which is essentially a photo sensitive material and has limited optical transparency. It has been observed that aged SU-8 polymer turns to reddish color. A fast and low cost out-of-plane microlens fabrication technology which can be used to make microlenses with a broad selection of materials is therefore highly desirable.

PDMS is a silicone based elastomer. It was introduced into microfabrication in late 90s [20]. Because it is in a liquid state before curing and has a very low surface energy (essential for

demolding process), PDMS has quickly become arguably the most popular material in micro and nano-molding processes. The PDMS molding process has also been adopted into microlens fabrication [60]. However, the reported microlens fabrication processes using PDMS are all for in-plane microlens fabrication. Unlike in-plane microlenses whose relief structures are on the substrate plane, out-of-plane microlens has relief structure on the sidewall. This makes the molding of out-of-plane microlens very challenging since the lens structures may easily be damaged during the demolding process. PDMS, because of its unique properties, is a great candidate for out-of-plane molding and replication process. Before curing, PDMS pre-polymer is in relatively low-viscosity liquid state, so it can conformally cover the three-dimensional microstructures. After curing, the polymerized PDMS has good elasticity, which makes it possible to deform during the demolding process and come back to the original shape after demolding. So the negative mold can be released while keeping the SU-8 structure on the master intact.

In this section, a method which can rapidly replicate out-of-plane microlens is described. Curable polymer (e.g. UV curable polymer, poly methyl methacrylate (PMMA)) can be used to form out-of-plane microlens replica using the PDMS negative mold. This method substantially reduces the whole fabrication process from more the 2 days to less than 5 hours (master mold fabrication time not included). In addition, with a choice of more polymers for the lens material, this method has the potential to substantially improve the microlens optical properties. Although a few researchers have used PDMS molding process to replicate simple three-dimensional microstructures, it is the first time that the PDMS molding process is used for out-of-plane microlens fabrication [61].

2.2.1 Fabrication of SU-8 Master Mold

The fabrication of an out-of-plane microlens master mold was done using a tilted UV lithography process with the widely used negative tone photoresist SU-8. Details of the fabrication process has been reported by Yang and Wang [6] [59].

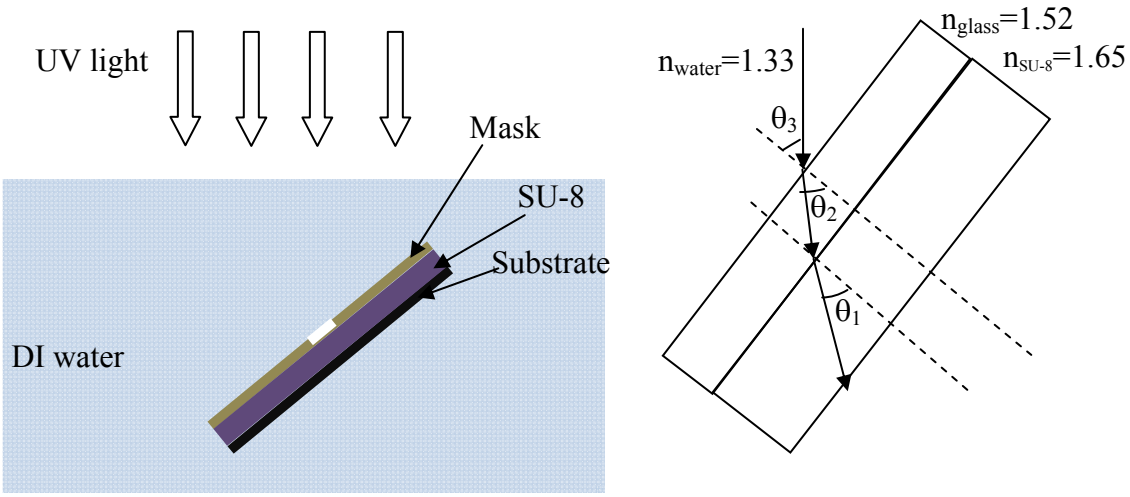

Figure 2-1 Schematic diagram of tilted UV lithography in water medium (left: the experimental setup; right: optical refraction path)

To perform the tilted UV lithography process, we chosed to use a water immersion lithography method similar to the one reported by Sato et al [62]. Comparing to prism assisted tilted UV lithography [6] [59], the water immersion approach is relatively easy to set up, and the maximum inclined angle can reach 56.2^o which is sufficient for out-of-plane microlens fabrication because only +/- 45^o inclined angles are required. Before exposure, silicon substrate spin-coated with SU-8 was fixed together with a chromium mask using a homemade clutch. As shown schematically in Figure 2-1, the clutch set was immersed in deionized (DI) water in a tilted position. The relationship between the resulting structure inclined angle and the tilted angle of the clutch set can be calculated using Snell's law. The following equation can be derived:

$$n_{SU-8}\sin\theta_1 = n_{glass}\sin\theta_2 = n_{water}\sin\theta_3 \quad (2\text{-}1)$$

Where , n_{SU-8}=1.65 [6], n_{glass}=1.52, n_{water}=1.33, are the refractive indices of uncured SU-8, glass (soda lime), and water respectively. In our fabrication process, the final structures should have -/+ 45^o inclined angles with respect to the substrate. In the diagram shown in Figure 2-1, θ_1, θ_2 and θ_3 are defined as the angles between the UV light propagation direction and the normals of the three interface planes respectively. Since the desired value for θ_1 is 45^0, θ_3 can then be calculated to be 61.26^o from equation (1). From simple geometry, it can be seen that θ_3 equals to the tilted angle of the clutch. Therefore, the clutch should be held at 61.26^o angle with respect to the horizontal plane during exposure. Since SU-8 has strong absorption to short wavelength UV light, short wavelength UV light may be absorbed only in the top layer and cause exposure non-uniformity throughout the whole photoresist thickness. For better exposure results, a piece of 1cm thick PMMA sheet (Plexiglas Grade G, Altuglas International, Philadelphia, PA) was used as an optical fileter to eliminate short wavelength spectrum of the UV light source. This PMMA sheet can block most of the UV light with wavelength shorter than 400nm. With the filter, SU-8 was only exposed by the *g-line* (436nm) and the *h-line* (405nm). Absorption of the *g-line* is much lower than that of the *h-line*, the exposure is dominated by the *h-line*. All exposure dosage mentioned in this chapter is measured at the *h-line*, unless otherwise stated.

The fabrication process for microlenses made of cured SU-8 is graphically illustrated in Figure 2-2.

(1) Substrate preparation and spin-coating: A 4 inch silicon wafer with one side polished was cleaned in acetone, isopropyl alcohol (IPA) and DI water successively. After dehydration at 180^{o}C for 30 minutes, about 16g of SU-8 100 was dispensed onto the wafer and spincoated at

460 rpm for 30 seconds to obtain an 1100μm thick SU-8 layer. Since the layer was relatively thick, no edge beads were observed after letting the sample set at room temperature for 20min. To reduce the bubble generation during the spin-coating process, SU-8 was poured onto the wafer directly from the bottle with care, and formed bubbles were pricked by a sharp needle.

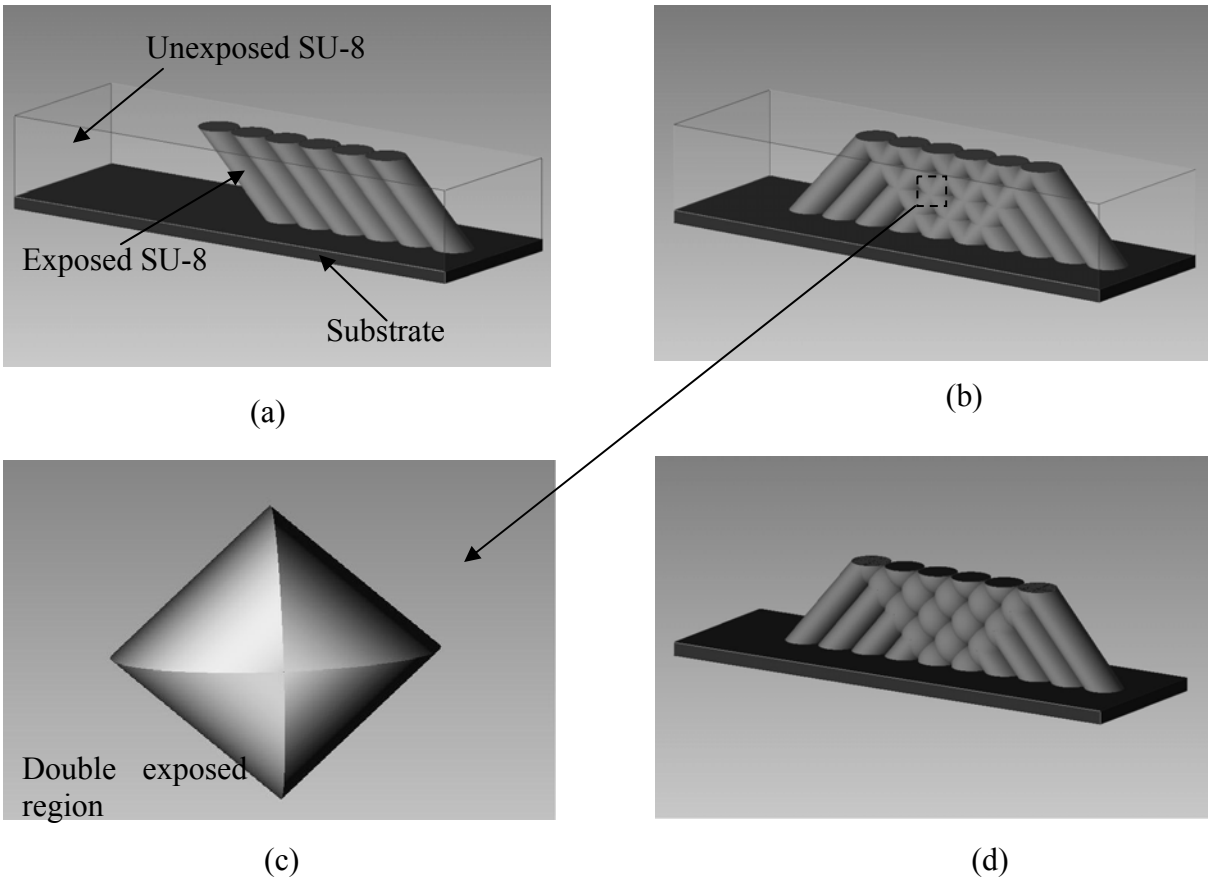

Figure 2-2 SU-8 out-of-plane microlens fabrication process

(2) Soft bake: The spin-coated SU-8 was soft baked on a well-leveled hot plate to eliminate the solvent. The hot plate has a heating part underneath the wafer which helps drive the solvent from the bottom to the top and, thus, keep the top layer soft. This is important for thick SU-8 layer soft bake since a dried top layer can prevent remaining solvent from being evaporated. To reduce the stress in the thick SU-8 layer and achieve better lithography results, multi-step ramping and stepping soft bake process is used. Figure 2-3 shows the multi-step baking process used in this

fabrication. The SU-8 layer was slowly ramped up to 110°C in multi steps and kept at 110°C for 10 hrs (for a thick SU-8 layer, the rule of thumb for soft bake time is about 1hr per100μm). The

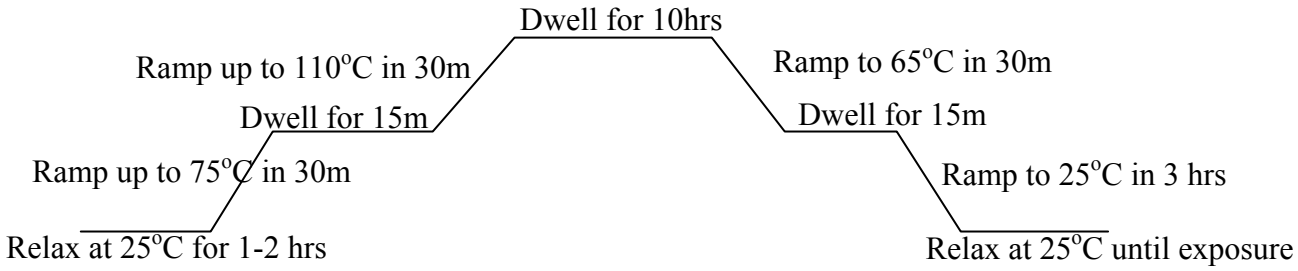

Figure 2-3 Multi step soft baking process

SU-8 layer was then slowly cooled down to 65°C. Since the glass transition temperature of uncured SU-8 is about 60°C, the cooling at around and below glass transition temperature should be done in a very slow rate to greatly reduce the internal stress in the thick SU-8 layer. 20°C per hour was used in this process. After the soft bake, surface inspection was performed. It was found that the SU-8 surface had relatively smooth surface, height deviation across the whole 4-inch wafer was less than 30μm for an 1100μm layer.

(3) Tilted UV exposure: The wafer a chromium mask were fixed together in a rotatable home-made clutch (a drop of glycerol was applied between the mask and the wafer to serve as index matching fluid) and immersed in a DI water container for the first 45° tilted UV exposure as described in the previous section (Figure 2-2 (a) shows the result after first exposure). After about 2 minutes relaxing, the whole set was put in an opposite direction for the -45° exposure (Figure 2-2 (a) shows the result after second exposure). At each intersection area of two exposure beams, a four faced double exposed region was obtained as shown in Figure 2-2 (c). 4.5 J/cm^2 exposure dosage at 405nm was used for each exposure. The dosage was experimentally optimized so that even the double exposed regions were still slightly under exposed, which was important for resulting of microlens with smooth surface. All UV exposures were performed

using an Oriel UV exposure station (Newport Stratford, Inc. Straford, CT).

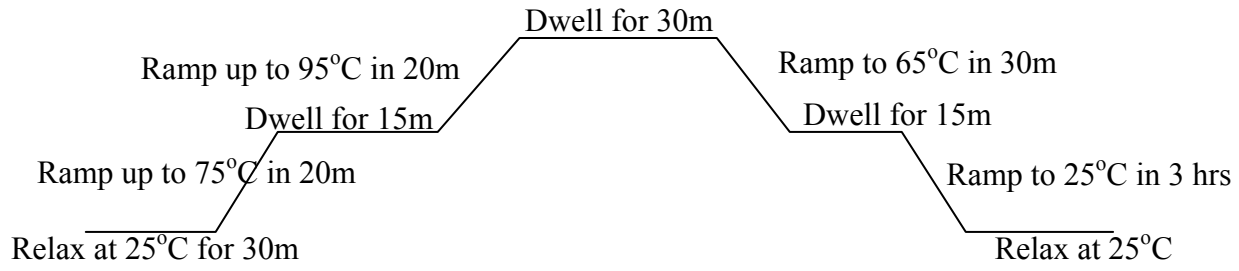

Figure 2-4 Multi step post bake process

(4) Post bake: After exposure, the SU-8 layer was post-baked to accelerate the polymerization process. Similar to the soft baking process, rapid heating and cooling should also be avoided during post baking process. As shown in Figure 2-4, the sample was slowly heated up to 96°C and kept there for 30m and then slowly cooled down to room temperature. To reduce the residual stress even more, a post bake at a lower temperature for a much longer time could also be employed.

(5) Development: After post bake, the whole sample was developed in SU-8 developer (PGMEA, propylene glycol methyl ether acetate). Because of the thickness of our SU-8 layer, a two-step development process was performed. As the first step, the sample was held facing-down in the developer for about 1 hr to solve most of the unexposed SU-8. Then, the sample was held face-up in a fresh developer solution for about 40 minutes with very mild agitation. Since the double exposed region was slight under exposed, the sharp edges of the four-faced region were smoothed out during the development process and eventually spherical microlens pixels with smoothed surfaces were formed as shown in Figure 2-2 (d). The developed sample was then rinsed in fresh SU-8 developer and dried in the hood under mild airflow. For microlens fabrication, IPA rinsing step which is widely used in SU-8 development process should be avoided since milky white spots formed on the partially polymerized SU-8 microlens surface can

cause great deterioration of its optical performance.

(6) Flood exposure and hard bake: After being dried, the sample with SU-8 out-of-plane microlens arrays is then flood exposed under the UV exposure station and baked at 95^{o}C for 1 hr. This treatment gave the final structures better mechanical stress. However, it was found during experiment that fully cross-linked SU-8 polymer turned to reddish color, which may negatively affect the optical performed of the microlens if SU-8 microlenses were directly used. For molding and replication process, the effect of this color change is negligible. SU-8 master mold fabrication was finished after hard bake process.

2.2.2 Out-of-plane Microlens Replication

PDMS molding process was used to make the negative mold from the SU-8 microlens array. Other curable polymers could then be used to cast out-of-plane microlens replica from the PDMS mold. In this work, a solvent-free UV curable polymer (NOA 73, Norland Products Inc., Cranbury, NJ) was used as an example curable polymer for demonstration purpose.

The microlens replication process is schematically shown in Figure 2-5. SU-8 out-of-plane microlens array was ready for PDMS molding after hard bake (Figure 2-5. (a)). PDMS pre-polymer mixture (Sylgard 184 Dow Corning) was prepared by mixing the base with curing agent in a 10:1 ratio. After being thoroughly stirred to ensure complete mixing, the PDMS pre-polymer mixture was placed in a vacuum chamber for 20 minutes to eliminate air bubbles. The PDMS pre-polymer mixture was then poured on the SU-8 master mold to form a 3mm thick PDMS layer. The PDMS covered wafer was then placed in a vacuum chamber for 20 minutes again to evaporate air bubbles and ensure that PDMS conformally covered the microstructures on the master mold. PDMS was then cured at 85^{o}C for 3 hours (Figure 2-5 (b)). Since SU-8 mold master with out-of-plane microlens array had micro relief structure on the sidewall, one would

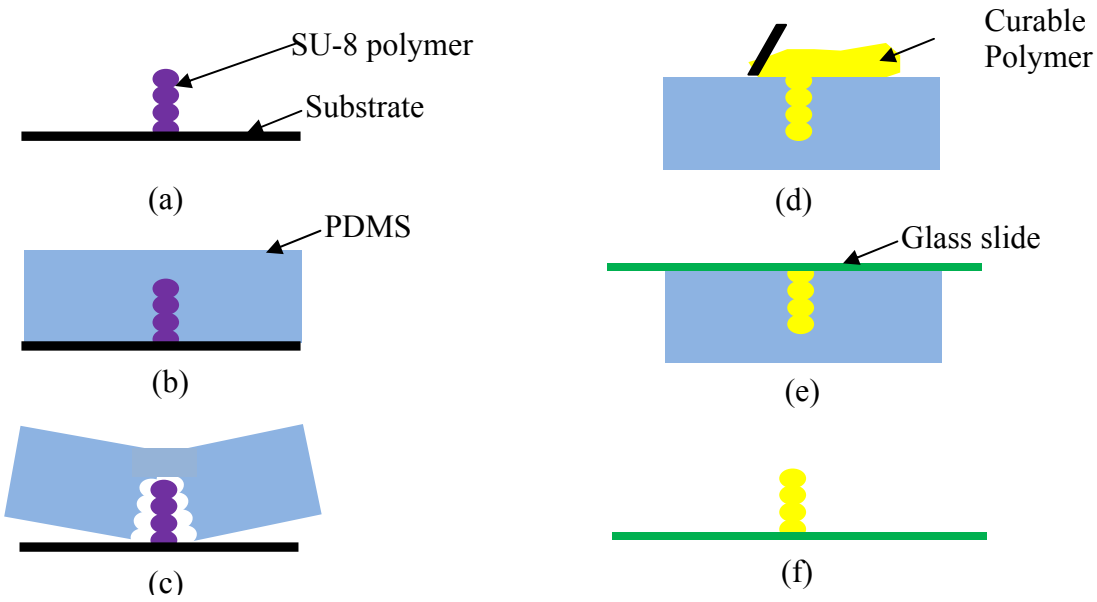

Figure 2-5 Out-of-plane microlens replication process: (a)-(c) PDMS molding, (d)-(f) curable polymer casting

have expected that demolding process might damage the master mold. However, the excellent flexibility of PDMS facilitated the demolding and made this whole process possible. Before being peeled off from SU-8 master, the PDMS mold was pulled sideways to be separated from the SU-8 microlens surface. The whole PDMS negative mold could then be peeled off from the master with ease (Figure 2-5 (c)). A calculated amount of UV curable resin (NOA 73) was then poured onto the PDMS negative mold. After vacuum treatment, excessive resin was scraped off using a clean razor blade (Figure 2-5 (d)). Comparing to other NOA series product, NOA 73 resin had low viscosity (130cps, from NOA 73 datasheet), which was very important for the resin to flow into the three-dimensional micro cavities in the PDMS mold. A microscope slide was then covered on the PDMS mold filled with UV curable resin (Figure 2-5 (e)) and exposed under a mercury lamp (Newport Cooperation, 9mw at 365nm) for 300s. After peeling off PDMS negative mold, out-of-plane microlens array replicas made of NOA 73 UV curable polymer was

fabricated on glass slide (Figure 2-5 (f)). The whole replication process took less than 5 hours (not including the fabrication of SU-8 master mold). Because the PDMS mold is reusable, multiple replications can be done use the same negative mold. In the following operations, each replication process can be completed in less than 30 minutes.

2.2.3 Results and Discussions

Using the presented PDMS molding and curable polymer casting technique, out-of-plane microlens arrays have been successfully replicated from the original SU-8 microlens arrays with no noticeable discrepancy. Figure 2-6 shows SEM images of the SU-8 out- plane microlens array

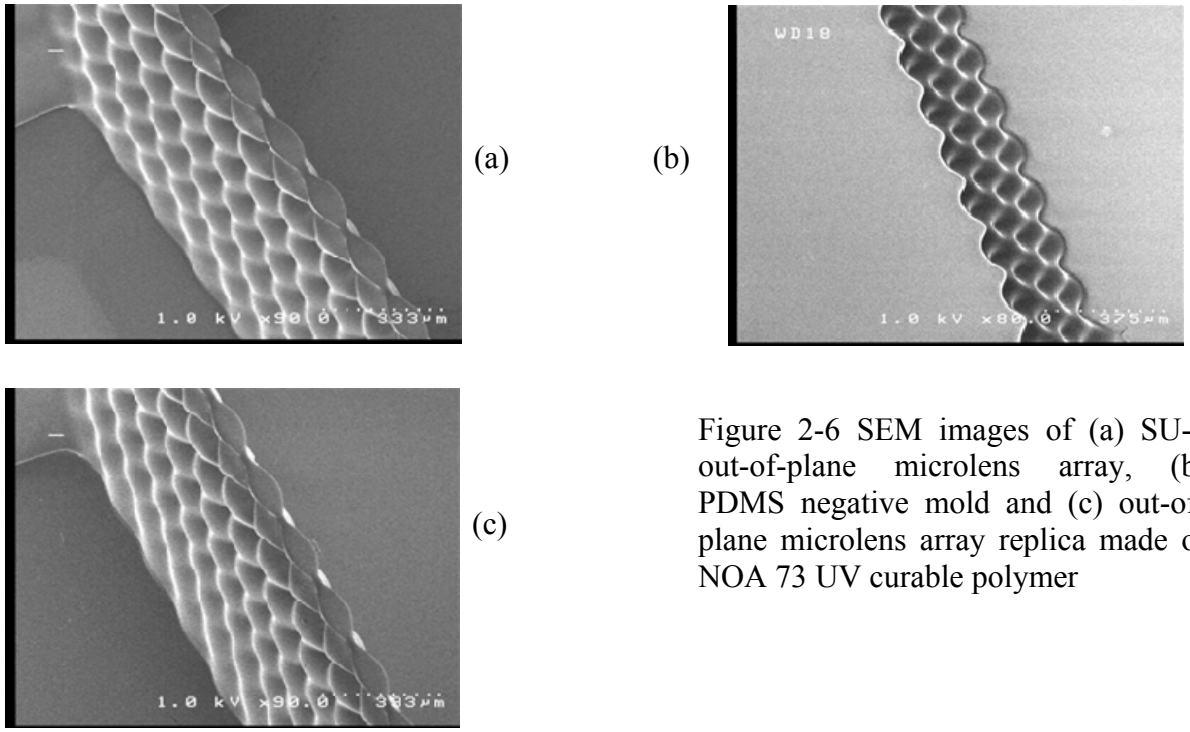

Figure 2-6 SEM images of (a) SU-8 out-of-plane microlens array, (b) PDMS negative mold and (c) out-of-plane microlens array replica made of NOA 73 UV curable polymer

(Figure 2-6 (a)), PDMS negative mold (Figure 2-6 (b)) and out-of-plane microlens array replica made of NOA 73 (Figure 2-6 (c)). From SEM images, it can be seen that microlens replica has almost identical morphology on the sidewall as the SU-8 master mold. The pixel diameters of the prototype microlens arrays range from 150μm to 350μm were fabricated and the one shown in

Figure 2-6 has pixel size of 250 μm.

NOA 73 microlens replica and SU-8 microlens master mold also have very close focal spot images (Figure 2-7). The slight differences in focal spot size and image brightness result from the refractive index and spectral transmission differences between these two polymers. NOA 73 has a lower refractive index (n_{NOA73}=1.56, from NOA 73 datasheet) compared with SU-8 (n_{SU-8}=1.65), so the resulting out-of-plane microlenses have different focal lengths and numerical

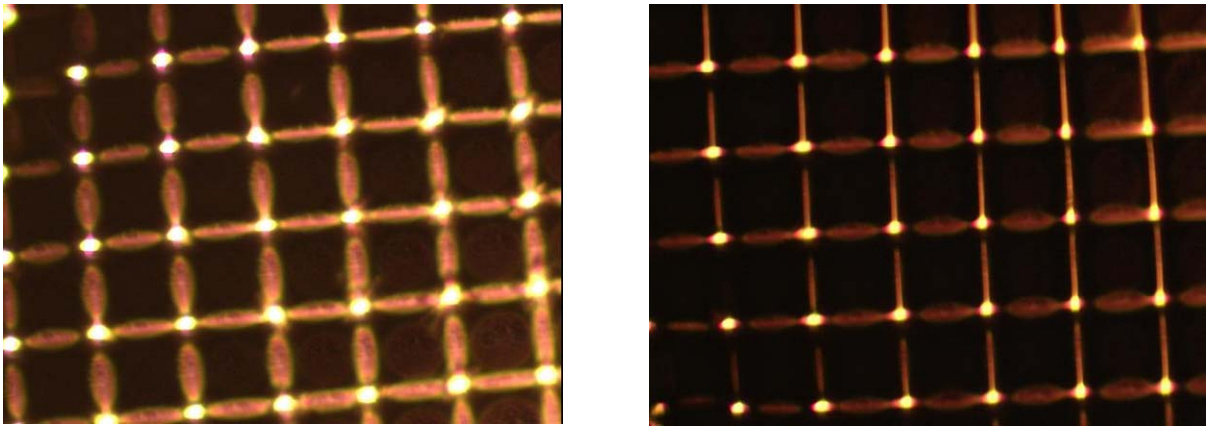

(a) (b)

Figure 2-7 Focal spot images of (a) SU-8 out-of-plane microlens array and (b) out-of-plane microlens array replica made of NOA 73

apertures. For a spherical lens, its focal length and numerical aperture can be calculated using the lens maker's equations [63]:

$$1/f = (n-1)[1/R_1 - 1/R_2 + (n-1)d/(nR_1R_2)] \tag{2-2}$$

$$NA = n_0 \sin\theta = n_0 \sin(\arctan\frac{D}{2f}) \tag{2-3}$$

Where f is the focal length; n and n_0 are the refractive indices of the lens material and medium; R_1 and R_2 are the radii of curvature of the lens front surface and back surface; d is the thickness of the lens; NA is the numerical aperture; θ is half of the maximum acceptance angle; and D is the lens diameter.

For a typical out-of-plane microlens pixel, n_0 =1.00 (air), d =300μm, R_1 =450μm, R_2 =-450 μm, D =400 μm (actual lens pixels are in square shape, inscribed circle diameter used here). Refractive index of the lens material is the only variable here. Figure 2-8 shows the relationship between lens material refractive index and focal length and numerical aperture of the resulting microlens. From Figure 2-8, it can be seen that when lens material refractive index increases,

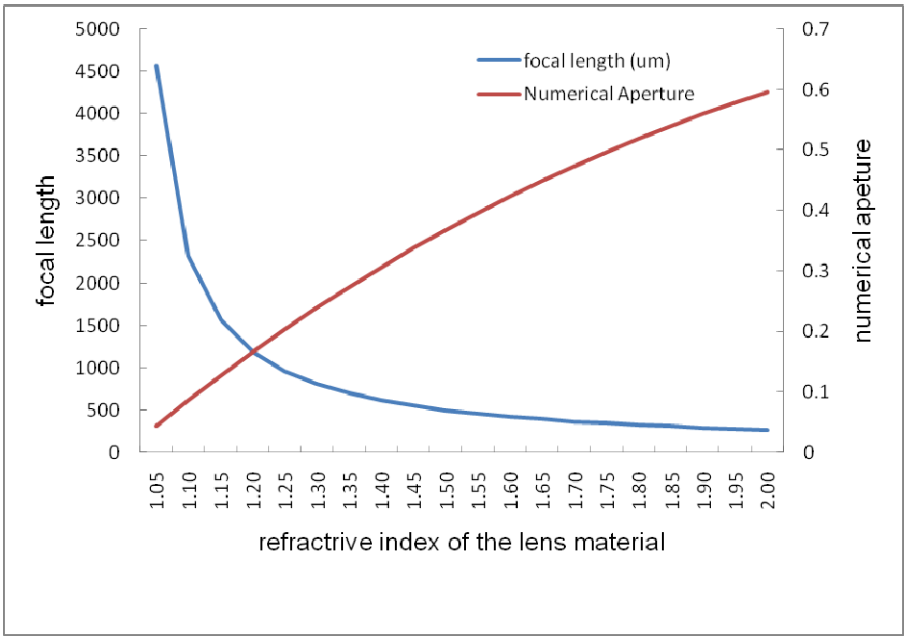

Figure 2-8 Focal length and numerical aperture for microlenses with different refractive

focal length decreases and numerical aperture increases. With NOA 73 as the lens material, the resulting microlens can have slightly longer focal length and smaller numerical aperture because the refractive index of NOA 73 is lower than that of cured SU-8 polymer.

Figure 2-9 shows the spectral transmission diagrams for cured SU-8 polymer and NOA 73 polymer (from NOA 73 datasheet). Microlens replica made of NOA 73 has broader working spectrum range in comparison with its SU-8 master mold. For cured SU-8 polymer, transmission reduces to about 70% at 450nm, while NOA 73 polymer still has 99% transmission at the same

wavelength. It should be noticed that, though NOA 73 was used as the casting material in this research, the reported molding technology should also work well with other curable polymers, such as PMMA etc. Therefore out-of-plane microlens with different optical properties may also be fabricated by choosing other curable polymers that may be preferred for specific applications.

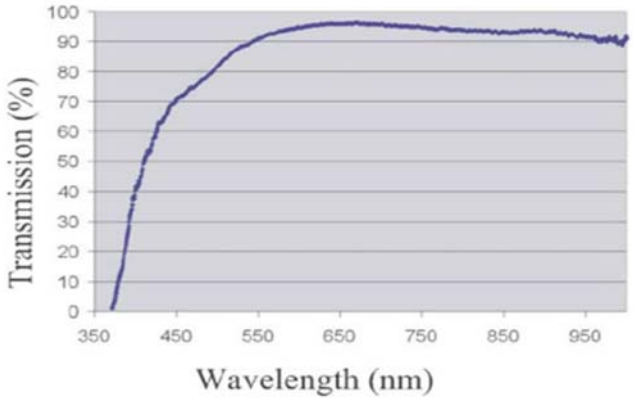

(a)

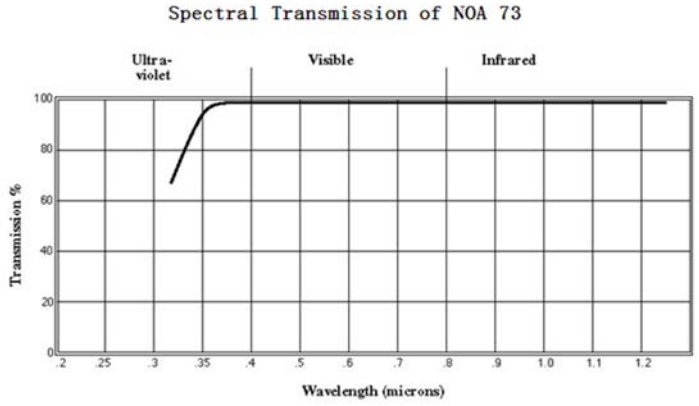

(b)

Figure 2-9 Spectral transmission of (a) SU-8 polymer and (b) NOA 73 polymer (from NOA 73 datasheet)

2.3 In-situ Fabrication of Out-of-plane Microlens in Microfluidic Chip

Although out-of-plane microlens can be fabricated easily with tilted UV lithography technique and PDMS molding process, there are several technical difficulties associated with the aforementioned technique which make the integration of a microlens into microfluidic chip not an easy task. First of all, the tilted UV lithography requires one extra mask and two extra exposure processes. Secondly, the resulting microlens surface profile can be affected by various

process parameters including exposure dosage, development time, mask design and even soft bake process, thus the theoretical study of how to precisely control the lens profile is still an on-going process. Therefore, a simple method to fabricate and integrate out-of-plane microlens into microfluidic chip is needed.

As mentioned in the introduction section, various methods has been tried to fabricate an out-of-plane microlens and integrate it into the microfluidic channel. However, Liang's liquid slug microlens [57] requires carefully applying pressure and the microlens position might be hard to control since the liquid slug is free to be move in the channel. Lien's design solved the fixing of the microlens by selectively treating the micro channel and had the cured microlens position at the interface between the treated and untreated areas [58]. But they failed to offer an easy solution to precisely position the coating site. Hsiung and coworkers reported a relatively simple way to fabricate a microlens in a microfluidic chip [64] by utilizing the membrane deformation under pneumatic pressure. However, they used index-matched liquid to fill the lens chamber and pneumatic source and lines are necessary for the lens operation. Also, the membrane they used had a rectangular shape, so the lens was strongly asymmetric. Light focusing effect was only investigated in the horizontal direction and only two-dimensional lens was claimed in their work.

Here, we developed an in-situ three-dimensional out-of-plane microlens fabrication method. This novel technique is capable of fabricating both convex and concave microlens with definable focal length at the required position in a microchip with very high precision. Its compatibility with the soft-lithography process also makes it possible to integrate out-of-plane microlens into various microsystems with minimum process complication and design footprint. By introducing curable polymer as the lens material, the fabricated microlens also does not

require any external equipments or accessories for operation, which can be a great ease for practical applications, especially those microchips used in field tests.

2.3.1 The Principle of the Fabrication Technique

The principle of this microlens fabrication technique is illustrated in Figure 2-10. A micro chamber with two thin membranes and a polymer injection channel is fabricated (Figure 2-10 (a)). Then, a curable polymer (UV curable polymer, PDMS pre-polymer, etc.) is injected into the micro chamber and can fill the whole chamber even without an outlet due to the gas permeability of PDMS (Figure 2-10 (b)). After all the residual air in the chamber is forced out through the PDMS body, appropriate pneumatic pressure is applied at the inlet end of the pre-polymer-filled microchannel (Figure 2-10 (c)). Since liquid pre-polymer can be considered as incompressible

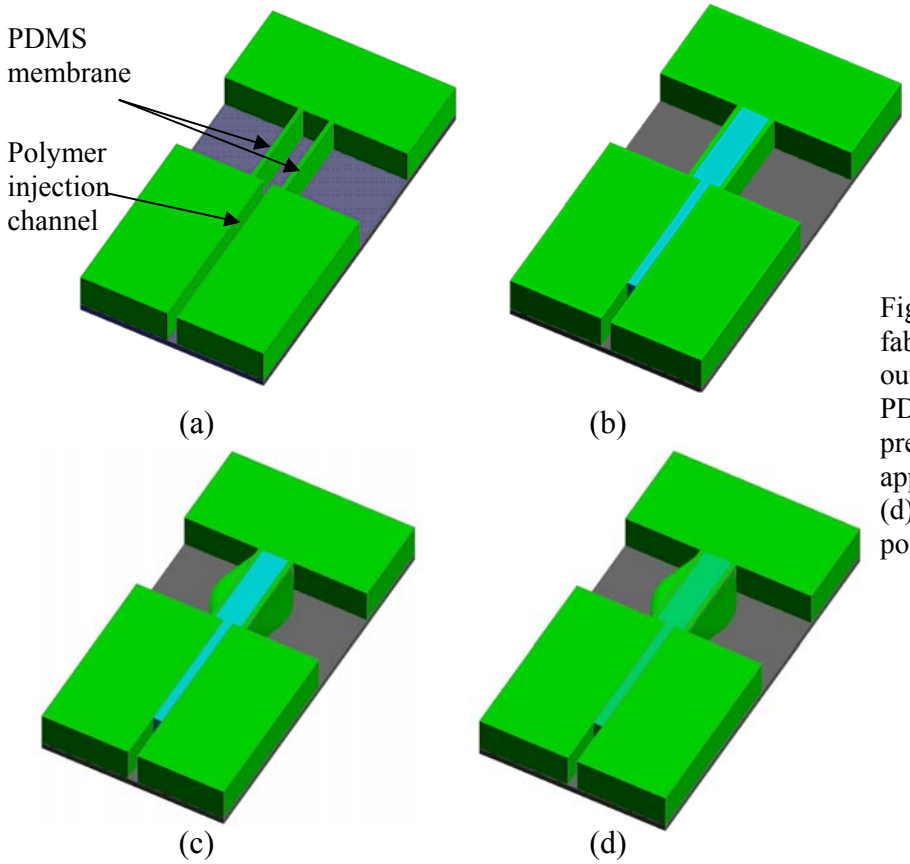

Figure 2-10 In-situ fabrication process of the out-of-plane microlens: (a) PDMS device, (b) curable pre-polymer injected, (c) applied pneumatic pressure, (d) microlens formed after polymer curing.

liquid, the pneumatic pressure at one end of the liquid can then be transferred to the walls of the liquid chamber. Two chamber side walls made of thin PDMS membrane expand under the pressure until the tensile stress of the film balances the force generated by the pneumatic pressure. The deformed membrane forms a 3-D parabolic surface profile which is suitable to be used as the lens surface. With pressure being fixed, the pre-polymer is then cured under its curing conditions. The microlens is set after the polymer curing and can be used in microchip without pneumatic pressure (Figure 2-10 (d)).

The actual microchip fabrication with the PDMS thin membrane is the same as typical soft lithography. Briefly, an SU-8 master mold is fabricated with UV-lithography. After silanization of the SU-8 master, PDMS pre-polymer (mixed at 10:1) is poured onto the SU-8 master and peeled off after curing at 80^{o}C for two hours. After boring access holes using a sharpened needle, the resulting PDMS device is then bonded onto a glass substrate or another flat PDMS slab after a brief oxygen plasma treatment (50 watt 30 second, in a Bransen plasma asher).

2.3.2 Elastomer Membrane Deformation under Pneumatic Pressure

To study the elastomer membrane deformation under pneumatic pressure and visualize the potential surface profile of our proposed microlens, a finite element analysis (FEM) software package (Stress analysis and grid deformation modules in CFD-ACE+, ESI Groups, France) was used. The Young's modulus and Poisson ratio of PDMS were obtained from other work [65] and set as 30 MPa and 0.50 respectively. A numerical simulation was performed using design presented in Chronis's work [65], the results from CFD-ACE+ is in good agreement with both simulation and experimental results presented in [65].

A typical simulation result of a thin PDMS membrane is shown in Figure 2-11. The dimension of the presented rectangular membrane is 125 μm wide, 125 μm long and 15 μm thick.

As can be seen from the simulation result, the center of the membrane can achieve maximum deflection of 15 μm under 30 psi and a smooth curved surface is formed.

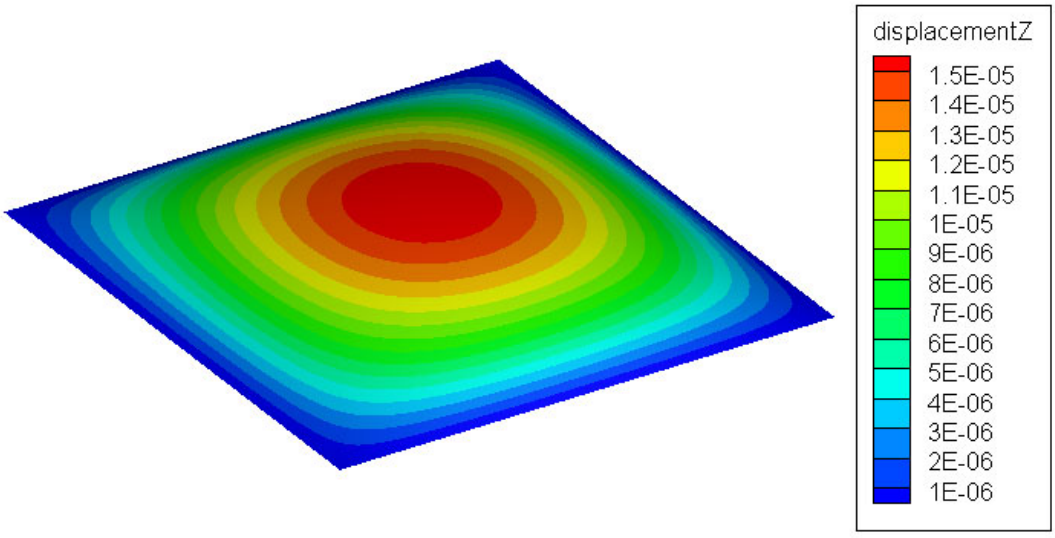

Figure 2-11 Simulation result of a rectangular PDMS film deformed under 30 psi

2.3.3 Experimental Results and Discussions

Deionized water was first used as the lens filling liquid and membrane deformation under various pneumatic pressures was observed as shown in Figure 2-12. It is clear that PDMS

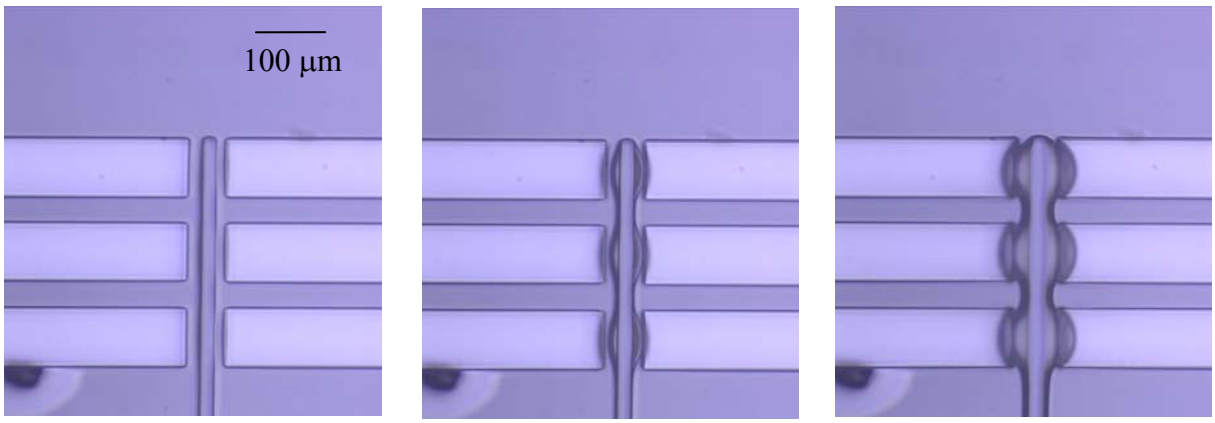

(a) (b) (c)

Figure 2-12 Water filled microlens chamber under various pressures (a) 0 psi; (b) 10 psi; (c) 50 psi. The film thickness in this device is 15 μm.

thin membrane can deform under pressure and form a curved outer surface profile. The higher the applied pressure is, the greater the deformation is. During the experiment, it was observed that PDMS/glass or PDMS/PDMS bonding interface could withstand 50 psi without leaking after more than 1 hour.

The displacement of the membrane center point on the outer surface was measured using a Nikon MU-22 measuroscope (Nikon Corp., Japan). Results were compared with the data obtained from an FEM simulation and showed a good agreement. From Figure 2-13, it can be seen that very good linear relationship exists between membrane deflection and the applied pressure at this pressure range. It is thus very convenient to precisely control the microlens surface profile by keeping the pneumatic pressure at an appropriate value.

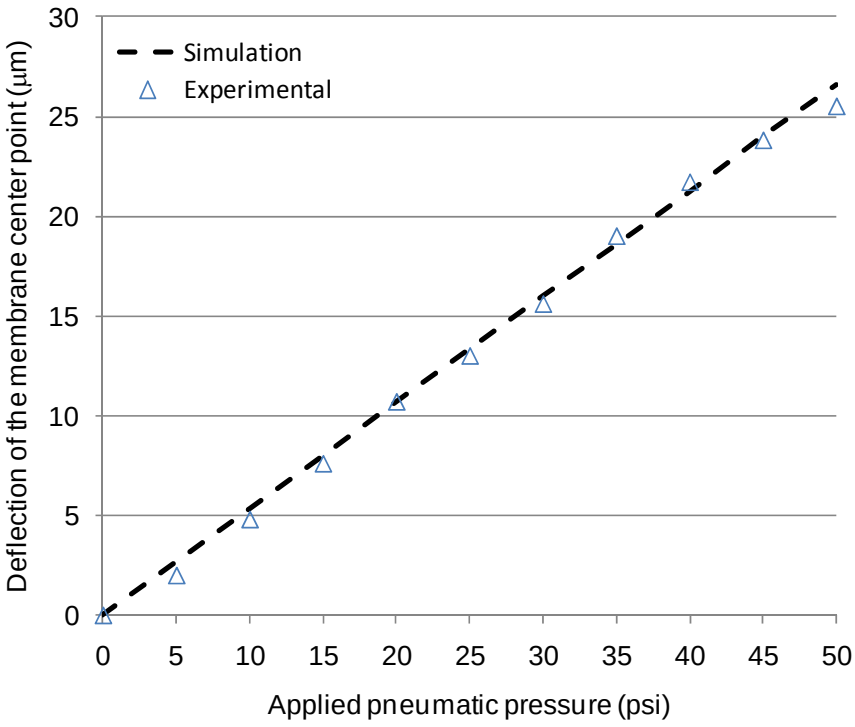

Figure 2-13 Membrane center deflection under various pneumatic pressure

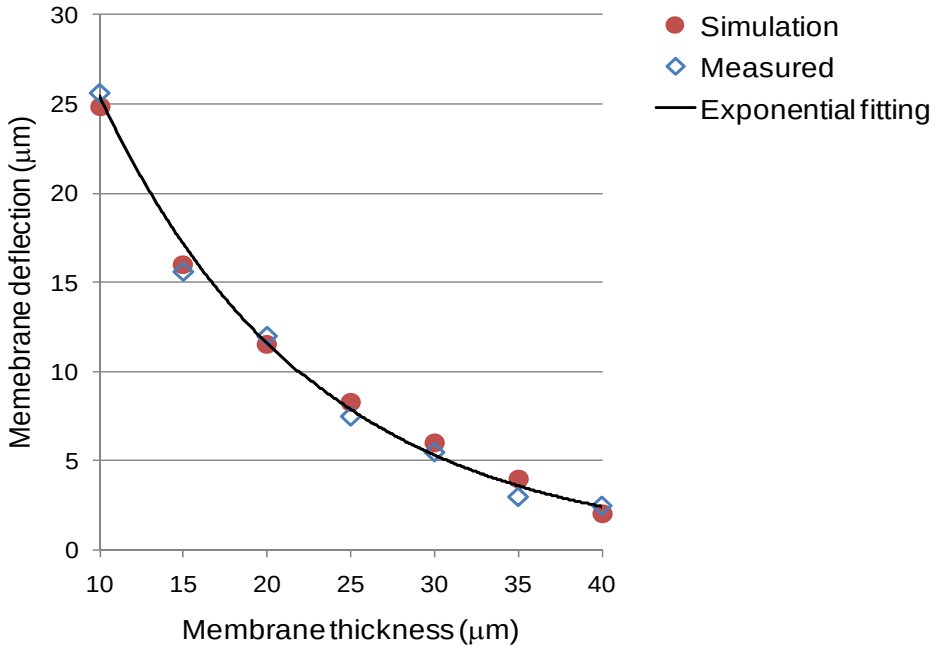

Figure 2-14 Membrane center deflection with various film thickness

Two curable polymers (NOA 73, PDMS) were used as the filling material for making the solid out-of-plane microlens. NOA 73 was selected as the UV curable polymer because of its low viscosity and good optical transparency as discussed earlier. The advantage of using NOA 73 as the curable filling material is the ease of curing. Only about three minute of exposure under a high power UV lamp (9 mW at 365 nm) was enough to crosslink the UV polymer and set the microlens. The UV cured microlens can be seen from Figure 2-15 (a). Instead of UV curable polymer, PDMS pre-polymer itself can also be used as the lens filling material. Compare to the UV polymer, PDMS takes a much longer curing time (1 hr at 80^{o}C). But the resulting microlens is made of the same material as the other components in the micro device and a homogenous microfluidic chip can be fabricated. Figure 2-15 (b) shows the resulting PDMS microlens. It should be noticed that the all-PDMS microlens in Figure 2-15 (b) shows much less contrast at the original lens chamber edges than those of the microlens filled with UV curable polymer, this can

be explained by the difference in refractive index between NOA 73 (n=1.56) and PDMS (n=1.43).

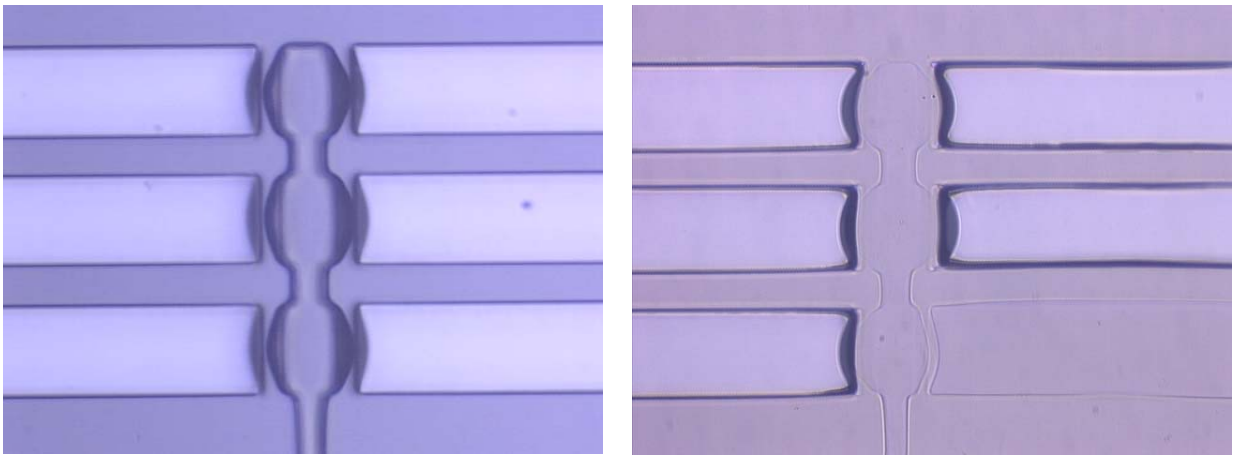

(a) (b)

Figure 2-15 Cured out-of-plane microlens (a) NOA 73 filled; (b) PDMS filled.

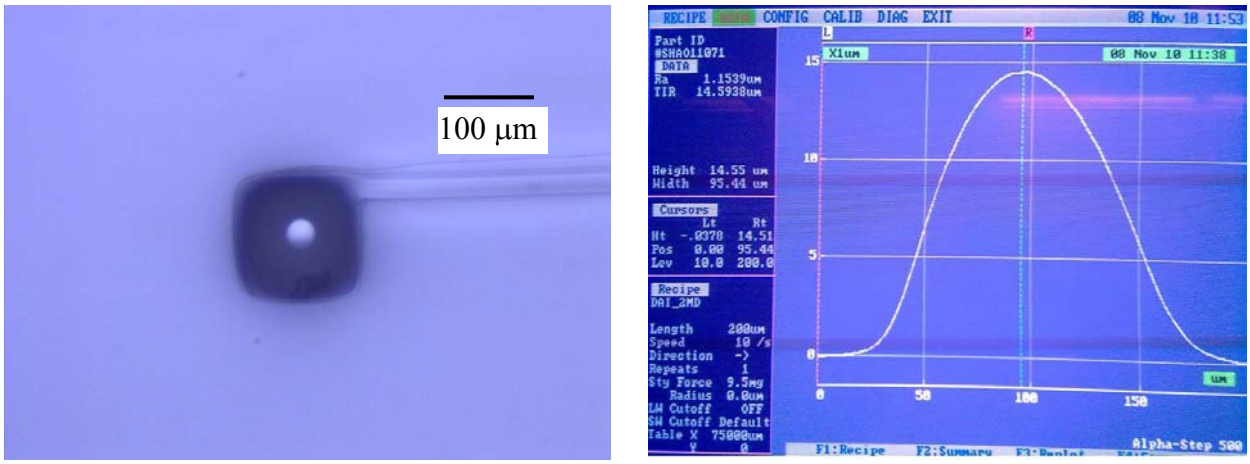

Figure 2-16 (a) focal spot of the microlens; (b) surface profile

Since the resulting microlens is embedded in the microchannel, it is difficult to investigate the microlens surface. To address this problem, an in-plane microlens with same dimensions and made using same fabrication conditions was fabricated and characterized. Figure 2-16 (a) shows a focal spot generated by the microlens by using collimated light illuminating on

the lens from underneath. Figure 2-16 (b) shows the 2-D surface profile obtained by scanning across the lens surface along the central line. The surface profile is measured using a Tencor Alpha-Step Surface Profiler.

2.4 Conclusions and Future Work

In this chapter, two integrated out-of-plane microlens fabrication techniques are presented. In the first technique, excellent flexibility and great non-adhesion properties of PDMS polymer is utilized to develop a three-dimensional soft lithography technique. An out-of-plane microlens made with the SU-8 tilting UV lithography technique is successfully replicated in UV curable polymer. Experimental results showed that the resulting NOA 73 out-of-plane microlens replicas had almost identical surface profiles as those of the SU-8 originals. Due to the difference in the refractive indices, the microlens replica had slightly longer focal length and smaller numerical aperture. In addition, NOA 73 polymer is transparent in a much wider spectral range in comparison to that of cured SU-8 polymer. This technique is good for fabricating microlens array which can be used in microfluidic chip and for free space optical interconnection systems. However, when a single lens is needed in microfluidic chip, the second method is more appropriate. The focal length of the resulting microlens can be precisely defined by keeping an appropriate pneumatic pressure during polymer curing.

With the in-situ microlens fabrication technique, out-of-plane microlenses can be easily integrated into PDMS microfluidic chips, which may open a wide range of application opportunities. In the future, more work need to be done to study the in-situ fabrication of other optical components. These works may finally make possible the integration of a total optical detection system onto an on-chip microfluidic system.

CHAPTER 3. A MEMS FLOW CYTOMETER WITH THREE DIMENSIONAL HYDROFOCUSING UNIT AND AN INTEGRATED OUT-OF-PLANE MICROLENS ARRAY

3.1 Introduction

The flow cytometer, as an important bio-research instrument, has been widely used in applications such as bio-detection, cell sorting, clinical diagnosis etc. In a typical flow cytometer, sample cells are hydrodynamically focused into the center of the flow and pass through the detection area in a single file stream. The presence of cells in the detection area generates either optical or electrical signals. Based on these signals, information about various properties of the sample cells can be obtained and analyzed.

Further applications of the conventional flow cytometer are still limited by their high cost and the lack of portability. With the development of Micro-Electro-Mechnical System (MEMS) technology, the "Lab-on-a-Chip" concept has gained great popularity [66] [67]. The on-chip integration of a flow cytometer has also attracted a lot of research interests. Lin and Lee reported a MEMS flow cytometer fabricated on glass substrate. Optical detection was carried out by inserting two etched optical fibers, one for delivering excitation light and the other one for optical signal output [68]. To improve the optical detection efficiency, several researchers have tried to introduce a microlens into micro flow cytometer as the focusing element. Wang et al. have successfully integrated a two dimensional cylindrical lens into their micro flow cytometer. The cylindrical lens was used to focus the excitation light, both forward scattering light and attenuated excitation light were detected [69]. Besides a cylindrical lens, a molded aspherical microlens was also used for flow cytometer purposes by Kou et al [53]. Although improved

detecting efficiency was claimed, the microlens was not integrated on the chip, but used in an off-chip fashion. In a recently published paper, Watkins and co-workers reported a micro cytometer with three dimensional hydrofocusing (3D) ability and a pair of integrated electrodes for cell counting purposes using the Coulter principle [70].

With typical microlens fabrication techniques, only an in-plane microlens (with its optical axis perpendicular to the substrate) can be obtained and the on-chip integration of the resulting microlens often required careful alignment and tedious assembly. Out-of-plane microlenses which have optical axis parallel to the substrate provided a feasible alternative for the on-chip integration of the optical detection system. Our group has previously reported a tilted ultra-voilet (UV) lithography technique for SU-8 out-of-plane microlens fabrication [6] [59]. With this technique, a microlens can be fabricated on the micro fluidic chip; alignment among different components can be accomplished during mask designing; and no post-fabrication assembly of optical components is required.

In this chapter, the design, fabrication and preliminary test of a micro flow cytometer with an integrated out-of-plane microlens and 3D hydrofocusing unit is described. A hydro-focusing unit design similar to the one reported by Yang et al. [71] was first tried out. An out-of-plane microlens array was embedded into a fluid outlet channel wall, the microlens can focus the fluorescent light emitted from the sample and efficiently couple the light into the output optical fiber. Preliminary test result shows that the fabricated micro flow cytometer can perform cell counting functions and generate an optical signal with a high signal to noise ratio. Based on preliminary experimental results and simulation results, optimization has been made to the hydro-focusing chamber. The optimized hydro-focusing chamber can focus the sample stream to under 10 μm, which will be suitable for high performance cytometer applications.

3.2 Chip Design and Optical Analysis

3.2.1 Design of the MEMS Flow Cytometer

A schematic diagram of the proposed micro flow cytometer is shown in Figure 3-1. The chip layout can be divided into three major areas: the fluid injection area, the hydro-focusing area and the optical detection area. In the fluid injection area, two sheath flows are injected in from inlets on two side channels, while the samples come in from the center inlet. The injected

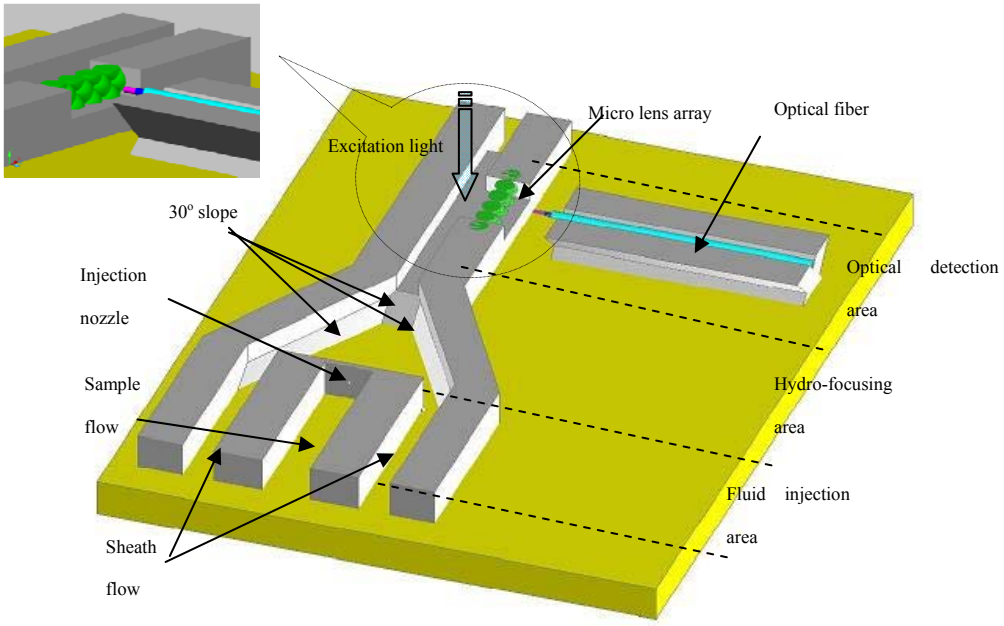

Figure 3-1 3-D layout of the designed MEMS flow cytometer

sample cells pass through the injection nozzle on the sample reservoir wall to merge into and be focused by sheath flows in the hydro-focusing area. Since the injection nozzle is at the center, sample cells enter the hydro-focusing area in an elevated position, which is helpful for vertical sample focusing at later stage. In the hydro-focusing area, the cross sectional area of the hydro-focusing chamber becomes smaller and smaller along the flow direction to help the sheath flow

squeeze samples into the center of the flow. In the meantime, three 30^o slopes (Figure 3-1) can lift up the flow before it enters the outlet channel. This lifting up provides a hydrodynamic force to move and focus the sample in the vertical direction. So by the time samples enter the optical detection area, they have been focused in both horizontal and vertical directions. To accomplish optical detection, external excitation light is focused on the samples passing through the detection area in a single file stream. Fluorescent light emitting from pre-dyed samples can be focused by the out-of-plane microlens and then be coupled into the output optical fiber to generate detectable optical signals.

3.2.2 Optical Analysis

Optical analysis is important to study the performance of the optical detection system and optimize its design. Optical simulation was done using Zemax EE (ZEMAX Development Corp., Tucson, AZ). In our system, the output multimode fiber core diameter was 200μm, which is more than 200 times greater than typical fluorescent light wavelength. Therefore enough transverse modes can be supported in the output fiber and geometrical ray tracing method can be used to evaluate the light coupling efficiency [72].

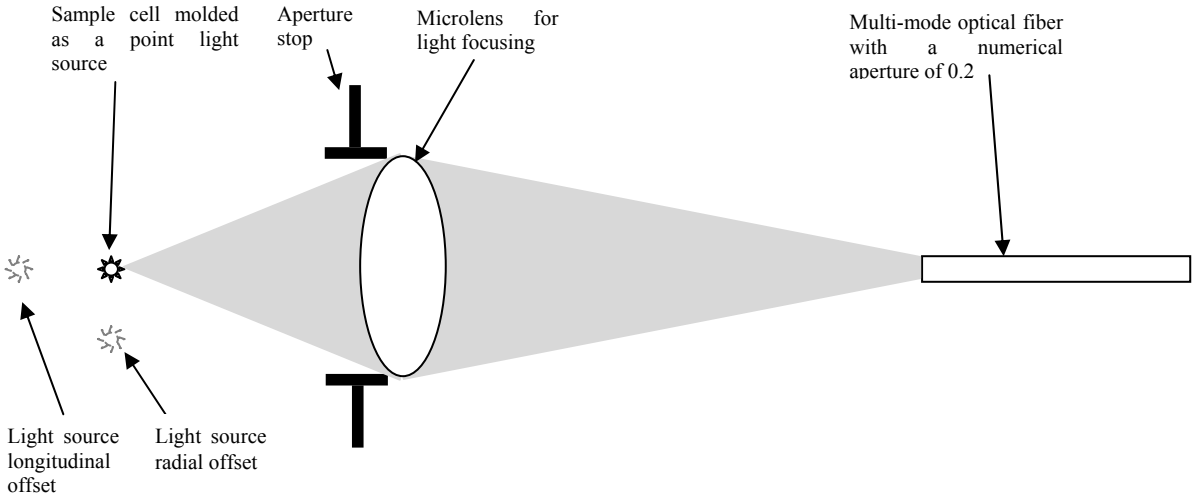

Figure 3-2 Illustration of the on-chip optical detection system

An optical system as shown in Figure 3-2 was built in Zemax. A sample cell/bead emitting fluorescent light was modeled as a point light source [73, 74]; an imaginary aperture stop was placed in front of the microlens to define the optical rays which were traced during the simulation; microlens was modeled as a spherical lens with diameter of 450μm and radius of curvatures of 380μm for both surfaces; a circular image surface with numerical aperture (N.A.) of 0.2 was defined in Zemax to model the optical fiber with same N.A..

During the simulation, Zemax randomly generated a group of rays from the point light source to fill the aperture stop; those rays were then bent by the microlens and reached the plane where the output fiber end face was; part of the rays missed the defined output fiber end face and was obviously not supported by the output fiber; among those rays that did hit the acceptance end of the optical fiber, some came in at an angle larger than the optical fiber's numerical aperture and were also be dropped; only those rays that hit the optical fiber acceptance end at an angle within its numerical aperture were supported by the output fiber and contributed to the final detection signal. By comparing the number of rays that were supported by the output fiber to the original rays filling the aperture stop, the light coupling efficiency was calculated. The optimization function built in Zemax automatically compared coupling efficiency for different microlens focal lengths, light source to lens distances, lens to optical fiber distances, etc and decided the best value for those parameters.

For comparison purposes, the light source to output fiber direct light coupling efficiency was also studied. The direct coupling system was similar to the microlens aided system shown in Figure 3-2, however, there was no focusing microlens and the optical fiber was moved to the microlens position. The aperture stop size remained the same to ensure that the same total amount of rays was used in the coupling efficiency calculation for both systems. Under the same

simulation conditions, a snap shot on the output fiber end face was taken in both systems (Figure 3-3). Each small dot in the center areas of both pictures represents a ray which was supported by the output fiber and contributed to the final optical signal. It is obvious to see that microlens aided system has much higher coupled ray density (Figure 3-3 (a)) than the direct coupling system (Figure 3-3 (b)), thus a higher coupling efficiency was achievable.

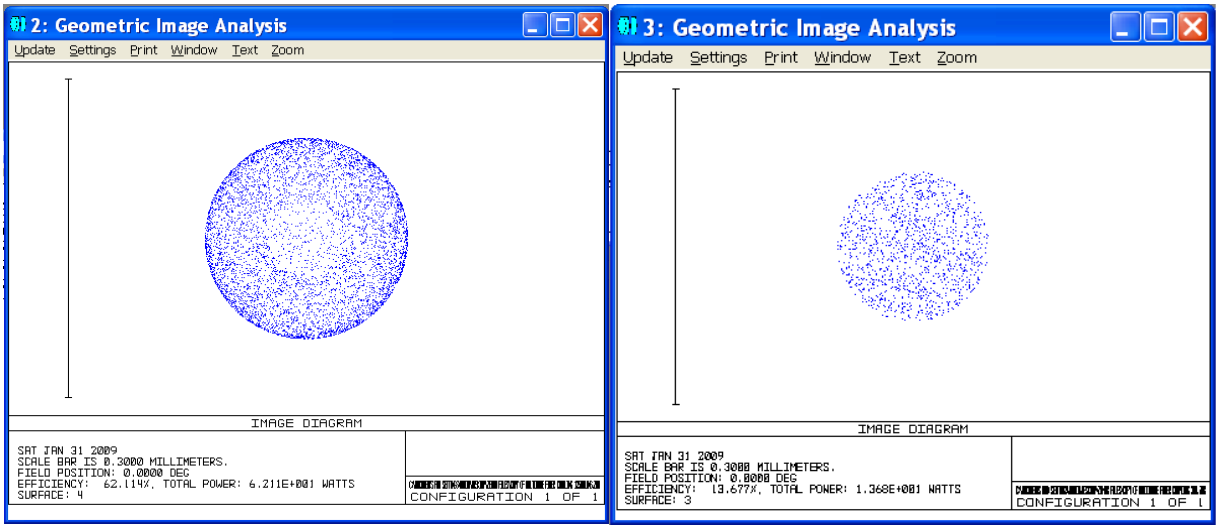

(a) (b)

Figure 3-3 Snap shots of the output fiber end face (a) in the microlens aided detection system and (b) in the direct coupling system

With a comprehensive consideration of fluid dynamics (personal communication with Dr. Udoetok), optical simulation results and fabrication feasibility, the critical feature dimensions were decided as following: all three inlets were 1000μm in both height and width; the injection nozzle was 100μm by 100μm; three slopes were inclined 30^{o} with respect to the substrate plane; the outlet channel was 500μm by 500μm; the microlens array was placed about 450μm away from the outlet channel center; microlens pixel diameters ranging from 250μm to 450μm were tried; the distance from the output fiber to the microlens back surface was estimated at about

1.5mm for the highest coupling efficiency.

Although the distance between the microlens and the sample cell light source was optimized, practically, it was very difficult to maintain the sample cells right at the center of the outlet channel. It is thus very important to study how the sample cells being off from the outlet center can affect the coupling efficiency. As shown in Figure 3-2, two types of offset were studied. The first one was the longitudinal offset caused by the slight asymmetry of two sheath flows from right and left sides. When the sheath flow from one side is stronger, sample cells, instead of being focused at the center, are pushed to the opposite side. Figure 3-4 (a) shows the relationship between longitudinal offset and the coupling efficiencies for both the direct coupling

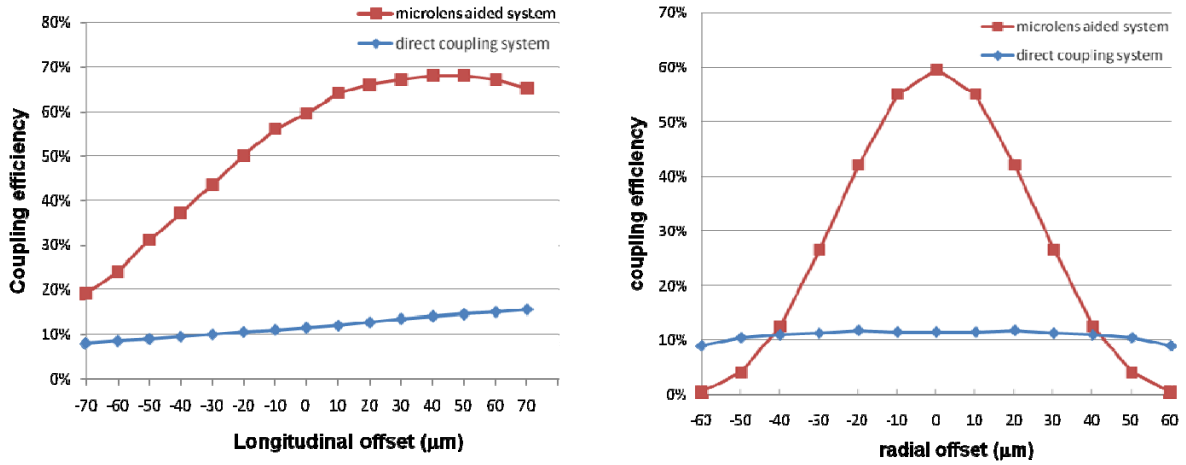

Figure 3-4 Coupling efficiency with (a) different longitudinal offset and (b) radial offset

system and the microlens aided system. For the direct coupling system, the coupling efficiency stays low but slight increases as the light source moves toward the output fiber. In contrast, with the microlens as the focusing element, the coupling efficiency is much higher. Coupling efficiency drops from about 60% to about 25% when point light source moves 90μm closer to the microlens and drops to about 40% when the point light source moves 90μm away. The other

common offset was radial offset related to the hydro-focusing in vertical direction. Non-sufficient vertical hydrodynamic force may cause sample cells being focused in a position lower than the center of the flow. As shown in Fig. 4 (b), detection system with microlens is very sensitive to radial offset, coupling efficiency drops to nearly 0 for only 60μm offset from the center. In the meantime, direct coupling system is not so sensitive to radial offset, but the overall coupling efficiency is low.

It should be mentioned that only fluorescent signal was considered in this optical analysis. The intensity distribution function for the scattering light may be greatly different from the light intensity distribution from a fluorescent bead. More sophisticated light source model should be used to analyze the coupling efficiency for scattering light. Also, since fluorescent bead is modeled as a point source, this analysis works better for fluorescent beads with diameter smaller than the diffraction limit of the optical detection system (about 1.5 μm). For larger beads, the point source assumption may cause error to the coupling efficiency, however, the efficiency trend remains the same and the result can be used as a reference for the system design [73].

3.3 Signal to Noise Ratio Analysis

When designing an optical detection system, it is important to study its signal to noise ratio performance. In a typical flow cytometer, as well as a micro flow cytometer, the noise can be categorized into optical background and electronic noise based on its source. Optical background can rise from leaked fluorescent dye in the solution, ambient light, scattering from target particle or debris in the solution, and also Raman scattering from sheath and sample medium. Electronic noise may come from electronic components used for signal conversion and acquisition, namely, the analog-to-digital converter, photon detector (photomultiplier tube or avalanche photodiode), and other electronic accessories. Since the electronic noise can be

reduced by using high-performance components and has become less and less of a problem with the advance of electronics, our discussion in this section will be confined to the origination of optical background and possible methods to reduce optical background related noise.

Among optical background sources, debris and leaked fluorescent dye should be eliminated or greatly reduced by carefully preparing the sample and sheath solution. One of the optical background sources one should pay special attention to is the scattering from the sample particle itself. In a flow cytometer, scattering on the target particle is generally an elastic process, either Rayleigh scattering or Mie scattering model can be used to calculate the scattering intensity depending on the particle size. For the elastic scattering light, its wavelength is identical to the excitation light, which normally has distinctive spectral separation from the emission fluorescent light, so its intensity can be greatly attenuated by the band-pass filter placed right before the photon detector. Take a Fluorescein isothiocyanate (FITC) dyed particle as an example, its excitation wavelength is at around 488 nm and its emission peak is at 520 nm. And the fluorescent light intensity is proportional to the illumination, absorbance, and quantum yield. The signal associated to the fluorescent intensity can be calculated as described in [75]:

$$F(\lambda_{520}) = AN\varepsilon_{ex}\phi Q(\lambda_{520})T(\lambda_{520})s(\lambda_{520}) \tag{3-1}$$

Where A includes illumination, sensing volume, and other wavelength independent parameters associated with the detection system. N is the number of dye molecules on the target particle. ε_{ex} and ϕ are extinction coefficient and quantum yield respectively. $Q(\lambda_{520})$ and $T(\lambda_{520})$ are the photo detector response and filter transmittance at 520 nm respectively. $s(\lambda_{520})$ is the relative emission function.

If the target bead is small enough so that Rayleigh scattering is the dominant scattering

phenomenon, the scattering light intensity can then be calculated as [76]:

$$I(x,\theta) = I_0 \left| \frac{n^2 - 1}{n^2 + 2} \right|^2 x^6 \frac{1 + \cos^2 \theta}{2k^2 r^2} \tag{3-2}$$

Where x is the dimensionless product of particle radius and wave number. I_0 is the illumination intensity. n is the refractive index of the particle. k and r are the wave number and distance respectively. θ is the scattering angle. The noise cause by this scattering light can also be calculated as:

$$N(\lambda_{480}) = I(x,\theta) Q(\lambda_{480}) T(\lambda_{480}) \tag{3-3}$$

So the signal to noise ratio can be expressed as $SNR = F(\lambda_{520}) / N(\lambda_{480})$. To improve signal to noise ratio for fluorescent light detection, several general rules can be conclude from above analysis. First, fluorophore with high quantum yield is desirable and excitation wavelength should be chosen according to the wavelength dependent extinction coefficient. For FITC dye, the quantum yield is about 0.5 and the extinction coefficient at 488 nm is about 67,000 L/mole·cm [77]. Secondly, appropriate band pass optical filter should be used so that $T(\lambda_{520})$ is much greater than $T(\lambda_{488})$ and most scattering light can be eliminated. For a typical band bass filter with center wavelength at 520 nm and full width at half maximum (FWHM) at 10 nm (20BPF10-520 from Newport Corporation), the transmittance at 520 nm is greater than 50% while it is reduced to under 0.1% at 488 nm. Additionally, consideration of signal to noise ratio also affects the optical detection system layout. The fluorescent detection unit is often positioned so that its optical axis is perpendicular to the incident direction of excitation light. With this arrangement, the scattering light can cause reach the fluorescent detection unit is the one with

scattering angle close to 90^{o}. From Equation (3-2), it is clear that the scattering is at minimum at the right angle.

For larger particles, Mie theory or even diffraction theory [78] should be used for the scattering intensity calculation [78]. Although the exact intensity distribution will be different from Rayleigh scattering, the general rules for achieving high signal to noise ratio remain similar.

In a typical flow cytometer operation, Raman scattering from solution medium can also cause optical related noise. Unlike elastic scattering where scattering light has the same wavelength as the illumination light, Raman scattering is an inelastic process and scattering light has different wavelength than the illumination light. In cytometry operations, Raman scattering comes from the O-H bond in water is the dominant effect, and the frequency of the resulting Raman scattering light is about the sum of the incident light frequency and the vibrational transition from O-H bonds [79]. Because of this, the noise effect of Raman scattering light is highly fluorochrome dependent [80]. For example, with 488 nm excitation light, the emission peak of water Raman scattering is at 585 nm [80]. This will not likely cause problem for FITC dye since its emission peak is far away from the Raman scattering peak. However, this may have significant interference for phycoerythrin (emission peak at 578 nm). Using wider band pass filter to recover more fluorescent light without significant change scattering intensity, since Raman scattering peak is relatively narrow, may increase the signal to noise ratio in this case [80].

3.4 3-D Hydrodynamic Focusing in a Rectangular Microchannel

Udoetok et al. developed a computational fluid dynamics model to analysis the hydrodynamic focusing effect in a focusing chamber similar to this design [81]. In their work, commercial software Fluent (ANSYS Inc., Canonsburg, PA) was used to model the hydro-

focusing process and optimize chamber design. Readers should refer to their work for a complete fluid dynamic analysis of the hydro-focusing chamber. In this section, a simple model was introduced to provide method to analytically estimate the focused sample width at the fully developed region. This simplified model can provide a quick guidance for 3-D hydro-focusing experiment although the result may not be as accurate and complete as that from CFD simulation.

In conventional flow cytometer, the flow channels normally have circular cross-sectional profile and the resulting flow velocity distribution across the channel has a symmetric parabolic profile. In micromachined cytometer, the microchannels usually have a rectangular shape and the velocity distribution is more complicated. In this section, we proposed a simple method developed based on mass conservation and laminar flow condition in microchannel. It can be used to determine the width of the focused sample flow under different sheath conditions and provide a quick reference for future micro cytometer designs. Similar method has been used to analyze 2-D hydrodynamic focusing effect [82], to the best of our knowledge, this model has not been extend to 3-D focusing analysis.

In a microchannel, Reynolds number (*Re*) is usually small and most developed flows are laminar (*Re* < 2300). Under this condition, if we assume that the fluid being analyzed is uncompressible Newtonian fluid and the microchannel size is big enough so that the continuum condition is not violated. The fluid motion is governed by the mass, momentum and energy conservation equations:

Mass conservation:
$$\nabla \cdot \vec{V} = 0 \tag{3-4}$$

Momentum conservation:
$$\rho \frac{d\vec{V}}{dt} = \rho g - \nabla P + \mu \nabla^2 \vec{V} \tag{3-5}$$

Energy conservation:
$$\rho c_v \frac{dT}{dt} = k \nabla^2 T + \phi \tag{3-6}$$

Where is $\bar{V}$ the flow velocity, ρ is the fluid density, P is the pressure, g is the gravitational constant, μ is the dynamic viscosity, T is the temperature, c_v is the heat capacity, k is the thermal conductivity and ϕ is the viscous-dissipation function [83]. In this analysis, only the equation (3-4) and (3-5) will be used to calculate the velocity profile and energy equation (3-6) is not used here.

For the fully developed laminar flow in a microchannel, further simplifications are possible. First, due to the ultra-small volume of fluid in a microchannel, the gravitational force is negligible. Also, the pressure distribution is only a function of x as illustrated in Figure 3-5 (a). Otherwise, the fluid cannot be stable at y or z direction. In addition, flow velocity has only x components and this x component is independent of x because of flow continuity. With all these conditions, equation (3-4) and (3-5) can be combined to a new equation (3-7):

$$-\frac{dP(x)}{dx}+\mu[\frac{\partial^2 u(y,z)}{\partial y^2}+\frac{\partial^2 u(y,z)}{\partial z^2}]=0 \qquad (3\text{-}7)$$

here, $u(y,z)$ is the x component of the fluid velocity.

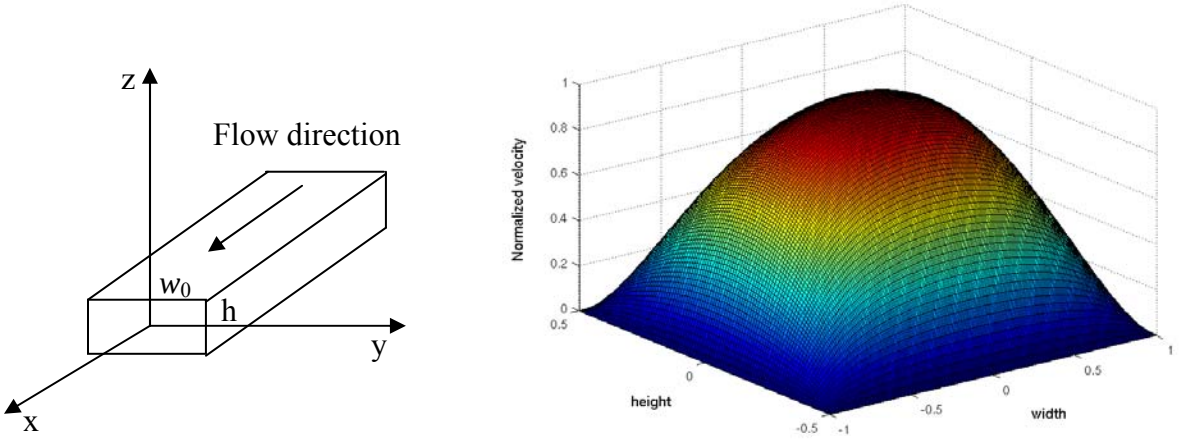

Figure 3-5 Laminar flow in a rectangular microchannel: (a) channel dimensions; (b) flow velocity distribution across the channel

By using non-slipping boundary conditions, analytical solution for equation (3-7) exists for the flow in a rectangular channel. It is the classic Poiseuille velocity profile for a rectangular channel and can be expressed as equation (3-8) [84]:

$$u(y,z)=\frac{4h^2}{\mu\pi^3}(-\frac{dP}{dx})\sum_{n=0}^{\infty}(-1)^n * \{1-\frac{\cosh[(2n+1)\pi y/h]}{\cosh[(2n+1)\pi w_0/(2h)]}\}\frac{\cos[(2n+1)\pi z/h]}{(2n+1)^3} \quad (3\text{-}8)$$

Where h is the channel height, w_0 is the channel width. The calculated velocity distribution is shown in Figure 3-5 (b). If the total flow rate is γ, it then should equal to the surface integration of the velocity distribution over the whole channel cross-section, as shown in equation (3-9):

$$\gamma_t = \int_{-h/2}^{h/2}\int_{-w/2}^{w/2} u(y,z)dydz \quad (3\text{-}9)$$

In the case of 3-D hydrodynamic focusing, a portion of the flow is the sample flow. Ideally, sample flow is focused at the center of the fluid channel. To evaluate the width of the focused sample flow, we assume the focusing in horizontal and vertical directions are equal and the resulting sample flow is focused into a square shape stream. Due to mass conservation, the sample flow rate (γ_a) should equal to the integration of the velocity profile over the sample stream cross-sectional area (equation (3-10)).

$$\gamma_a = \int_{-w_0/2}^{w_0/2}\int_{-w_0/2}^{w_0/2} u(y,z)dydz \quad (3\text{-}10)$$

During experiment, the channel dimensions and flow rates for sheath and sample flow are often known. To obtain the width of the focused sample flow, only the flow rate ratio between the sample flow and sheath flow (γ_t) is necessary.

$$\gamma_a/\gamma_t = \int_{-w_0/2}^{w_0/2}\int_{-w_0/2}^{w_0/2} u(y,z)dydz \Big/ \int_{-h/2}^{h/2}\int_{-w/2}^{w/2} u(y,z)dydz = \int_{-w_0/2}^{w_0/2}\int_{-w_0/2}^{w_0/2} u_n(y,z)dydz \Big/ \int_{-h/2}^{h/2}\int_{-w/2}^{w/2} u_n(y,z)dydz \quad (3\text{-}11)$$

Where $u_n(y,z)$ is the normalized velocity against the maximum velocity at the channel center. Since the only unknown in equation (3-11) is the focused sample width, simple numerical calculation can be carried out to obtain w_0. A typical relationship between flow ratio and focused sample width is illustrated in Figure 3-6. It can be seen that the focused sample stream width

decrease as the flow ratio increase. To focus the sample focus down to one tenth of the channel width, the sheath flow rate needs to be about ten times of the sample flow rate.

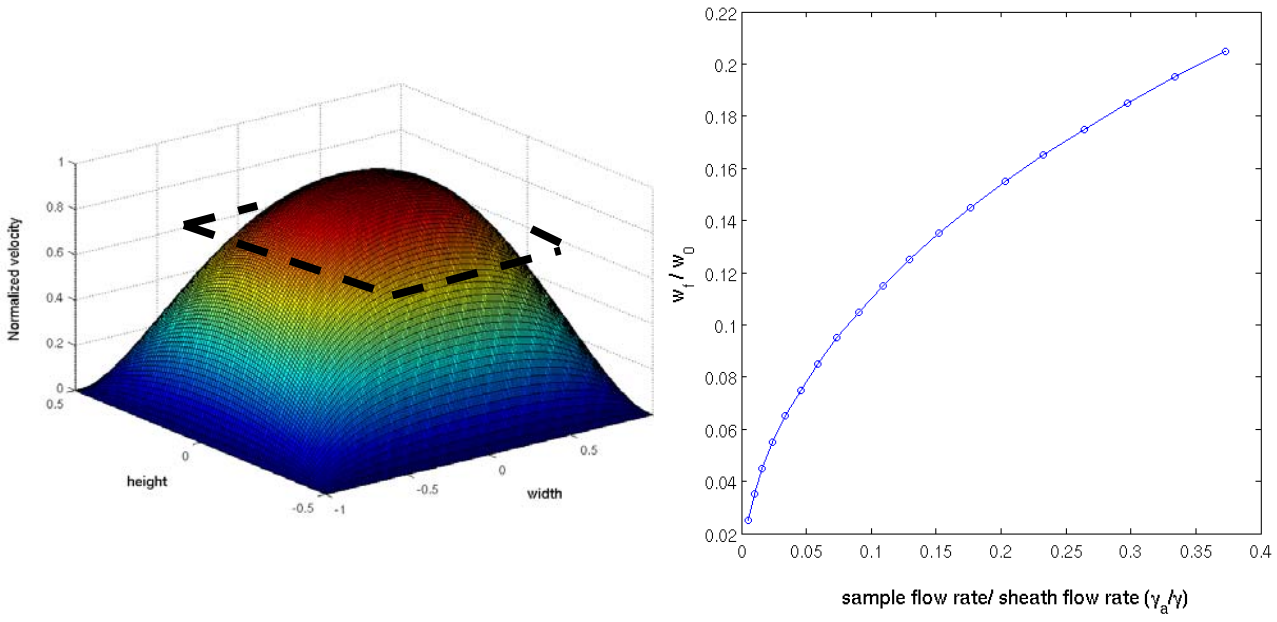

Figure 3-6 (a) sample flow is at the center area confined by the dashed square; (b) focused sample stream width versus flow ratio

Since the previous analysis focused on the fully developed flow, it is worthwhile to estimate the entrance length of the microfluidic channel. For microchannel flow with medium Reynolds number, the correlation between the entrance length and the Reynolds number is similar to that in a conventional flow [85, 86].

$$L_e / D_h = 0.0752\,\mathrm{Re} \tag{3-12}$$

Where $\mathrm{Re} = \rho V D_h / \mu$, D_h is the hydraulic diameter and L_e is the entrance length.

For the water flow in a channel of 100 μm height and 200 μm width, if the flow rate is 300 μl/min, the corresponding Re is about 33.3. So the entrance length is about 2.5 times of the

channel hydraulic diameter (D_h = 133 μm). It is safe to conclude that the flow in the outlet channel can develop relatively fast and fully developed flow can be expected at the downstream investigation area.

3.5 Device Microfabrication

Out-of-plane microlens is an essential component in the proposed micro flow cytometer. It was fabricated using tilted UV lithography technique. Fabrication process is similar to the process described in the previous chapter. Briefly, two 45^o UV exposures were performed on a thick layer of SU-8 (>500μm). Two exposed SU-8 cylinders perpendicular to each other were formed after two exposures; at the intersection area, a four-faced shape region was double exposed; during the development process, the sharp edges of the double exposed region were smoothed out and nearly spherical shape out-of-plane microlens was formed in the double exposed region.

The micro flow cytometer fabrication process is illustrated in Figure 3-7 (a-d):

First, SU-8 50 was spin-coated on a clean and dehydrated silicon wafer at a spin speed of 450rpm to obtain a 500μm thick layer. After being softbaked at 110^{o}C for 6 hours, the sample was fixed against a chromium mask in a rotatable home-made chuck. A 30^o tilted UV lithography was performed to expose those 30^o slopes and the bottom of the outlet channel (Figure 3-7 (a)). The sample was then postbake at 90^{o}C for 30 minute.

Next, a second 500μm thick SU-8 layer was spincoated on the sample to make the total thickness to 1000μm. Following an 11 hour softbake, two 45^o tilted exposures at opposite direction were performed using a second mask to form the injection nozzle at the center as shown in Figure 3-7 (b).

Thirdly, another two 45^{o} exposures was done using a third mask with pre-aligned microlens and optical fiber holder patterns. Microlens and fiber holder were defined in this step (Figure 3-7 (c)). To achieve better top-to-bottom exposure uniformity, a PMMA (Plexiglas® G) sheet was used as a UV filter to eliminate UV light with wavelength under 400nm; In this step, it should also be noticed that the exposure dosage for microlens array was different from that for the fiber holder structures. Since both lens and fiber holder patterns were on the same mask, a shadow mask was needed to cover the lens pattern while exposing the fiber holder.

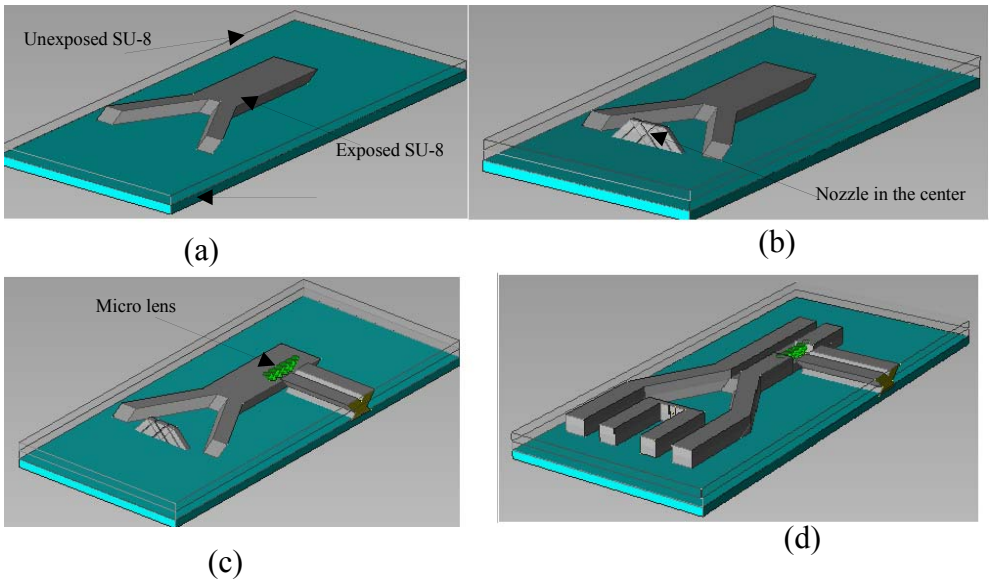

Figure 3-7 Micro flow cytometer fabrication process

Fourthly, fluidic channels were defined with another mask and normal UV exposure. This step was done on a Quintel UV aligner to ensure the good alignment between fluidic channels and optical components. The microstructures were all visible after postbake (Figure 3-7 (d)).

Finally, the whole sample was immersed into SU-8 developer up-side-down for about 50 minute to clear the large unexposed area and then switched into fresh SU-8 developer face-up for 1 hour to complete the development.

For micro fluidic channel sealing, a piece of 1mm thick glass slide with a thin layer of SU-8 as adhesive was used to cover the device to form a sealed chip. Output optical fiber was manually inserted into the V-shape fiber holder groove which was pre-aligned to one of the microlens pixel.

3.6 Results and Discussions

3.6.1 Microfabrication Results

The proposed MEMS flow cytometer with out-of-plane microlens was successfully fabricated with tilted UV lithography technique. Figure 3-8 shows SEM images of some key features on the chip. Figure 3-8 (a) shows three 30^o slopes for vertical hydro-focusing; a

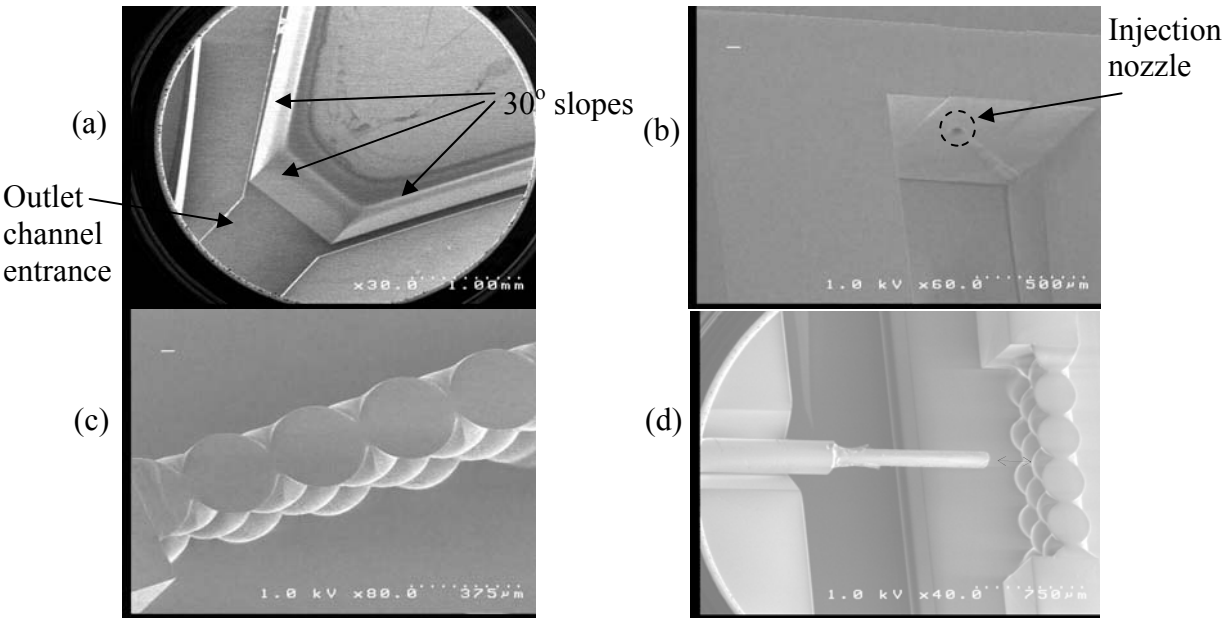

Figure 3-8 SEM pictures of the key structures on the fabricated micro flow cytometer

diamond-shaped 100μm x 100μm sample injection nozzle is shown in Figure 3-8 (b); a fabricated out-of-plane microlens array with pixel diameter of 350μm can be seen in Figure 3-8

(c), microlens pixels have smooth spherical shape without obvious sharp edges; Figure 3-8 (d) shows the same microlens array with a multi-mode optical fiber (200μm in diameter) fixed in the V-shape fiber holder groove. From the picture, it can be seen that optical fiber is well aligned with one of the microlens pixel.

In our design, microlens is used for light collection purpose, so aberration can be tolerated to a certain degree. However, focal length is still an important parameter. The focal length of the microlens is mainly determined by the mask design. Elliptical transparent patterns on the mask with different major axis to minor axis ratios can result in microlenses with different focal lengths. Besides the mask design, exposure dosage and development condition also affect radii of curvature of the resulting microlens. Lower exposure dosage and longer development time generally produce more flat lens surfaces, thus longer focal length. More experiments and analysis need to be done in the future to quantitatively study the relationship between process conditions and the resulting microlens optical properties.

3.6.2 Cell Counting Experiment Results

One basic function for a flow cytometer is cell counting. Preliminary experiment has been conducted to use the fabricated micro flow cytometer to count micro-sized fluorescent beads. Micro beads with allophycocyanine (APC) dye (Bangs Lab Inc. Fisher, IN) were used in the experiment. These micro beads were chosen because they have size similar to human lymphocytes, which is 7-9μm in diameter. The experimental setup is schematically shown in Figure 3-9. Sheath flows (deionized water) were injected by a syringe pump at a flow rate of213μL/min each, and the sample flow was at 10μL/min. A 50mW laser diode with wavelength of 645nm was used as the external excitation light source. The laser beam was focused by a microscope objective onto the flow cytometer chip mounted on an adjustable stage. The emitted

fluorescent light was focused by the microlens and then picked up by the output optical fiber. At the other end of the optical fiber, a customized APD (avalanche photodiode) photon detection unit was used for fluorescent light detection with high precision and sensitivity. To reduce the noise caused by the scattering light from the channel walls and fluid medium, a band-pass (680nm-720nm) optical filter was placed between the output fiber and the APD detection window.

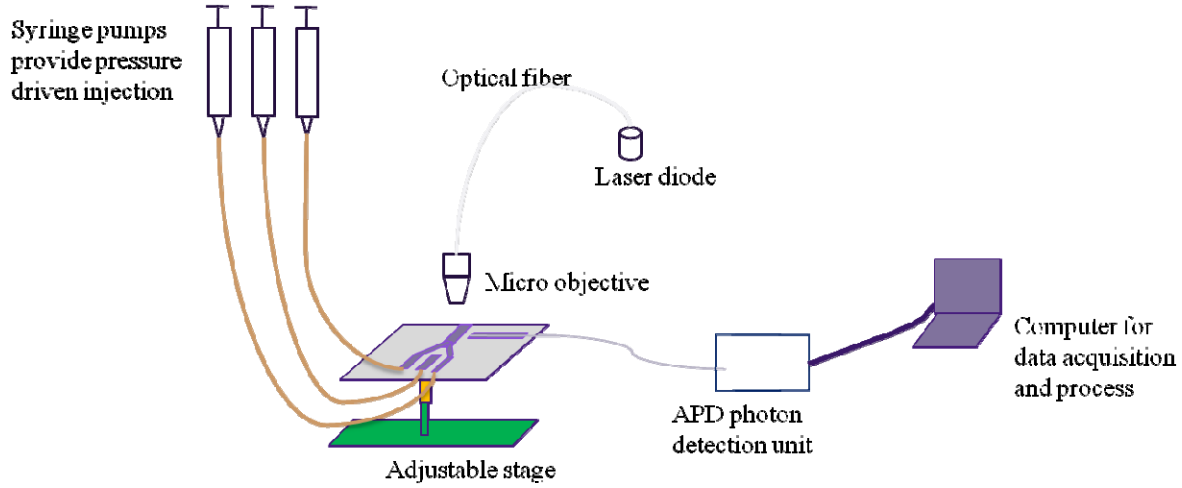

Figure 3-9 Schematic diagram of the cell counting experiment setup

During the experiment, we first adjusted the position of the micro flow cytometer to ensure excitation laser beam was focused to a small spot at the center of the fluidic outlet channel; then the sheath flows were turned on at the set flow rate to fill the fluidic channels and wash away residue fluid; sample bead product was pre-diluted in a 1 to 4 ratio to reduce beads aggregation and then injected into the flow cytometer chip after the sheath flows were stabilized; output signal was displayed and recorded by the software for the APD photon detection unit; when a sample bead passing through the detection area, a burst or peak output signal was generated. By counting the number of peaks within a certain amount of time, micro beads or

cells in the sample fluid was counted.

Figure 3-10 shows a typical cell counting result from the experiment. Sample flow injection was started at about 2 second and lasted for about 20 seconds. From the result, it can be seen that the flow cytometer chip can generate clear signal with high signal to noise ratio. However, the number of generated peaks is lower than the expected beads number in the sample and some peaks with lower intensity were observed. One possible reason is that the hydro-focusing was not ideal, some sample beads actually passed through the detection area at an off-center position, which greatly affect the output optical signal intensity as pointed out in the optical analysis section. Hydro-focusing in the horizontal plane has been investigated using a fluorescent microscope. Instead of sample beads, fluorescent dye was used in the experiment for

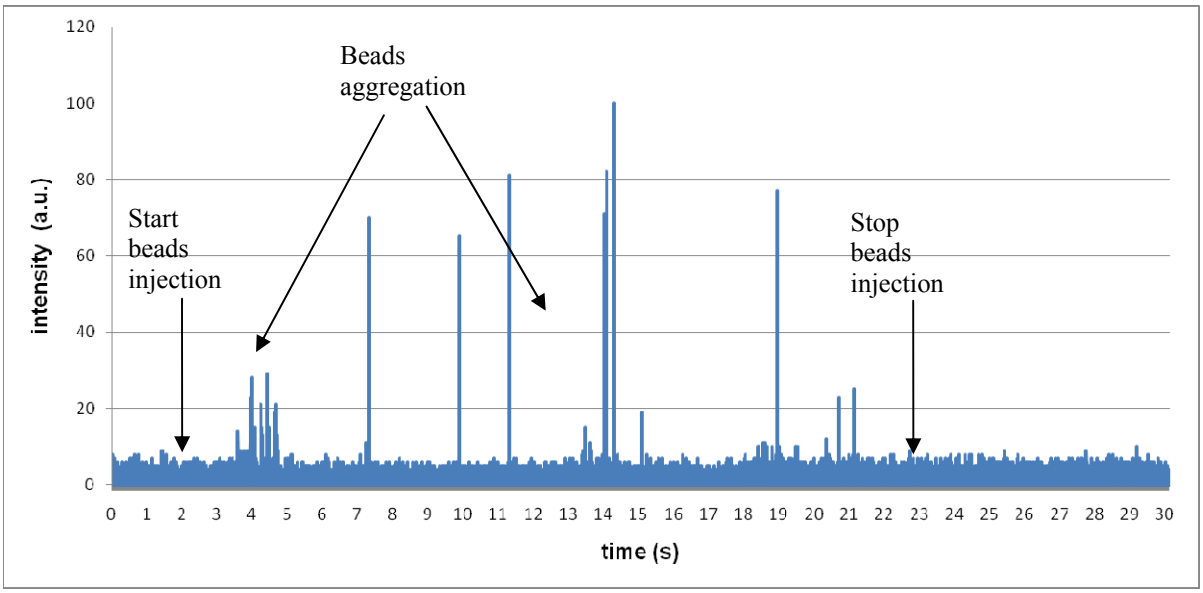

Figure 3-10 Signal response for the cell counting experiment.

the ease of observation. Figure 3-11 is a snap shot from the hydro-focusing experiment result. Fluorescent dye was well focused by the sheath flows into a stream about 50μm in width.

Although higher sheath flow rate could generate narrower focusing, the focused stream was not stable and fluctuation was observed. Since 50 μm was wider than the bead diameter we used (7-9μm), signal fluctuations might be caused.

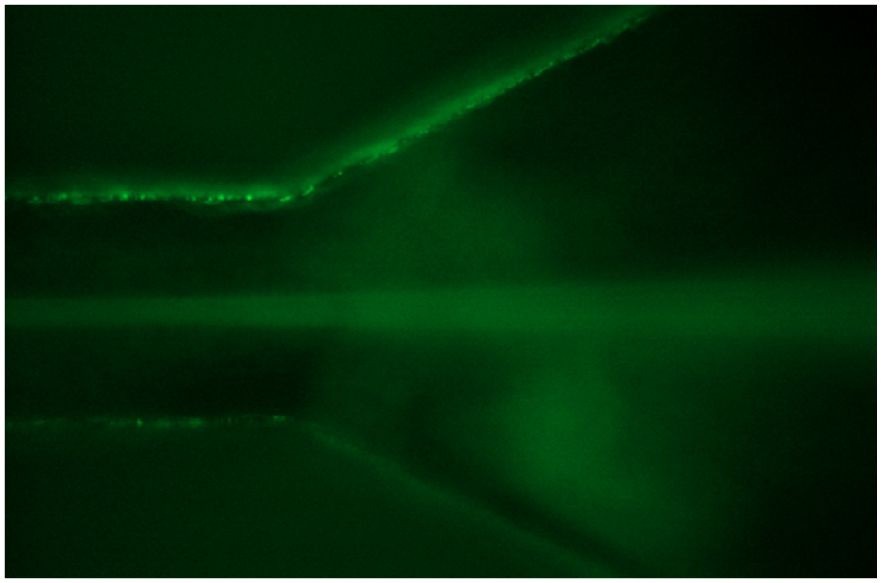

Figure 3-11 Fluorescent dye focused by sheath flows.

3.7 Hydrofocusing Chamber Optimization

Based on previous experimental results, the minimum width of the focused sample flow was about 50 μm, which is much higher than the cell/beads size used in the beads counting experiment (bead size ≈ 7.5 μm). Ideally, the focused sheath flow need to be at least less than the twice of the sample size. In this particular case, the focused sample stream width should be narrowed down to less than 15 μm. Also, due to the optical analysis results, the focused stream should be as narrow as possible to minimize the optical signal fluctuation caused by the misplacement of the sample cell/bead. In addition, hydrofocusing in the vertical direction was only performed at one side in the previous design and this may cause offset in the vertical direction.

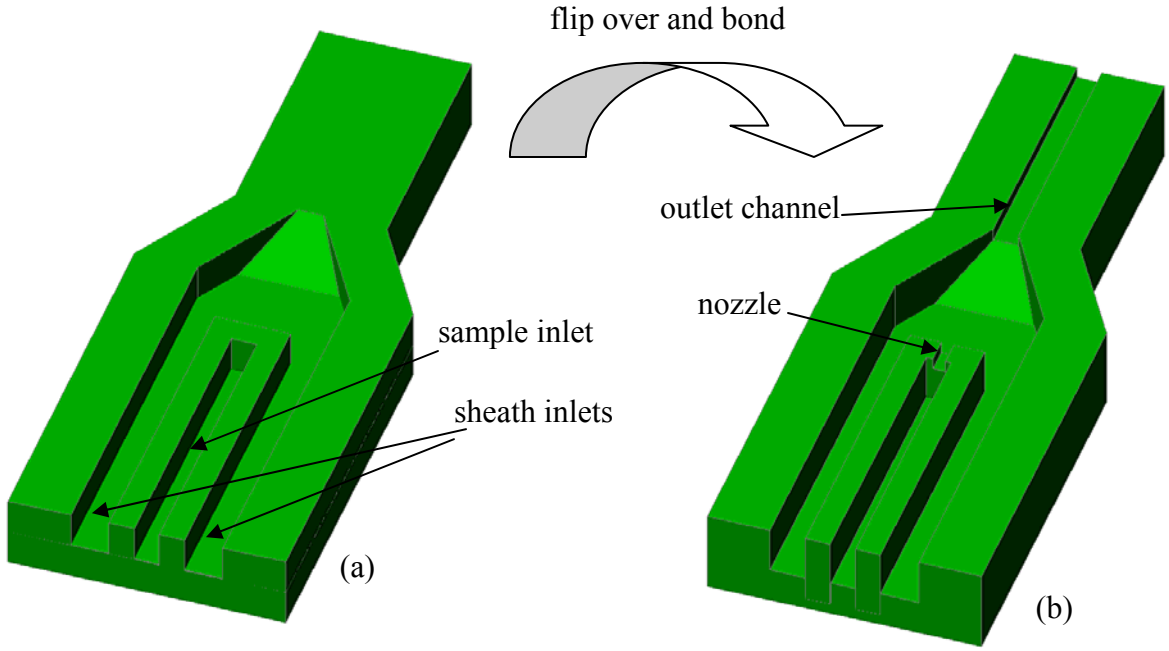

Figure 3-12 Schematic of the new hydrofocusing chamber design: (a) top half, (b) bottom half.

To optimize the hydrofocusing chamber, the new design includes two 30^{o} slopes symmetric to each other to provide vertical focusing from both the bottom and the top. The dimensions of the chamber design are also optimized based on the simulation results. The newly designed chamber is illustrated in Figure 3-12. To better describe the new design, the chamber is separated in two halves (the bottom half and the top half). Sample nozzle and the outlet channel are fabricated on the bottom half, which makes the assembly process more tolerant for misalignment. The nozzle size in the new design is 100 μm x 100 μm and the outlet channel is 200 μm x 100 μm.

3.7.1 Fabrication Optimization

Previously, the device was fabricated on a silicon substrate and a glass slide was used as the transparent top cover for the ease of observation. However, to make the true 3-D focusing chamber which requires the top half to be flipped over and aligned onto the bottom half, both

halves have to be transparent for alignment and later observation. Obviously, silicon substrate cannot be used to fabricate the newly designed chamber due to its opacity. The attempt to try to fabricate the device on a glass substrate also failed due to the poor adhesion between glass surface and SU-8.

Figure 3-13 Required SU-8 negative mold

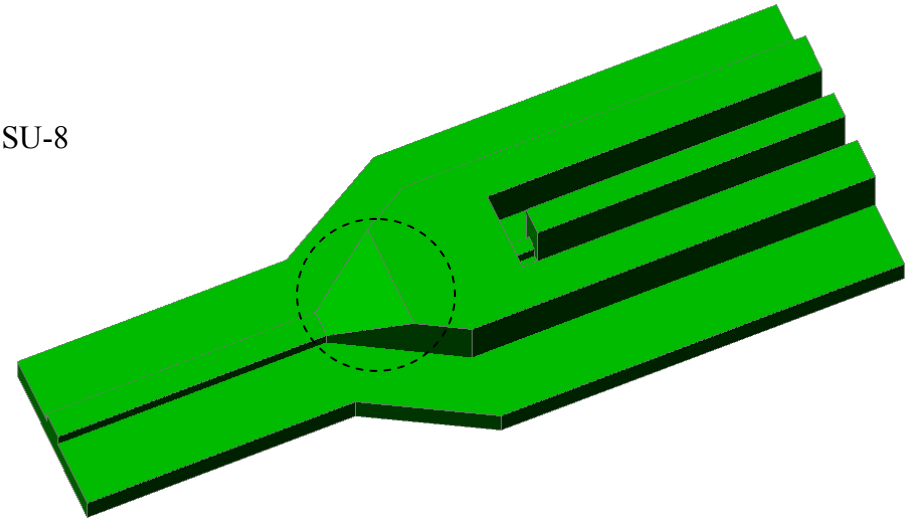

PDMS molding, as a capable technique to replicate three-dimensional microstructures, was finally chosen to make transparent components for the newly designed focusing chamber. To make the PDMS chamber halves as illustrated in Figure 3-12, SU-8 mold needs to be made as shown in Figure 3-13. However, the shown negative mold structure cannot possibly be made using the existing tilting lithography technique. The difficulty lies at the area highlighted by the dashed circle in Figure 3-13, which is a 30^{o} slope wall with wide top and narrow bottom. Since exposure light beam is always delivered from top to bottom and SU-8 is a negative-tone photo resist, the resulting slopes need to have same width from top to bottom. An extra normal exposure can partially cover the slope and make a slope with uneven top and bottom as shown in Figure 3-13. It is nearly impossible to make a protuberant slope with narrower bottom.

Due to the difficulties associated with negative SU-8 mold fabrication, positive SU-8 molds with structures same as the final structures (Figure 3-12) were fabricated. The fabrication

of SU-8 molds is very similar to the one described in section Figure 3-7. However, only one tilted lithography process is involved in the fabrication of new mold. Comparing to the five tilting exposures included in the old process, this new process is much easier and time efficient.

A PDMS double casting process was eventually developed to reproduce the all-transparent PDMS replicas with structures same as the one on the SU-8 molds. PDMS to PDMS double casting has been previously investigated by researchers to replicate microstructures mainly with low aspect ratio [87, 88]. Sun and co-workers used trimethylchlorosilane (TMCS) to treat a negative PDMS mold obtained by casting from natural lotus leaf and got artificial lotus leaf with super hydrophobicity by casting PDMS using the treated PDMS mold [87]. Gitlin et al. reported a method to use a safer chemical hydroxypropylmethylcellulose (HPMC) as the non-texture releasing agent for the PDMS on PDMS casting [88]. During our experiment, HPMC treatment was enough to successfully release our double-casted structure from negative PDMS mold, it may due to the fact that our microstructures are much taller than the one reported in Gitlin's work and it is more difficult to release. By exposing PDMS mold in TMCS vapor environment for 30 min did not result in a good enough non-sticking layer for subsequent process.

The mold treatment process used in our experiment is illustrated in Figure 3-14. The PDMS negative mold was first treated in oxygen plasma for 1 minute (150 mTorr oxygen, 50 Watt). The resulting mold was then quickly moved into a silanization chamber and exposed in 1H, 1H, 2H, 2H-perfluorodecyltrichlorosilane (PFDTS, $C_{10}H_4Cl_3F_{17}Si$) vapor environment for 25 minutes. Oxygen plasma treatment process generated abundant of silanol groups on the PDMS surface[89], the PFDTS vapor then reacted with silanol group to form a layer of organosilane and the organosilane molecular also formed network among each other, the

combined result was a robust organosilane film with fluorine sticking out. After baking at 70 ^{o}C for 1 hour, the PDMS mold treatment was finished and the resulting mold can be used as a ordinary mold for following PDMS casting process, no sticking between PDMS replica and PDMS mold was observed. As a matter of fact, microstructure with aspect ratio as high as 10:1

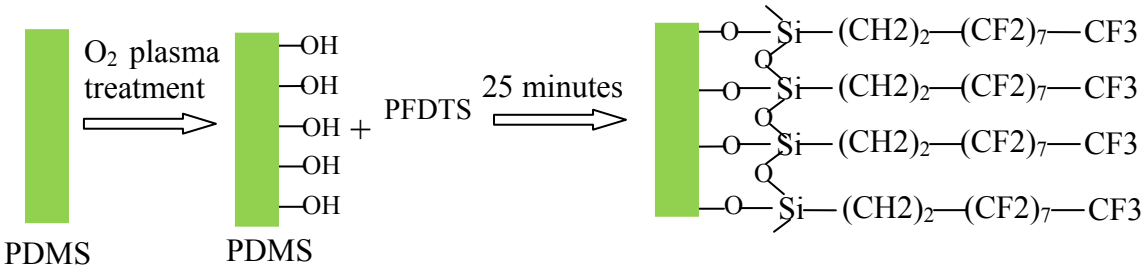

Figure 3-14 PDMS negative mold treatment for double casting process

was successfully replicated using this process.

Once the top and bottom halves of the hydrofocusing chamber were fabricated in PDMS, they were treated briefly in oxygen plasma and aligned onto each other under a microscope. Small Tygon tubings (0.03" OD × 0.01" ID; Small Parts Inc., Miami Lakes, FL) were inserted into fluid access holes for the interconnection with fluid supply and collection systems.

3.7.2 Experimental Results with the New Hydrofocusing Chamber

Hydrofocusing experiment was performed using the newly designed and fabricated device with true 3D hydrofocusing ability. Bright field and fluorescent images were taken using a Leica DM RXA2 upright fluorescent microscope (Leica Microsystems, Ban-nockburn, IL). A bright field image of the fabricated device (only showed the critical components include nozzle and 30^{o} slopes) is shown in Figure 3-15 (a). With fluorescein dye injected through the sample nozzle and phosphate buffer solution sheath flows from both sides, sample flow first slightly diverges right after entering the focusing chamber and then focused by the sheath flows to form a

narrow stream. This result is in good agreement with the simulation result obtained by Udoetok [81].

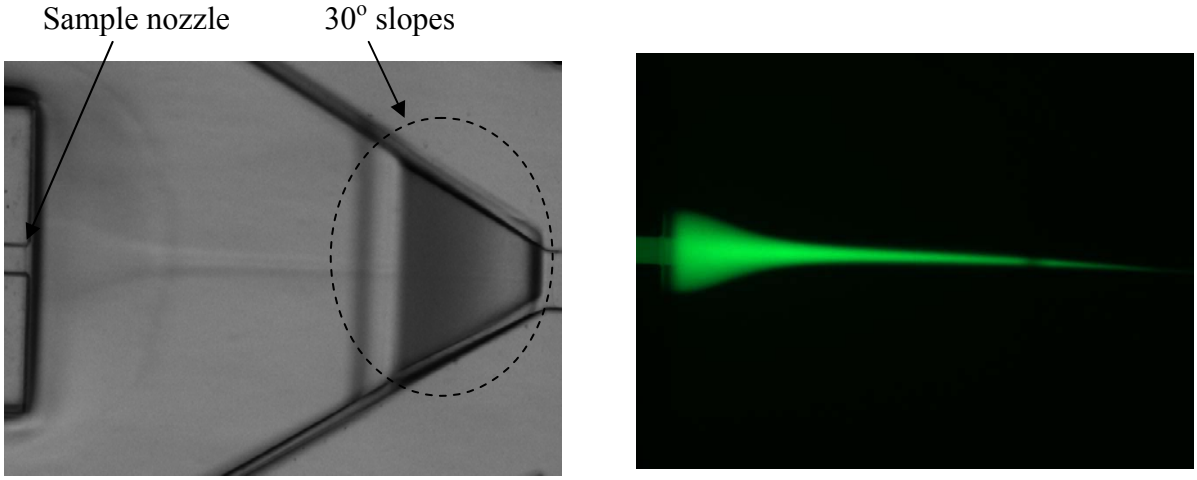

Figure 3-15 (a) bright field image of the 3D hydrofocusing chamber; (b) fluorescent dye stream focused by sheath flows (fluorescent image taken at the same location on the same chip)

To investigate the hydrofocusing ability of this chamber, sample to sheath flow rate ratio was controlled to change the width of the focused sample stream. Figure 3-16 shows the focused sample streams under different sheath flow rates (sample flow rate fixed at 5 μl/min). It can be seen that the width of the stream decrease with the increase of sheath flow. At low sheath flow rate, the hydrodynamic force on the sample stream is not sufficient and the sample stream is poorly focused (Figure 3-16 (b)). Once the sheath flow rate reaches 150 μl/min, the sample stream is focused down to about 10 μm in diameter, which is suitable for our flow cytometer application. In this setup, the sample to volume flow rate ratio equals to 0.02 and the focused sample streams width is about 1/20. This result is very close to the sample width prediction curve illustrated in Figure 3-6 (b). Because of mass conservation, it can be predicted that the height of the focused sample stream is also close to the results from the previous analysis in section 3.4.

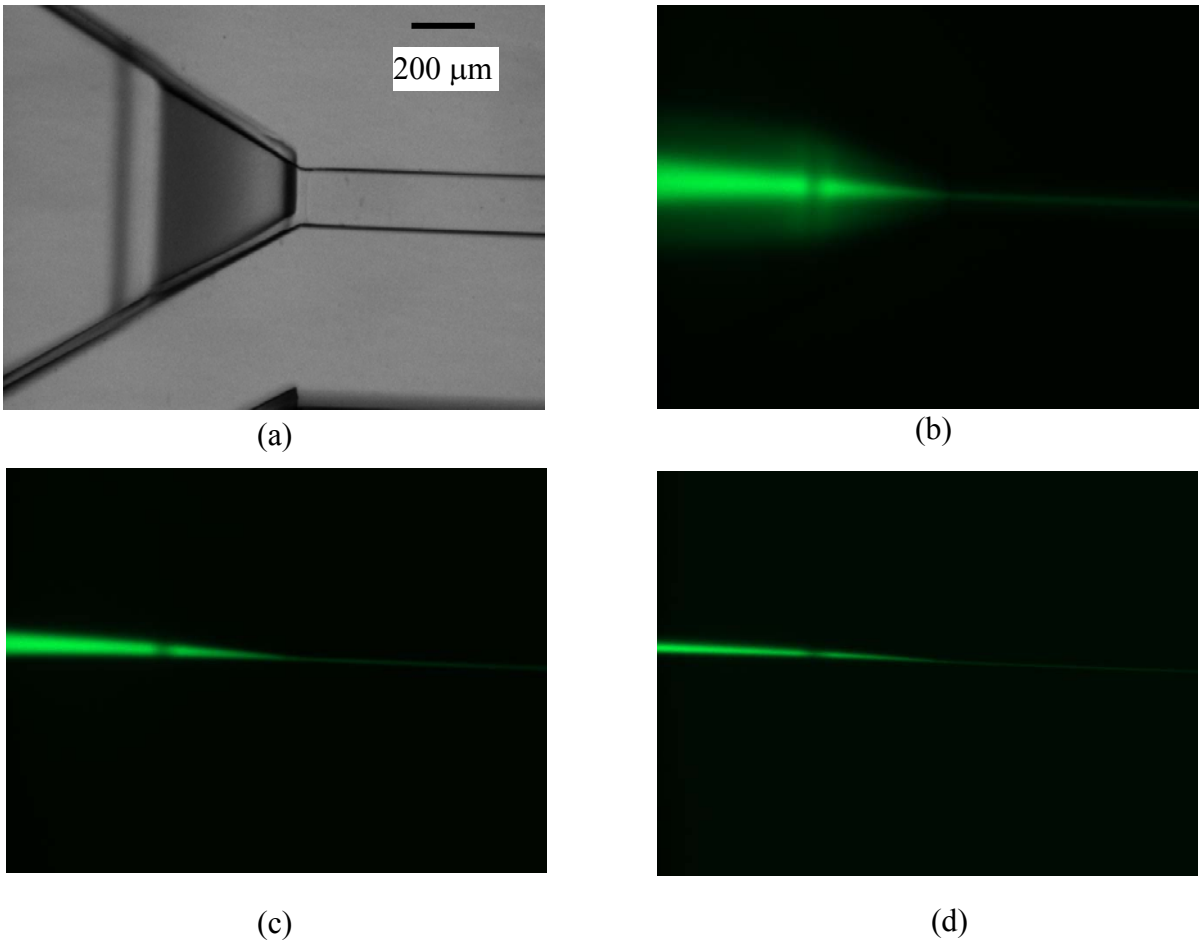

Figure 3-16 Hydrofocusing with at different sample to sheath flow rate ratio: (a) bright field image; (b)-(d) sample flow at 5 μl/min, sheath flow at 30 μl/min, 80 μl/min and 150 μl/min respectively.

3.8 Conclusions and Future Work

We have successfully fabricated and tested a micro flow cytometer with a three-dimensional hydro-focusing unit and an on-chip optical detection unit including an out-of-plane microlens array. The pre-aligned, out-of-plane, microlens was fabricated using a lithography-based technology. The resulting microlens was embedded in one of sidewalls of the fluidic outlet channel. Optical analysis was conducted using Zemax to optimize the design parameters and to estimate the light coupling efficiency. According to the simulation results, the out-of-plane microlens in the reported design can substantially increase the light coupling efficiency, and also

makes the detection system more sensitive to sample cell mis-focusing caused by non-ideal hydro-focusing unit. Cell counting experiment was also conducted to test the prototype system. Preliminary results obtained have confirmed feasibility of the reported flow cytometer in simple cell counting application.

An optimized hydrofocusing chamber with true 3-D focusing ability was also developed. Experimental results show that the new design is capable of focusing the sample stream down to a width very close to the diameter of our target cell/beads. And the focused sample stream is more stable comparing to that in the early design.

Udoetek et al.[81] optimized the hydrofocusing chamber design based on computational fluid dynamics (CFD) simulation results. Although the resulting chamber is still difficult to fabricate due to its three-dimensional design, more work can be done to look for a new technology for the optimized chamber fabrication.

With the success of developing all-PDMS hydrofocusing chamber and PDMS membrane based out-of-plane microlens, future work can be focused on the integration of PDMS membrane based out-of-plane microlens into the new hydrofocusing chamber. With the new lens fabrication procedure, the focal length of the microlens can be precisely defined by controlling the pneumatic pressure used for membrane deformation. In addition, since the microlens fabrication process is essentially soft lithography process plus pneumatic lens formation, the fabrication process should be much more efficient.

CHAPTER 4. A PDMS BASED MICROCHIP PLATFORM FOR HIGH THROUGHPUT IMMUNOASSAY APPLICATIONS

4.1 Introduction

Immunoassay is a biochemistry analytical tool that utilizes the antigen-antibody specific binding reaction to measure the concentration of the target chemical substance in the sample solution. After being first invented by Solomon Berson and Rosalyn Yalow in late 1950s [90], immunoassay has not only been widely used in clinical applications [91], but has also found applications in drug testing [92], environmental monitoring [93], food safety study [94] and even the detection of explosives [95, 96]. Immunoassay can be categorized into heterogeneous assay and homogeneous assay. In a typical heterogeneous assay, the coating antibody (or primary antibody) is first immobilized on the solid phase substrate (it is sometimes called solid phase immunoassay). After washing step to remove non-immobilized antibody and blocking step to cover the vacant binding sites on the solid phase substrate, sample solution is introduced onto the antibody-coated substrate. The coated antibody can capture its target antigen if it does exist in the sample solution. After second washing step, reporter antibody (or secondary antibody) with enzyme or other detectable labels is then introduced into the system. The previously captured antigen can then capture the reporter antibody to form a sandwich antigen-antibody complex. By detecting the reporter antibody, information about the existence and concentration of the antigen is obtained. The working principle of a homogeneous immunoassay is very similar to the heterogeneous assay, however, all the reactions take place in solution phase and the free antibodies are not required to be separated from the antigen-antibody complex. Therefore, no washing steps are needed [97].

Despite of its wide applications, several drawbacks can be found in conventional immunoassay process. First, the assay time is usually over 24 hours, although it may be shorten by using primary antibody coated substrates; secondly, bulk instruments are necessary to measure the resulting signals; thirdly, trained personnel is often required to conduct immunoassay process to obtain consistent and reliable results. Comparing to conventional assay approach, the microchip-based approach has several important advantages. Less expensive reagents are consumed due to the micro size nature of the fluidic channels. In addition, because of the high surface-volume ratio and short diffusion distance, microchip based immunoassay often requires much shorter assay time. More excitingly, different detection elements can be integrated onto the microchip and on-chip detection is achievable. With the development of microfabrication and immune-sensing technologies, all automated portable immunoassay detection system may be developed in the foreseeable future. Extensive research effort has been devoted to develop microchip-based immunoassays [25, 98-101]. Most of the reported microchip based immunoassay are heterogeneous assays and are often fabricated on polymers (PDMS is the most popular one).

In the development of microchip based multiplex immunoassay, or lab-on-a-chip devices in general, one critical challenge is the in-channel fluid manipulation. The emergence of integrated pneumatic valve has offered a versatile and straightforward solution to address this problem [27, 102]. Individual valves can direct the reagent flow in microchannel network by selectively blocking certain fluid passages; a series of valves close and open at a synchronized fashion can form an effective peristaltic pump; and several peristaltic pumps being operated in a circle function as an active mixer [103]. In fact, microchips integrated with pneumatic valve network have been reported in the fields of genetic analysis [104], amino acid investigation [105], protein

crystallization [106] and single cell studies [107], etc., indicating their great potential to the development of future on-chip automatic analysis systems. Kong and co-workers [108] recently demonstrated such a design for the rapid detection of clenbuterol. Enzyme-linked immunosorbent assay (ELISA) was performed in the interrogation section of the micro channel network and pneumatic valves were utilized to control the introductions of different reagents. The pneumatic valve design they used was similar to the one reported by Grover et al. [102] which was the normally-closed approach (valve is closed in non-activated state and vacuum is applied to open the valve). The normally-open valve (valve is open in non-activated state and air pressure is applied to close the valve) invented by Dr. Quake's group [27] has several advantages over the normally-closed approach. For example, valves are easier to be integrated onto existing microfluidic networks with little or no modification to the fluidic network. The actual valve footprint is smaller than that of the normally-closed valve so that higher valve density on a chip can be achieved. Also, its compatibility with multiple layer process allows large scale integration in a three dimensional fashion for various applications [109]. Although normally open valve – based microfluidic chip platform has been used widely [104-107], the combination of immunoassay with such a microfluidic platform has not been explored much. There are certain advantages to perform immunoassay within this type of microfluidic device: (i) the introduction and delivery of small amounts of analytes are highly controllable and enable the rapid exchange of nanoliter-level solutions on the same chip; (ii) integration of high density of immune-reaction site can be easily achieved for performing high throughput multiplex immunoassays; (iii) because PDMS is transparent, optical detection, e.g. fluorescence, can be performed on the microfluidic device; (iv) Such a microfluidic device can be easily integrated with sensor chip to achieve multiplex electrochemical immunoassays.

In this chapter, the development of a PDMS based microchip platform with integrated pneumatic valve network for immunoassay applications is discussed. The micro fluidic network is formed by four parallel channels and one intersecting channel perpendicular to the previous four. Pneumatic valves are used to control the reagent flow so that immuno-reactions can only happen at each of the four channel intersection areas. These intersection areas are called designated reaction zones (DRZ) though out the chapter. To test and evaluate the fabricated microchip, mouse serum containing mouse IgG was used as the model analyte and Fluorescein isothiocyanate (FITC) labeled goat anti-mouse IgG was selected as the reporter antibody. Experimental results showed that immunoassay based on this microchip platform is simple, sensitive, and may possess great promise for point of care detection of disease protein biomarkers.

4.2 Microchip Design and Working Principle

As a key component in our microfluidic chip, the pneumatic valve is similar to the one proposed by Quake's group [27] and its working principle is illustrated in Figure 4-1. The fluidic

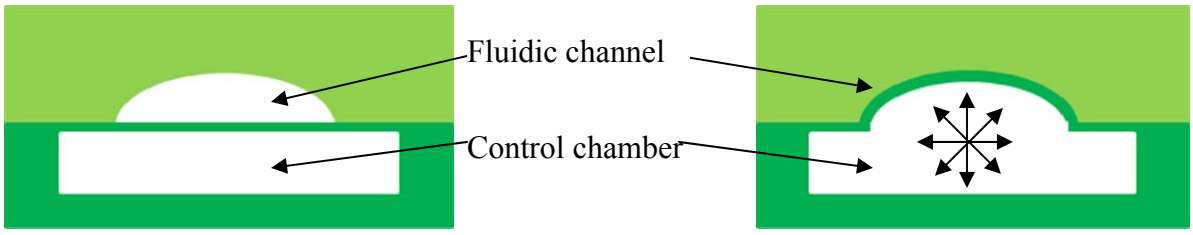

Figure 4-1 Micro pneumatic valve (a) Open; (b) Closed

channel and the pneumatic control chamber are separated by an elastomeric membrane. Without pneumatic pressure, the fluidic channel is unblocked and fluid can go through the channel freely (Figure 4-1 (a)). However, once the control chamber is pressurized, the membrane can deform

and close the fluidic channel. The fluidic channel is designed to have a rounded cross-sectional profile to ensure good sealing and lower the activation pressure [27].

The overall design of our microchip was inspired by Bernard et. al.'s micromosaic immunoassay [99]. In their work, a silicon chip with a group of straight micro fluidic channels was placed against a PDMS slab. Reagents were introduced into the fluidic channels by capillary force. Washing and blocking steps were all performed with the PDMS slab separated from the silicon chip. In our proposed design, all the antibody immobilization, washing, blocking and immuno-reactions take place in the microchannels inside a sealed PDMS microchip with controllable on-chip pneumatic micro valves.

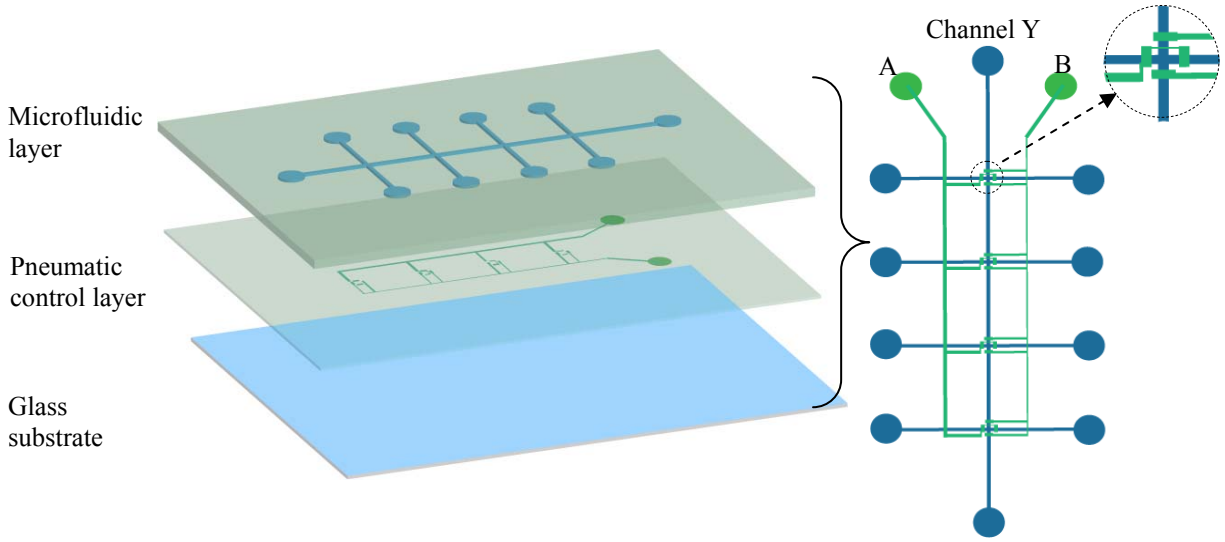

Figure 4-2 Overview of the chip layout: 3-D layout (left) and top view (right)

The microchip in our design includes three layers, a fluidic layer, a pneumatic control layer and a glass substrate (from top to bottom). As illustrated in Figure 4-2, the microfluidic network includes four parallel transverse channels and one longitudinal channel which intersects four transverse channels. Micro valves in the control layer are separated into two groups. Group A is responsible for the flow control in transverse channels and group B is used to block flow in

the longitudinal channel. Each of the four intersections between transverse channels and the longitudinal channel is surrounded by two group A valves and two group B valves. By controlling the status of each valve group, the reagent flow can flow through either in the transverse channel or the longitudinal channel, and the intersection areas are the only sites shared by the transverse channel and the longitudinal channel. As mentioned previously, the immuno-reactions happen only in those intersection areas and those are called designated reaction zones (DRZ). In this first generation design, four DRZs are included in one microchip.

4.3 Device Fabrication

4.3.1 Fluidic Channel Layer Fabrication

To achieve curved channel profile, positive photoresist SPR 220-7.0 was chosen for the process. The fabrication process is a standard UV lithography process with a reflow step at the end, and can be explained as following:

(a) A clean 4 inch silicon wafer was dehydrated at on an 180^{o}C hotplate for 1 hr and treated in hexamethyldisilazane (HMDS) vapor for 3 mins.

(b) SPR220-7.0 positive resist was spin coated onto the wafer at 1900 rpm for 30s to obtain an 11 μm layer.

(c) The wafer was then baked at 100^{o}C for 200s to evaporate the solvent.

(d) The soft baked wafer was then exposed under a UV aligner for 200s (UV intensity was not measured for this aligner, optimal dosage found after dosage matrix experiments). A laser printed high resolution transparent film was used as the exposure mask.

(e) After relaxing and rehydration for 20min, the exposed wafer was developed in MF 322 developer for 90s and rinsed in DI water.

(f) The obtained micro fluidic channel pattern was then baked at 140°C for 4min to reflow the resist and form rounded channel profile.

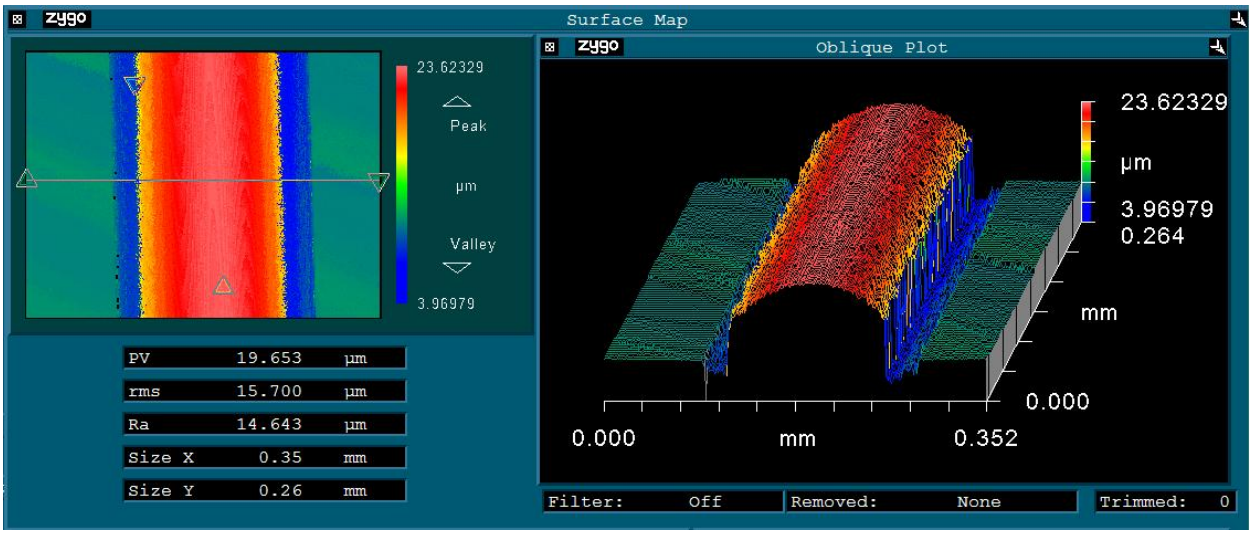

Figure 4-3 Fluidic channel with rounded cross-sectional profile

(g) To obtain a sustainable master mold, the wafer was also baked at 180°C for 30min. The photoresist turned from red to black in color and became insolvable in common organic solvent (IPA, acetone, methanol, etc.).

The resulting wafer with microfluidic pattern was ready for PDMS soft lithography process.

4.3.2 Micro Valve Control Layer Fabrication

SU-8 negative tone photoresist was chosen for control layer fabrication due to its process stability and mechanical toughness of the resulting structures. The fabrication process is as following:

(a) A clean 4 inch silicon wafer was dehydrated at on an 180°C hotplate for 1 hr and treated in hexamethyldisilazane (HMDS) vapor for 3 mins.

(b) SU8-25 negative photoresist was spin coated onto the wafer at 1800rpm for 30s to

obtain a 30μm layer.

(c) The wafer was then baked at 65°C for 5min and 100°C for 8min to evaporate the solvent.

(d) The soft baked wafer was then exposed under a UV aligner for 300s (UV intensity was not measured for this aligner, optimal dosage found after dosage matrix experiments). A laser printed high resolution transparent film was used as the exposure mask.

(e) After post baking at 65°C for 1min and 100°C for 3min, the sample was developed in SU-8 developer and rinsed with IPA.

(f) To obtain a sustainable master mold, the wafer was hard baked at 150°C for 30min.

All fabricated master molds were treatment in HMDS vapor for at least 2hrs before the PDMS soft lithography process. This step was applied to chemically dehydrate the mold surface and consume all the available silanol groups.

4.3.3 PDMS Soft Lithography and Device Assembly

Sylgard 184 (Dow Corning Corporation, Midland, MI) PDMS kit was used for soft lithography process. PDMS prepolymer mixture was prepare at a ratio of 5:1 (base : curing agent) for control layer molding. After treating the mixture in a vacuum desiccator for 30min to remove all trapped air bubbles, the mixture was spin coated onto the control layer master mold at 2000rpm for 30s. The resulting film thickness was about 45μm and since the control layer itself was 30 μm, the PDMS membrane for valve operation is about 15μm in thickness.

Another PDMS prepolymer mixture was prepared at a ratio of 20:1 (base : curing agent) for fluidic layer molding. The PDMS fluidic layer was about 8mm thick for good mechanical strength during experiment. After the vacuum treatment, the two PDMS master molds were baked at 70°C for 30min. Following the baking step, fluidic layer was solidified enough for later

process while the thin control layer was still sticky, which was preferred for the interlayer bonding. The fluidic layer was then peeled off from the master mold and cut into single device pieces. A gage 20 blunt need was used to punch inlet and outlet holes in the fluidic layer. The fluidic layer was then aligned onto the control layer under a microscope. The aligned chips were then baked at 70^{o}C for overnight. (Because of the base and curing agent mixing ratio difference, the resulting control layer contained excess of vinyl groups and the resulting fluidic layer contained excess of silicon hydride groups. Cross-linking between these vinyl groups and silicon hydride groups happened at the interface, and good interlayer bonding was therefore achievable).

After overnight baking, the two layers were irreversibly bonded. So when the thick fluidic layer was peeled off from the wafer, the control layer came off with it. Glass slide was used to mount the whole chip and seal against the control layer. Cleaned glass slide and the PDMS chip were both treated in oxygen plasma (150mtorr oxygen flow, 50W RF power) for 30s to generate silanol groups on both surfaces. Right after the plasma treatment, the two surfaces were brought together and boned onto each other.

4.4 Non-specific Adsorption Blocking on PDMS Surface

PDMS surface is strongly hydrophobic and has a water contact angle of about 108^{o} [89] which is higher than the commonly used solid substrate – polystyrene (PS) (water contact angle is about 90^{o} [110, 111]). Since the immobilization of coating antibody is accomplished by physical adsorption, stronger hydrophobicity may result higher coating antibody density on the substrate surface, however, it can also adsorb reporter antibody if vacant binding sites on the surface are not properly blocked and cause higher background signal or even false results. It is thus important to look for a good blocking protocol that can effectively work on PDMS surface before PDMS microfluidic chip can actually be used for immunoassay applications.

Although PDMS has been used as the immunoassay solid phase substrate by different researchers, mixed results have been reported regarding the blocking scheme on PDMS surface. Eteshola et al. reported that bovine serum albumin (BSA) could not effectively block the non-specific adsorption on the PDMS surface [112], while Ziegler and co-workers used BSA as the blocking solution when developing their PDMS based immunoassay chip [113]. To investigate the blocking efficiency of different blocking solution on PDMS surface, a simple experiment was designed. Degassed PDMS prepolymer (mixed at 10:1 base to curing agent ratio) was coated into wells of a blank 96 well microplate (BD Falcon^{TM} ELISA plate, BD Bioscience, Bedford, MA) so that the surface of each well was covered with a thin layer of PDMS after curing. Immunoassay process was run as usual using the PDMS coated microplate, and the plate reader can still be used as the signal reading instrument, but the PDMS surface was the solid substrate for immunoassay now instead of the PS surface. In a typical assay process, 250 μl of corresponding blocking solution was first introduced into its designated well and incubated at 37^{o}C for 1 hour. Blocked wells were then washed three times with phosphate buffered saline (PBS) solution (Sigma Aldrich, St. Louis, MO). 50 μl of goat anti-mouse IgG conjugagted with horse radish peroxidase (HRP) (Sigma Aldrich) (1 μg/mL diluted in PBS solution containing 0.5% BSA) was then added into each well and incubated at 37^{o}C for another 40 minutes. Depending on the blocking efficiency, different amount of anti-mouse IgG may be adsorbed onto the PDMS well surface. After washing for three times, the resulting wells were then each filled with 50 μl tetramethylbenzidme (TMB) substrate (Sigma Aldrich) and allowed to react for 2 minute. The prepared microplate was then put into a Safire2 microplate reader (Tecan Group Ltd., Switzerland) and absorbance at 650 nm wavelength was measured for each well.

In our experiment, the non-specific binding signals on PDMS and PS surfaces were first

studied by using anti-mouse IgG-HRP diluted in PBS without adding BSA. Since no binding competition from BSA molecules existed, signals generated by non-specific binding of anti-mouse IgG-HRP were very high as can be seen from Figure 4-4 (Non-specific binding). It is also

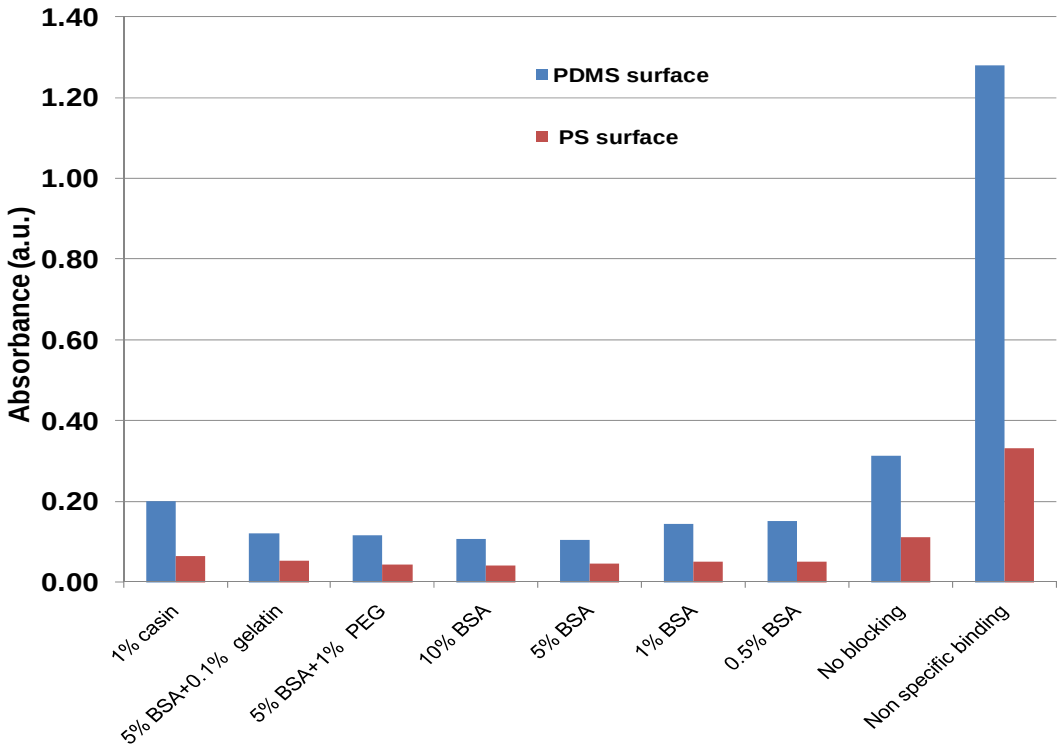

Figure 4-4 Background signal under different blocking conditions

clear that the non-specific binding on PDMS surface is much stronger than that on the PS surface. By adding 0.5% BSA into the PBS solution when diluting the reporter antibody, the non-specific background signal became considerably lower (Figure 4-4, No blocking) even without any blocking step, however, the background signal on PDMS surface was still not acceptable in highly sensitive immunoassay. To search for a good blocking solution for PDMS surface, seven different recipes for blocking solution were tested, which include 1% casin (Sigma Aldrich), 5% BSA + 0.1% gelatin (Sigma Aldrich), 5% BSA +1% polyethylene glycol (PEG 6000, Sigma Aldrich), 10% BSA, 5% BSA, 1% BSA and 0.5% BSA. From the results

shown in Figure 4-4, it can be seen that all of the seven blocking solutions are effective on PS surface. However, on the PDMS surface, higher concentration BSA solutions work the best. 5% BSA can provide good blocking on PDMS surface and further increasing BSA concentration does not help blocking but may cause unnecessary difficulties during solution preparation due to limited solubility of BSA in water. Adding additives such as gelatin and PEG also does not observably improve the blocking efficiency. Although the background signal on PDMS surface is still higher than that is on PS surface even with 5% BSA blocking for one hour, it is already substantially reduced comparing to the non-blocking case. In the other hand, high non-specific affinity of PDMS surface would be helpful for immobilizing more capture antibody and thus enhancing immunoassay signal, its slightly higher non-specific background can be compensated in a certain degree.

4.5 On-chip Immunoassay

In this experiment, mouse serum, goat anti-mouse IgG and goat anti-mouse IgG conjugated with FITC label were selected to form the model sandwich immuno-complex. All immuno reagents were purchase from Bethyl Laboratory Inc. (Montgomery, TX).

The on chip immunoassay protocol is illustrated in Figure 4-5 (a)-(d). First, with micro pneumatic valves on transverse channel X1-X4 pressurized at 20 psi, 10 μl of coating antibody (goat anti-mouse IgG, 10 μg/ml) was injected into longitudinal channel Y at the flow rate of 10 μl/min using a precise syringe pump (BASi, West Lafayette, IN) (Figure 4-5 (a)). After 1 hour incubation, channel Y was washed by continuous PBS buffer flow for 10 minutes at the flow rate of 10 μl/min. Blocking solution (5% BSA in PBS buffer) was then injected into channel Y and was incubated for 1 hour to block the vacant non-specific binding sites on PDMS surface (Figure 4-5 (b)). After another 10 minute PBS washing step, valves on channel X1-X4 were relaxed and

valves on channel Y were closed. 10 µl of mouse IgG solutions with different concentrations (prepared in PBS buffer containing 0.5% BSA) were introduced into channel X1, X2, X3 and X4, respectively, at the flow rate of 2 µl/min (Figure 4-5 (c)). The solutions were allowed to

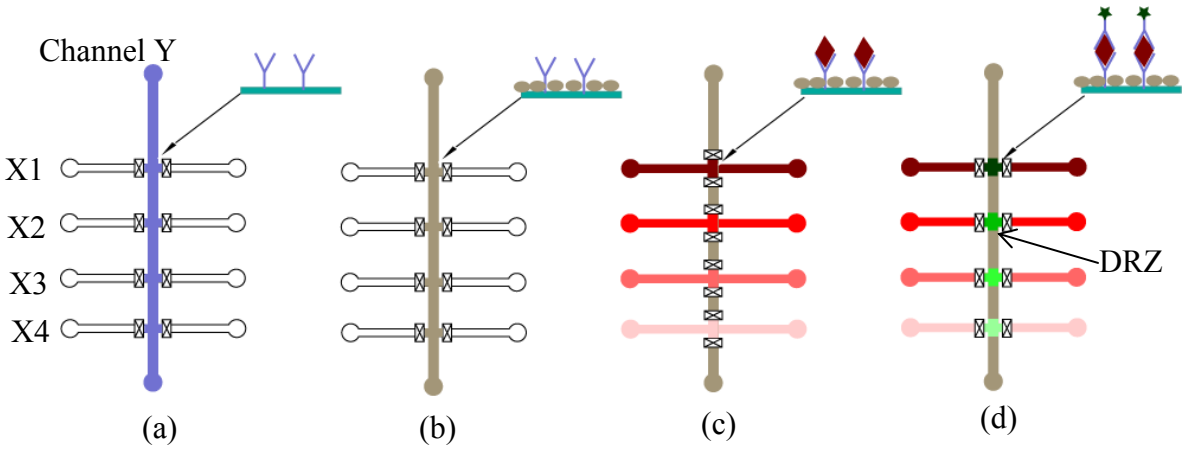

Figure 4-5 On-chip immunoassay protocol

react for 40 minutes and then channel X1-X4 were also washed for 10 minutes. Next, valves on channel Y were released and valves on channel X1-X4 were pressurized again. Reporting antibody solution (goat anti-mouse IgG conjugated with FITC, 10 µg/ml in PBS buffer containing 0.5% BSA) was then injected into channel Y and allowed to react for 40 minutes (Figure 4-5 (d)). After a final 10 minute washing, the resulting microchip was ready for observation under a fluorescence microscope. All incubations were accomplished at room temperature and under no agitation.

Figure 4-6 (a) shows a typical fluorescence image of the PDMS microchip after on-chip immunoassay (image taken under a Nikon Eclipse TE2000-E, 4x objective and 500 ms exposure time were used). The green cross patterns from left to right are associated with mouse IgG concentrations at 5 ng/ml, 20 ng/ml, 80 ng/ml and 320 ng/ml, respectively. It can be seen from Figure 4-6 (a) that the intensity of fluorescence increased with the increase of IgG concentration.

From the description of the on-chip assay protocol, it should be noticed that the segments in channel Y between two consecutive DRZs were successively coated with coating antibody, blocking agent and reporting antibody without IgG antigen. Therefore, the fluorescence intensities at these segments can serve as the negative control. As shown in Figure 4-6 (a), no obvious background signal was observed in negative control segments during our on-chip

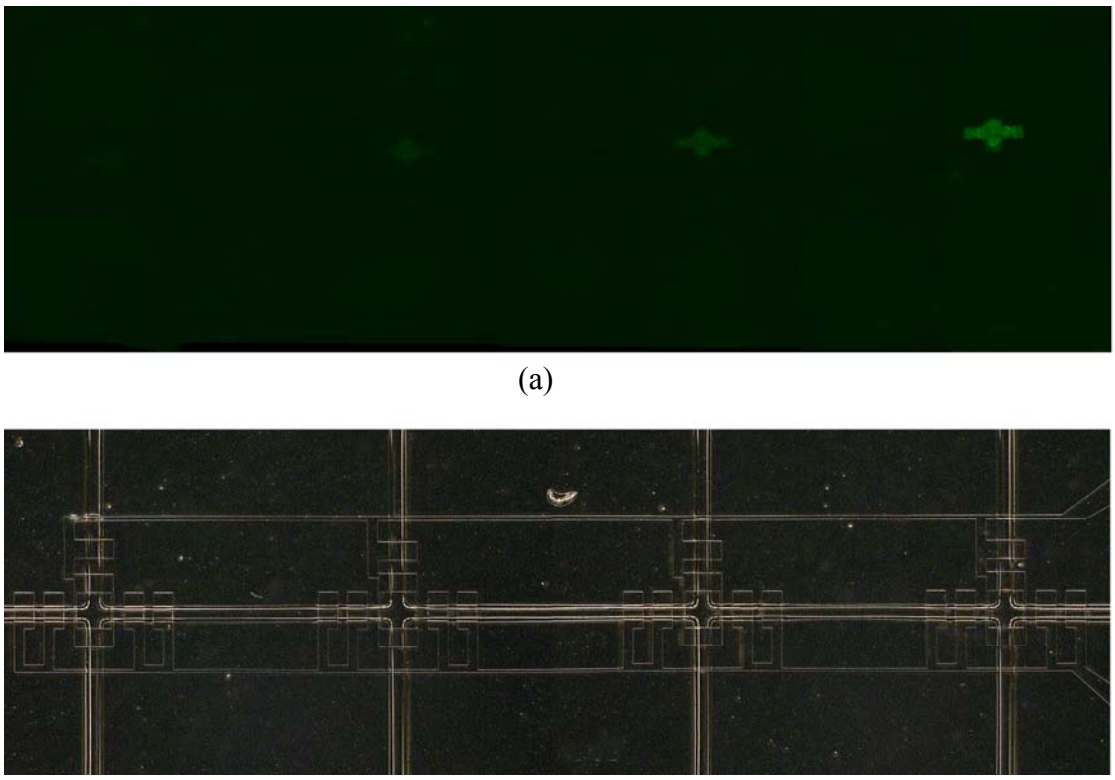

(a)

(b)

Figure 4-6 On-chip immunoassay result: (a) fluorescent image of the four DRZs after immunoassay (analyte concentrations from left to right are 5 ng/ml, 20 ng/ml, 80 ng/ml and 320 ng/ml, respectively); (b) bright field image of the same microfluidic chip

immunoassay experiment, which was ascribed to the well blocking of non-specific adsorption in the channels. Figure 4-6 (b) is the corresponding bright field image of the same chip. Furthermore, it is evident from Figure 4-6 (a) that integrated micro valves provided good sealing with 20 psi working pressure and cross contaminations between isolated DRZ were effectively

prevented. All immuno-reactions happened only at four DRZs, so only DRZs have captured reporting antibodies and generated bright spots under fluorescence microscope.

Fluorescence intensities at DRZs and the negative control were quantified with public domain software ImageJ which is available through the National Institutes of Health website. The average gray scale intensity of each DRZ was used as the signal intensity (SI) which was then normalized against negative control intensity (NCI) using the following equation.

$$\text{Normalized Intensity} = (SI - NCI) / NCI \qquad (4\text{-}1)$$

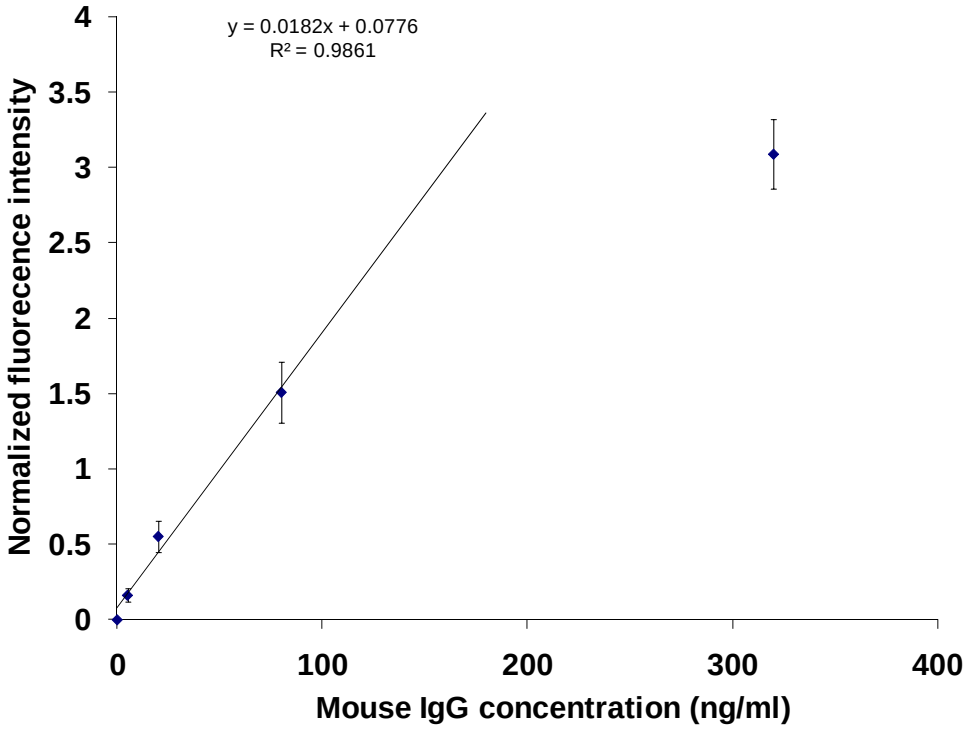

Figure 4-7 Calibration curve of the mouse IgG immunoassay performed on developed microchip platform

During experiment, immunoassay was performed repeatedly on four different chips under same conditions. Four concentrations and the control experiment were performed on each chip. Normalized signals generated using different chips were collected to study inter-chip repeatability. The calibration curve is shown in Figure 4-7. One can see from this figure that the

fluorescence intensity linearly increases with increase of IgG concentration in the range from 5 ng/mL to 100 ng/mL. The regression equation is $y = 0.0182x + 0.0776$ with the correlation coefficient R2=0.99, where y is the normalized fluorescence intensity and x is the mouse IgG concentration. However, the curve starts to level off after IgG concentration becomes higher. The limit of detection (LOD) was estimated to be 5 ng/ml (about 33 pM) which is very competitive among microchip-based immunoassay for IgG detection (Dodge et al. 50 nM [114], Eteshola and Leckband 17 nM [112], Lai et al. 31 nM [115], Li et al. 3.8 nM [116]).

4.6 Conclusions and Future Work

A PDMS microchip based on-chip immunoassay was successfully developed and demonstrated with mouse IgG as the model analyte. With the integration of controllable micro pneumatic valves, immunoreactions can only happen in the DRZs and thus cross-contamination was effectively eliminated. Preliminary experiments with mouse IgG showed that LOD as low as 5 ng/ml was achievable with this microchip as the immunoassay platform. It is found that high concentration BSA blocking solution (5% BSA in PBS buffer) can effectively suppress the non-specific binding in the surface of the microfluidic channels.

Based on this basic design, it is also possible to integrate a large number of DRZs in a single chip for high throughput and multiplexed applications. A second generation chip with 5 x 5 DRZs has already been fabricated and will be used in multiplex immunoassay applications.

Although only one analyte was demonstrated in this work, this on-chip immunoassay design can also accommodate in multiplex immunoassay applications with each DRZ dedicated for one target analyte. The basic multiplex immunoassay scheme can be easily performed by slightly modifying the assay protocol described previously. Briefly, four transverse channels can be coated with different coating antibodies. After blocking step, sample solution can be

introduced into the longitudinal channel. Various analytes presented in the sample solution can be caught by corresponding antibody immobilized at each DRZ. Reporter antibodies can then be respectively introduced through corresponding transverse channel or introduced together into the longitudinal channel assuming no cross reaction existed among different antibodies.

CHAPTER 5. SUMMARY

As stated previously, this dissertation focused on developing novel polymer based MEMS devices/components utilizing various polymer microfabrication techniques. The contribution of the research work presented in this dissertation is twofold. One is the development of new polymer microfarbrication techniques, and the other one is the development of new polymer based MEMS devices/components.

In the area of polymer based microfabrication, this dissertation made the following contribution and innovations:

(1) Developed a fast quasi-3D microstructure replication technique using PDMS molding and UV curable polymer casting. This new technique reduced the fabrication time of out-of-plane microlens from 2 days to less than 5 hours. In addition, more polymers, with various optical characteristics, can be used as the lens material, which in turn broaden the potential applications for the out-of-plane microlens.

(2) Innovated an in-situ out-of-plane microlens fabrication technique. This novel technique is capable of making both convex and concave microlens with definable focal length at the precise desirable position in a microchip. The whole process is completely compatible with soft lithography technique and the lens requires minimal footprint in the mask design.

(3) Developed a PDMS to PDMS double casting process to fabricate microstructure with same shape as the mold but made of PDMS. Experimental results have shown that this technique not only can be used to fabricate ordinary micro patterns, but also is capable of making flexible high-aspect ratio microstructures.

In the area of MEMS devices/components development, the research work included in this dissertation has made the following achievements:

(1) Designed, fabricated and tested a microchip flow cytometer with 3D hydrofocusing chamber and an integrated out-of-plane microlens array. Recently optimized hydrofocusing chamber has shown that it is capable of focusing the sample stream down to less than 10 μm in both horizontal and vertical directions. This result is comparable with the flow cuvette used in conventional flow cytometer. Out-of-plane microlens was used for the on-chip light collection. Results have shown that although it introduced higher requirement on the position and size of focused sample beam, the light collection efficiency was substantially improved.

(2) Developed and tested a PDMS microchip based platform for high throughput multiplex immunoassay applications. Controllable micro pneumatic valves were integrated into the microchip to facilitate the on-chip manipulation of fluidic reagents. Immuno-reactions only happen at the desirable areas called designated reaction zones. To demonstrate the feasibility of this device, mouse IgG was used as the model analyate. Although inexpensive polyclonal antibody were used in the demonstration experiments, detection limit as low as 5 ng/mL was achieved.

Although the research finished in this dissertation has made contribution to this dynamically evolving field, more work is necessary to improve the fabrication technique and device development. For example, only fluorescent detection was tested in the micro flow cytometer. In the future work, scattering signal at various angles and multi-channel fluorescent signal detection can be included in the chip design. Due to the nature of micro flow cytometer, the integration of these detection units is very challenging, but if success, may eventually make microchip based flow cytometer competitive to conventional flow cytometer with the respect of sample characterization capability, while stilling being compact and portable.

REFERENCES

1. J. Bryzek, S. Roundy, B. Bircumshaw, C. Chung, K. Castellino, J. R. Stetter, and M. Vestel, "Marvelous MEMS," *Circuits and Devices Magazine, IEEE* **22**(2), 8-28 (2006)

2. R. P. Feynman, "There's Plenty of Room at the Bottom," *Journal of Microelectromechanical Systems* **1**(1), 60-66 (1992)

3. W. C. Tang, T.-C. H. Nguyen, M. W. Judy, and R. T. Howe, "Electrostatic-comb drive of lateral polysilicon resonators," *Sense and Actuator A* **21**(1-3), 328-331 (1990)

4. M. Gad-el-Hak, "MEMS: design and fabrication," pp. 9.1-9.35, CRC Press, Boca Raton, FL (2005).

5. R. Yang and W. Wang, "A numerical and experimental study on gap compensation and wavelength selection in UV-lithography of ultra-high aspect ratio SU-8 microstructures," *Sensors and Actuators B: Chemical* **110**(2), 279-288 (2005)

6. R. Yang and W. Wang, "Out-of-plane polymer refractive microlens fabricated based on direct lithography of SU-8," *Sensors and Actuators A: Physical* **113**(1), 71-77 (2004)

7. W. Dai, K. Lian, and W. Wang, "Design and fabrication of a SU-8 based electrostatic microactuator," *Microsystem Technologies* **13**(3), 271-277 (2007)

8. P. Ruther, B. Gerlach, J. Gottert, M. Ilie, J. Mohr, A. Muller, and C. Ossmann, "Fabrication and characterization of microlenses realized by a modified LIGA process," *Pure and Applied Optics: Journal of the European Optical Society Part A* **6**(6), 643-653 (1997)

9. S. K. Lee and et al., "A simple method for microlens fabrication by the modified LIGA process," *Journal of Micromechanics and Microengineering* **12**(3), 334 (2002)

10. V. Nazmov, L. Shabel'nikov, F. J. Pantenburg, J. Mohr, E. Reznikova, A. Snigirev, I. Snigireva, S. Kouznetsov, and M. DiMichiel, "Kinoform X-ray lens creation in polymer materials by deep X-ray lithography," *Nuclear Instruments and Methods in Physics Research Section B: Beam Interactions with Materials and Atoms* **217**(3), 409-416 (2004)

11. F. Pérennès, M. Matteucci, W. Jark, and B. Marmiroli, "Fabrication of refractive X-ray focusing lenses by deep X-ray lithography," *Microelectronic Engineering* **78-79**(79-87 (2005)

12. W. Jinsheng, G. Yadong, G. Abba, C. Jianfeng, S. Jiashun, and C. Guangqi, "Micro Milling Technologies for MEMS," in *Perspective Technologies and Methods in MEMS Design, 2007. MEMSTECH 2007. International Conference on*, pp. 86-95 (2007).

13. C. R. Friedrich and M. J. Vasile, "The micromilling process for high aspect ratio microstructures," *Microsystem Technologies* **2**(3), 144-148 (1996)

14. Q. Mei, Z. Xia, F. Xu, S. A. Soper, and Z. H. Fan, "Fabrication of Microfluidic Reactors and Mixing Studies for Luciferase Detection," *Analytical Chemistry* **80**(15), 6045-6050 (2008)

15. X. Liu, D. Du, and G. Mourou, "Laser ablation and micromachining with ultrashort laser pulses," *Quantum Electronics, IEEE Journal of* **33**(10), 1706-1716 (1997)

16. Y. Nakata, T. Okada, and M. Maeda, "Micromachining of a thin film by laser ablation using femtosecond laser with masks," *Optics and Lasers in Engineering* **42**(4), 389-393 (2004)

17. R. Steve and P. Robert, "A review of focused ion beam applications in microsystem technology," *Journal of Micromechanics and Microengineering* **11**(4), 287 (2001)

18. R. M. Langford and et al., "Focused ion beam micromachining of three-dimensional structures and three-dimensional reconstruction to assess their shape," *Journal of Micromechanics and Microengineering* **12**(2), 111 (2002)

19. Y. Xia, E. Kim, X.-M. Zhao, J. A. Rogers, M. Prentiss, and G. M. Whitesides, "Complex Optical Surfaces Formed by Replica Molding Against Elastomeric Masters," *Science* **273**(5273), 347-349 (1996)

20. J. C. McDonald, D. C. Duffy, J. R. Anderson, D. T. Chiu, H. Wu, O. J. A. Schueller, and G. M. Whitesides, "Fabrication of microfluidic systems in poly(dimethylsiloxane)," *Electrophoresis* **21**(1), 27-40 (2000)

21. X.-M. Zhao, Y. Xia, and G. M. Whitesides, "Soft lithographic methodes for nano-fabrication," *Journal of Material Chemistry* **7**(7), 1069-1074 (1997)

22. Y.-J. Juang, L. J. Lee, and K. W. Koelling, "Hot embossing in microfabrication. Part I: Experimental," *Polymer Engineering & Science* **42**(3), 539-550 (2002)

23. Y.-C. Wang, A. L. Stevens, and J. Han, "Million-fold Preconcentration of Proteins and Peptides by Nanofluidic Filter," *Analytical Chemistry* **77**(14), 4293-4299 (2005)

24. D. D. Carlo, K.-H. Jeong, and L. P. Lee, "Reagentless mechanical cell lysis by nanoscale barbs in microchannels for sample preparation," *Lab on a Chip* **3**(4), 287-291 (2003)

25. J. Wang, A. Ibanez, M. P. Chatrathi, and A. Escarpa, "Electrochemical Enzyme Immunoassays on Microchip Platforms," *Analytical Chemistry* **73**(21), 5323-5327 (2001)

26. G.-R. Yi, T. Thorsen, V. N. Manoharan, M.-J. Hwang, S.-J. Jeon, D. J. Pine, S. R. Quake, and S.-M. Yang, "Generation of Uniform Colloidal Assemblies in Soft Microfluidic Devices," *Advanced Materials* **15**(15), 1300-1304 (2003)

27. M. A. Unger, H.-P. Chou, T. Thorsen, A. Scherer, and S. R. Quake, "Monolithic Microfabricated Valves and Pumps by Multilayer Soft Lithography," *Science* **288**(5463), 113-116 (2000)

28. R. Yang, J. D. Williams, and W. Wang, "A rapid micro-mixer/reactor based on arrays of spatially impinging micro-jets," *Journal of Micromechanics and Microengineering* **14**(10), 1345-1351 (2004)

29. M. Yamada and M. Seki, "Hydrodynamic filtration for on-chip particle concentration and classification utilizing microfluidics," *Lab on a Chip* **5**(11), 1233-1239 (2005)

30. R. Jindal and S. M. Cramer, "On-chip electrochromatography using sol-gel immobilized stationary phase with UV absorbance detection," *Journal of Chromatography A* **1044**(1-2), 277-285 (2004)

31. C. D. Garcia and C. S. Henry, "Direct Determination of Carbohydrates, Amino Acids, and Antibiotics by Microchip Electrophoresis with Pulsed Amperometric Detection," *Analytical Chemistry* **75**(18), 4778-4783 (2003)

32. J.-C. Roulet, R. Volkel, H. P. Herzig, E. Verpoorte, N. F. de Rooij, and R. Dandliker, "Performance of an Integrated Microoptical System for Fluorescence Detection in Microfluidic Systems," *Analytical Chemistry* **74**(14), 3400-3407 (2002)

33. "Optical MEMS networks into light," *III-Vs Review* **17**(4), 6-6 (2004)

34. M. C. Wu, O. Solgaard, and J. E. Ford, "Optical MEMS for Lightwave Communication," *Lightwave Technology, Journal of* **24**(12), 4433-4454 (2006)

35. C. Marxer, M. A. Gretillat, N. F. de Rooij, R. Battig, O. Anthamatten, B. Valk, and P. Vogel, "Reflective duplexer based on silicon micromechanics for fiber-optic communication," *Lightwave Technology, Journal of* **17**(1), 115-122 (1999)

36. K. Isamoto, K. Kato, A. Morosawa, C. Changho, H. Fujita, and H. Toshiyoshi, "A 5-V operated MEMS variable optical attenuator by SOI bulk micromachining," *Selected Topics in Quantum Electronics, IEEE Journal of* **10**(3), 570-578 (2004)

37. J. E. Ford, K. W. Goossen, J. A. Walker, D. T. Neilson, D. M. Tennant, P. Seo Yeon, and J. W. Sulhoff, "Interference-based micromechanical spectral equalizers," *Selected Topics in Quantum Electronics, IEEE Journal of* **10**(3), 579-587 (2004)

38. J. Tsai, S. Huang, H. Dooyoung, H. Toshiyoshi, and M. C. Wu, "Open-loop operation of MEMS-based 1×N wavelength-selective switch with long-term stability and repeatability," *Photonics Technology Letters, IEEE* **16**(4), 1041-1043 (2004)

39. H. Dooyoung, S. T. Y. Huang, T. Jui-Che, H. Toshiyoshi, and M. C. Wu, "Low-voltage, large-scan angle MEMS analog micromirror arrays with hidden vertical comb-drive actuators," *Microelectromechanical Systems, Journal of* **13**(2), 279-289 (2004)

40. J. Tsai and M. C. Wu, "A high port-count wavelength-selective switch using a large scan-angle, high fill-factor, two-axis MEMS scanner array," *Photonics Technology Letters, IEEE*

18(13), 1439-1441 (2006)

41. J. E. Ford, V. A. Aksyuk, D. J. Bishop, and J. A. Walker, "Wavelength add-drop switching using tilting micromirrors," *Lightwave Technology, Journal of* **17**(5), 904-911 (1999)

42. J. K. Rhee, I. Tomkos, and L. Ming-Jun, "A broadcast-and-select OADM optical network with dedicated optical-channel protection," *Lightwave Technology, Journal of* **21**(1), 25-31 (2003)

43. M. Garrigues, J. Danglot, J. L. Leclercq, and O. Parillaud, "Tunable high-finesse InP/air MOEMS filter," *Photonics Technology Letters, IEEE* **17**(7), 1471-1473 (2005)

44. V. Kaman, Z. Xuezhe, Y. Shifu, J. Klingshirn, C. Pusarla, R. J. Helkey, O. Jerphagnon, and J. E. Bowers, "A 32×10 Gb/s DWDM metropolitan network demonstration using wavelength-selective photonic cross-connects and narrow-band EDFAs," *Photonics Technology Letters, IEEE* **17**(9), 1977-1979 (2005)

45. L. J. Hornbeck, "Digital Light Processing for high-brigntness high-resolution applications," in *Electronic Imaging, EI' 97* M. H. Wu, Ed., pp. 27-40, SPIE, San Jose, California USA (1997).

46. D. T. Amm and R. W. Corrigan, "Grating Light Valve Technology: Update and Novel Applications," in *Society for Information Display Symposium*, Anaheim, CA (1998).

47. H. Xie, Y. Pan, and G. K. Fedder, "Endoscopic optical coherence tomographic imaging with a CMOS-MEMS micromirror," *Sensors and Actuators A: Physical* **103**(1-2), 237-241 (2003)

48. C. Changho, K. Isamoto, and H. Toshiyoshi, "Optically Modulated MEMS scanning endoscope," *Photonics Technology Letters, IEEE* **18**(1), 133-135 (2006)

49. D. Shimura, R. Sekikawa, K. Kotani, M. Uekawa, Y. Maeno, K. Aoyama, H. Sasaki, T. Takamori, K. Masuko, and S. Nakaya, "Bidirectional optical subassembly with prealigned silicon microlens and laser diode," *Photonics Technology Letters, IEEE* **18**(16), 1738-1740 (2006)

50. J. Arai, H. Kawai, and F. Okano, "Microlens arrays for integral imaging system," *Appl. Opt.* **45**(36), 9066-9078 (2006)

51. M. Martínez-Corral, B. Javidi, R. Martínez-Cuenca, and G. Saavedra, "Integral Imaging with Improved Depth of Field by Use of Amplitude-Modulated Microlens Arrays," *Appl. Opt.* **43**(31), 5806-5813 (2004)

52. H. Kwon, Y. Yee, C.-H. Jeong, H.-J. Nam, and J.-U. Bu, "A high-sag microlens array film with a full fill factor and its application to organic light emitting diodes," *Journal of Micromechanics and Microengineering* **18**(6), 065003 (2008)

53. J.-N. Kuo, C.-C. Hsieh, S.-Y. Yang, and G.-B. Lee, "An SU-8 microlens array fabricated by soft replica molding for cell counting applications," *Journal of Micromechanics and Microengineering* **17**(4), 693-699 (2007)

54. P. Nussbaum, R. Volkel, H. P. Herzig, M. Eisner, and S. Haselbeck, "Design, fabrication and testing of microlens arrays for sensors and microsystems," *Pure and Applied Optics: Journal of the European Optical Society Part A* **6**(6), 617-636 (1997)

55. E. Roy, B. Voisin, J. F. Gravel, R. Peytavi, D. Boudreau, and T. Veres, "Microlens array fabrication by enhanced thermal reflow process: Towards efficient collection of fluorescence light from microarrays," *Microelectronic Engineering* **86**(11), 2255-2261 (2009)

56. M. He, X. Yuan, K. J. Moh, J. Bu, and X. Yi, "Monolithically integrated refractive microlens array to improve imaging quality of an infrared focal plane array," *Optical Engineering* **43**(11), 2589-2594 (2004)

57. D. Liang and J. Hongrui, "Selective Formation and Removal of Liquid Microlenses at Predetermined Locations Within Microfluidics Through Pneumatic Control," *Microelectromechanical Systems, Journal of* **17**(2), 381-392 (2008)

58. V. Lien, Y. Berdichevsky, and Y.-H. Lo, "Microspherical surfaces with predefined focal lengths fabricated using microfluidic capillaries," *Applied Physics Letters* **83**(26), 5563-5565 (2003)

59. R. Yang, W. Wang, and S. A. Soper, "Out-of-plane microlens array fabricated using ultraviolet lithography," *Applied Physics Letters* **86**(16), 161110-161113 (2005)

60. K.-H. Jeong, J. Kim, and L. P. Lee, "Biologically Inspired Artificial Compound Eyes," *Science* **312**(5773), 557-561 (2006)

61. C. N. LaFratta, L. Li, and J. T. Fourkas, "Soft-lithographic replication of 3D microstructures with closed loops," *Proceedings of the National Academy of Sciences* **103**(23), 8589-8594 (2006)

62. H. Sato, D. Yagyu, S. Ito, and S. Shoji, "Improved inclined multi-lithography using water as exposure medium and its 3D mixing microchannel application," *Sensors and Actuators A: Physical* **128**(1), 183-190 (2006)

63. E. Hetch, *Optics*, Benjamin Cummings, San Francisco (2001).

64. S. K. Hsiung, C. H. Lee, and G. B. Lee, "Microcapillary electrophoresis chips utilizing controllable micro-lens structures and buried optical fibers for on-line optical detection," *Electrophoresis* **29**(9), 1866-1873 (2008)

65. N. Chronis, G. Liu, K.-H. Jeong, and L. Lee, "Tunable liquid-filled microlens array integrated with microfluidic network," *Opt. Express* **11**(19), 2370-2378 (2003)

66. J. El-Ali, P. K. Sorger, and K. F. Jensen, "Cells on chips," *Nature* **442**(7101), 403-411 (2006)

67. M. Toner and D. Irimia, "BLOOD-ON-A-CHIP," *Annual Review of Biomedical Engineering* **7**(1), 77-103 (2005)

68. C. H. Lin and G. B. Lee, "Micromachined flow cytometers with embedded etched optic fibers for optical detection," *Journal of Micromechanics and Microengineering* **13**(3), 447-453 (2003)

69. Z. Wang, J. El-Ali, M. Engelund, T. Gotsaed, I. R. Perch-Nielsen, K. B. Mogensen, D. Snakenborg, J. P. Kutter, and A. Wolff, "Measurements of scattered light on a microchip flow cytometer with integrated polymer based optical elements," *Lab on a Chip* **4**(4), 372-377 (2004)

70. N. Watkins, B. M. Venkatesan, M. Toner, W. Rodriguez, and R. Bashir, "A robust electrical microcytometer with 3-dimensional hydrofocusing," *Lab on a Chip* **9**(22), 3177-3184 (2009)

71. R. Yang, D. L. Feeback, and W. Wang, "Microfabrication and test of a three-dimensional polymer hydro-focusing unit for flow cytometry applications," *Sensors and Actuators A: Physical* **118**(2), 259-267 (2005)

72. N. H. Kim, "How to model coupling into a multimode fiber," in *Zemaxer Users' Knowledge Base* (2007).

73. R. Noek, C. Knoernschild, J. Migacz, T. Kim, P. Maunz, T. Merrill, H. Hayden, C. S. Pai, and J. Kim, "Multiscale optics for enhanced light collection from a point source," *Opt. Lett.* **35**(14), 2460-2462 (2010)

74. J. W. Shaevitz and D. A. Fletcher, "Enhanced three-dimensional deconvolution microscopy using a measured depth-varying point-spread function," *J. Opt. Soc. Am. A* **24**(9), 2622-2627 (2007)

75. Lili Wang, Adolfas K. Gaigalas, Fatima Abbasi, and Gerald E. Marti, "Quantitating Fluorescence Intensity From Fluorophores: Practical Use of MESF Values," *Journal of Research of the National Institute of Standards and Technology* **107**(339-353 (2002)

76. Miroslaw Jonasz and Georges R. Fournier, *Light Scattering by Particles in Water*, Academic Press, London, UK (2007).

77. A. Waggoner, "Fluorescent probes for cytometry," *Flow cytometry and sorting* 209–225 (1990)

78. R. Xu, *Particle Characterization: Light Scattering Methods*, Kluwer Academic Publishers, Netherlands (2000).

79. H. M. Shapiro, *Practical Flow Cytometry*, John Wiley & Sons, Inc., Hoboken, New Jersey (2003).

80. J. C. S. Wood, "Flow cytometer performance: Fluorochrome dependent sensitivity and instrument configuration," *Cytometry* **22**(4), 331-332 (1995)

81. E. Udoetok, T. Charalampopoulos, W. Wang, and G. Shao, "Simulation of Hydrofocusing in Flow Cytometry," *Submitted to International Journal of Computational Fluid Dynamics* (2010)

82. L. Gwo-Bin and et al., "The hydrodynamic focusing effect inside rectangular microchannels," *Journal of Micromechanics and Microengineering* **16**(5), 1024 (2006)

83. F. M. White, *Fluid Mechanics*, Mcgraw-Hill College (1998).

84. F. M. White, *Viscous Fluid Flow*, McGraw-Hill Science (1991).

85. C. Wiginton and C. Dalton, "Incompressible laminar flow in the entrance region of a rectangular duct," *Journal of Applied Mechanics* **37**(854 (1970)

86. T. Ahmad and I. Hassan, "Experimental Analysis of Microchannel Entrance Length Characteristics Using Microparticle Image Velocimetry," *Journal of Fluids Engineering* **132**(4), 041102-041113 (2010)

87. M. Sun, C. Luo, L. Xu, H. Ji, Q. Ouyang, D. Yu, and Y. Chen, "Artificial Lotus Leaf by Nanocasting," *Langmuir* **21**(19), 8978-8981 (2005)

88. L. Gitlin, P. Schulze, and D. Belder, "Rapid replication of master structures by double casting with PDMS," *Lab on a Chip* **9**(20), 3000-3002 (2009)

89. D. C. Duffy, J. C. McDonald, O. J. A. Schueller, and G. M. Whitesides, "Rapid prototyping of microfluidic systems in poly(dimethylsiloxane)," *Anal. Chem.* **70**(23), 4974-4984 (1998)

90. R. S. Yalow and S. A. Berson, "Assay of Plasma Insulin in Human Subjects by Immunological Methods," *Nature* **184**(4699), 1648-1649 (1959)

91. J. Wu, Z. Fu, F. Yan, and H. Ju, "Biomedical and clinical applications of immunoassays and immunosensors for tumor markers," *TrAC Trends in Analytical Chemistry* **26**(7), 679-688

92. G. Marielle and L. Pirjo, "A comparison between on-site immunoassay drug-testing devices and laboratory results," *Forensic science international* **121**(1), 37-46 (2001)

93. M. Vanderlaan, B. E. Watkins, and L. Stanker, "ES&T Critical Review: Environmental monitoring by immunoassay," *Environmental Science & Technology* **22**(3), 247-254 (1988)

94. D. L. Brandon, R. G. Binder, R. E. Wilson, and W. C. Montague, "Analysis of thiabendazole in potatoes and apples by ELISA using monoclonal antibodies," *Journal of Agricultural and Food Chemistry* **41**(6), 996-999 (1993)

95. I. B. Bakaltcheva, F. S. Ligler, C. H. Patterson, and L. C. Shriver-Lake, "Multi-analyte explosive detection using a fiber optic biosensor," *Analytica Chimica Acta* **399**(1-2), 13-20 (1999)

96. S. Y. Rabbany, W. J. Lane, W. A. Marganski, A. W. Kusterbeck, and F. S. Ligler, "Trace detection of explosives using a membrane-based displacement immunoassay," *Journal of Immunological Methods* **246**(1-2), 69-77 (2000)

97. A. Bange, H. B. Halsall, and W. R. Heineman, "Microfluidic immunosensor systems," *Biosensors and Bioelectronics* **20**(12), 2488-2503 (2005)

98. K. Hosokawa, M. Omata, K. Sato, and M. Maeda, "Power-free sequential injection for microchip immunoassay toward point-of-care testing," *Lab on a Chip* **6**(2), 236-241 (2006)

99. A. Bernard, B. Michel, and E. Delamarche, "Micromosaic Immunoassays," *Analytical Chemistry* **73**(1), 8-12 (2000)

100. B. M. Murphy, X. He, D. Dandy, and C. S. Henry, "Competitive Immunoassays for Simultaneous Detection of Metabolites and Proteins Using Micromosaic Patterning," *Analytical Chemistry* **80**(2), 444-450 (2007)

101. M. J. Madou, L. J. Lee, S. Daunert, S. Lai, and C.-H. Shih, "Design and Fabrication of CD-like Microfluidic Platforms for Diagnostics: Microfluidic Functions," *Biomedical Microdevices* **3**(3), 245-254 (2001)

102. W. H. Grover, A. M. Skelley, C. N. Liu, E. T. Lagally, and R. A. Mathies, "Monolithic membrane valves and diaphragm pumps for practical large-scale integration into glass microfluidic devices," *Sensors and Actuators B: Chemical* **89**(3), 315-323 (2003)

103. J. Melin and S. R. Quake, "Microfluidic Large-Scale Integration: The Evolution of Design Rules for Biological Automation," *Annual Review of Biophysics and Biomolecular Structure* **36**(1), 213-231 (2007)

104. J. Liu, C. Hansen, and S. R. Quake, "Solving the "World-to-Chip" Interface Problem with a Microfluidic Matrix," *Analytical Chemistry* **75**(18), 4718-4723 (2003)

105. A. M. Skelley, J. R. Scherer, A. D. Aubrey, W. H. Grover, R. H. C. Ivester, P. Ehrenfreund, F. J. Grunthaner, J. L. Bada, and R. A. Mathies, "Development and evaluation of a microdevice for amino acid biomarker detection and analysis on Mars," *Proceedings of the National Academy of Sciences of the United States of America* **102**(4), 1041-1046 (2005)

106. C. L. Hansen, S. Classen, J. M. Berger, and S. R. Quake, "A Microfluidic Device for

Kinetic Optimization of Protein Crystallization and In Situ Structure Determination," *Journal of the American Chemical Society* **128**(10), 3142-3143 (2006)

107. J. S. Marcus, W. F. Anderson, and S. R. Quake, "Microfluidic Single-Cell mRNA Isolation and Analysis," *Analytical Chemistry* **78**(9), 3084-3089 (2006)

108. J. Kong, L. Jiang, X. Su, J. Qin, Y. Du, and B. Lin, "Integrated microfluidic immunoassay for the rapid determination of clenbuterol," *Lab on a Chip* **9**(11), 1541-1547 (2009)

109. T. Thorsen, S. J. Maerkl, and S. R. Quake, "Microfluidic Large-Scale Integration," *Science* **298**(5593), 580-584 (2002)

110. E. Moy, F. Y. H. Lin, J. W. Vogtle, Z. Policova, and A. W. Neumann, "Contact angle studies of the surface properties of covalently bonded poly-L-lysine to surfaces treated by glow-discharge," *Colloid & Polymer Science* **272**(10), 1245-1251 (1994)

111. Y. Li, J. Q. Pham, K. P. Johnston, and P. F. Green, "Contact Angle of Water on Polystyrene Thin Films: Effects of CO2 Environment and Film Thickness," *Langmuir* **23**(19), 9785-9793 (2007)

112. E. Eteshola and D. Leckband, "Development and characterization of an ELISA assay in PDMS microfluidic channels," *Sensors and Actuators B: Chemical* **72**(2), 129-133 (2001)

113. J. Ziegler, M. Zimmermann, P. Hunziker, and E. Delamarche, "High-Performance Immunoassays Based on Through-Stencil Patterned Antibodies and Capillary Systems," *Analytical Chemistry* **80**(5), 1763-1769 (2008)

114. A. Dodge, K. Fluri, E. Verpoorte, and N. F. de Rooij, "Electrokinetically Driven Microfluidic Chips with Surface-Modified Chambers for Heterogeneous Immunoassays," *Analytical Chemistry* **73**(14), 3400-3409 (2001)

115. S. Lai, S. N. Wang, J. Luo, L. J. Lee, S. T. Yang, and M. J. Madou, "Design of a compact disk-like microfluidic platform for enzyme-linked immunosorbent assay," *Analytical Chemistry* **76**(7), 1832-1837 (2004)

116. P. Li, A. Abolmaaty, C. D'Amore, S. Demming, C. Anagnostopoulos, and M. Faghri, "Development of an ultrafast quantitative heterogeneous immunoassay on pre-functionalized poly(dimethylsiloxane) microfluidic chips for the next-generation immunosensors," *Microfluidics and Nanofluidics* **7**(4), 593-598 (2009)

VITA

Guocheng Shao hails from Zhejiang province of China. He received his bachelor's degree from Department of Optical Engineering at Zhejiang University in 2004. Then he went on and finished his master's research work at Institute of Micro/Nano Science and Technology, a research institute of Shanghai Jiao Tong University, in 2006. He joined Dr. Wanjun Wang's MEMS research group at Louisiana State University in 2006, where his main research interests focus on the design and fabrication of polymer based optical MEMS and BioMEMS devices.

In addition to his research interests, Guocheng also shares his passion in photography and sports activities, especially American football and soccer.